Application of ultrafast spectroscopy techniques to probe correlated ion hopping mechanisms in solid-state ion conductors

Thesis by
KIM HOÀNG PHẠM

In Partial Fulfillment of the Requirements for the
Degree of
Doctor of Philosophy

CALIFORNIA INSTITUTE OF TECHNOLOGY
Pasadena, California

2025
Defended November 18, 2024

KIM HOÀNG PHẠM
ORCID: 0000-0003-4053-6363

ACKNOWLEDGEMENTS

I truly owe my PhD to all of the professors, colleagues, technical and administrative staff, friends, and family who believed and supported me along my academic journey.

First and foremost, I would like to thank my two faculty advisors, Scott Cushing and Kimberly See.

Scott, thank you for giving me the opportunity to dive headfirst into a challenging project as both my advisor and lab-mate. You were always enthusiastic to spend an extra few hours in sub-basement to conduct experiments with me if that meant we could be one step closer to a research discovery. Your endless encouragement motivated me to push through every research hurdle that came my way. I wouldn't have grown into the independent researcher that I am now without your support and guidance.

Kim, thank you for helping me become a more well-rounded scientist than I was the day before. Thank you for accepting me into your lab, first as a WAVE fellow, and then as your co-advised student. I knew your dedication to students would be unmatched during my visitation weekend at Caltech, when you didn't hesitate to carry me across a river during our hike so that my feet didn't get wet. You not only helped me develop my independence as a researcher, but also taught me how to communicate my science clearly through my writing and in presentations. Thank you for always believing in me and supporting my research, even when my project took a deeper dive into instrumentation and spectroscopy.

Secondly, I want to thank my thesis committee members, Professor Geoffrey Blake, Professor Brian Stoltz, and Professor Katherine Faber.

Geoff, thank you for all of your insightful discussions on my research project and scientific research directions within THz spectroscopy. Brian, thank you for not only reminding me of the big picture impact of my research, but also for your leadership in supporting diversity, equity, and inclusion initiatives within the Chemistry and Chemical Engineering department. My impact within the department was possible because you listened and advocated for my ideas and initiatives. Kathy, thank you for your helpful discussions during my examinations.

Beyond my immediate advisors and committee members, I also want to express my gratitude for all the professors and mentors that shaped my growth as a researcher

during my undergraduate studies. They all played a monumental role in sparking my interest in research and teaching me valuable skills that I used throughout graduate school.

Professor Jerome Robinson, thank you for taking me under your wing as you began to build your lab at Brown. Thank you for always being patient with me as I started doing research for the first time and being my number one advocate and cheerleader. The scientific skills that you helped me develop proved instrumental during my graduate school journey. Thank you Dr. Matthew Lueckheide for being my graduate student mentor and friend. Your optimism and enthusiasm for science never ceases to amaze and inspire me. Thank you Dr. Rachel Klet for mentoring me during my SULI internship at Argonne National Laboratory and teaching me the realities of research and the importance of patience and persistence. Thank you Sarah Bevilacqua for mentoring me during my WAVE fellowship in Kim's group and being so welcoming from the beginning. Your mentorship truly helped set the foundation for my time at Caltech and I couldn't be more thankful looking back.

At Caltech, none of my research would have been possible without the backbone of both the Cushing group and the See group. Both labs provided me two special homes during my time at Caltech. I'm honored to have completed my PhD along some of the smartest and kindest people that I've ever met.

The Cushing battery subgroup grew rapidly in size during my last year at Caltech, and also quickly became the group of people that I will miss working with the most. Thank you Dr. Haw-Wei Lin and Jax Dallas for all your expertise in Terahertz spectroscopy and maintaining those very capabilities in Scott's lab. Thank you to my graduate student mentees, Amy Lin and Natan Spear, for always volunteering (now volun-told) to do the most tedious experiments with the most enthusiastic attitude. Your collective passion for science often reminds me of why I wanted to pursue research in the first place. Working with you both has been an absolute privilege and I look forward to seeing what you both accomplish in the future.

In the Cushing group, I want to give a special thank you to Levi Palmer and Nicholas Heller for being supportive companions who always lent an ear when research got tough.

In the See group, I want to thank Dr. Zachary Iton, as well as my chemistry cohort, Michelle Qian, Brian Lee, and Eshaan Patheria, for their endless support and companionship.

Thank you Zac for being my unofficial mentor and always looking out for my well being during COVID-19 and after. I appreciate all the guidance that you gave me when I first started doing ionics research and am grateful for all of the much needed breaks and outings we took outside the lab. Michelle, thank you for being such a supportive and positive friend, reminding me of my strengths when I feel defeated from lab, helping me survive every hard and sketchy hike that we've done together, and always being down to craft together. Brian, thank you for always sharing your hot takes in the office and always answering my lab questions even when I think they're stupid. Every laugh in our office helps me get through a few more days of graduate school. Eshaan, thank you for being the positive to Brian's pessimism. Your scientific curiosity never ceases to amaze me in addition to your endearing limericks.

Thank you to my graduate student friends, Ana Duarte, Chandler Conn, and Dr. Jake Evans for all of the fun adventures and memories outside of the lab. Thank you Ana and Chandler for being the goofiest, funniest, and kindest friends I could've asked for during my time at Caltech. Thank you Jake for not only being a supportive friend but also being the best TA for my Ch101 class. Your enthusiasm for science and knowledge of electrochemistry is unparalleled and I'm so glad that you volunteered to help teach my students during lab. Also big shout out to the Wednesday Warriors (Zac, Jordan, Dan) for giving me a reason to unwind with friends in the middle of the week for an oddly consistent amount of summer Wednesdays.

Thank you to all of my undergraduate friends who stayed in touch with me after Brown and constantly cheered me on throughout my graduate school journey. Thank you Stella Towne and Teijiro Nishimura (and your cat Nanika!) for your friendship and support especially during COVID-19. Thank you Raekwon Grace for all the fun adventures and company whenever I come back to the East coast. Thank you Sarah Tran and your family for providing me a second home in SoCal and making sure that I had access to home-cooked Vietnamese food. Your warmth and endless support in everything that I do is immensely appreciated.

I would also like to thank all of the technical staff at Caltech that made my research possible, the staff at the Caltech Center for Inclusion and Diversity, and the staff at the Center for Teaching, Learning, and Outreach for all the support in my diversity and teaching efforts.

I want to first thank Maria Manzanares and Carol Casey at the Student-Faculty Programs office for making the WAVE fellowship possible for me while I was an

undergraduate student. This opportunity opened the door that eventually led me to where I am today because they saw something special in my application and wanted to give me a chance to show what I had to offer.

Thank you Michael Roy, Ricardo Zarazua, and Martin Mendez for machining all of the custom electrochemical cell parts for my research. I want to give a special thank you to Ricardo for always being proactive with my machine shop requests and helping me revise complicated cell designs, especially when I ask for unreasonable measurements. I appreciated all of our conversations whenever I visited the shop and am glad to have become your friend over the years that you've been here.

Thank you Elyse Garlok for all your efforts in managing all of the diversity and inclusion initiatives within the department and amplifying student voices. Thank you Dr. Hanna Song and Yazmin Gonzalez for supporting and funding all of the diversity and inclusion efforts that I led and making sure that I maximized impact and outreach. Thank you Dr. Melissa Dabiri and Dr. Jasmine Bryant for guiding my vision for my Ch101 course and exposing me to research-based teaching methods that I could apply. Thank you Dr. Jeffrey Mendez for proving the lab space and equipment to teach my Ch101 course. Thank you to the division for also sponsoring additional supplies for my class. I'm so honored to have met so many passionate and knowledgeable staff who were always willing to help and am grateful to have learned so much from each and every one of you during my time at Caltech.

Finally, I want to thank my family for always being there for me, as well as my extended family across the country. Thank you to all of my cousins in the Bay area and in Orange County for welcoming me whenever I came to visit, especially for the first time. Thank you for providing me another home away from home during the holidays and including me in your festivities. I always wondered what it would be like to grow up in a big family and am glad to have had a glimpse of that experience whenever I visited.

Thank you Ân for reliably supplying a dose of random and silly energy whenever I visit home. Even when we go through long periods of not staying in touch, I know that I will always have a brother that I can readily depend on. Thank you Quỳnh Anh for taking care of my brother and family while I've been in LA, and I look forward to spending more time with you as my sister-in law.

Thank you, Ba and Má for always supporting me, even when I don't know how to express the true depth of my experiences and struggles in Vietnamese. Despite the

language barrier, I am always reminded of how unconditional love and support can transcend language, and especially through actions. With that, thank you for letting me pursue my career passions thousands of miles away from home and believing that I would define my own version of success. Although my time at Caltech will never be as hard as what you went through after the Vietnam war, my graduate school experience, in many ways, helped me sympathize more with your journey to America. What it was like to leave your family behind in pursuit of opportunity. How to adopt a language foreign to you. What it was like to feel lost and lonely. Reconciling the uncertainty of your future. Knowing enough to get by, and having just enough money to have a roof over your head. Meeting new friends and letting them help you through tough times, and so much more. The courage and resilience that you both showed while venturing into the unknown to achieve the American Dream was the very model that showed me what it would take to finish my PhD and the reward that it would offer at the very end.

To my dear cat Ada, thank you for joining my graduate school journey when you were only 3 months old. Despite me being a cat mom for the first time, you've been both patient and vocal whenever I forgot to do something for you. You've really been there through thick and thin, always keeping me company regardless of my mood when I came home. Your cuddles, silliness, and smiles really brightened up my time in graduate school and I couldn't be more grateful for your presence in my life.

Last but not least, I want to thank my fiance Vincent Nguyễn for showing me so much love and grace during my highest highs and my lowest lows during graduate school. Thank you for celebrating every small milestone with me and believing in me when I wanted to give up the most. You always reminded me of my inner strength to keep going and knew that my untapped potential was there the whole time. Your unconditional love and support truly helped me through it all, and I can't wait to spend my next chapter in life with you by my side.

ABSTRACT

Superionic conductors, or solid-state ion conductors that surpass the ionic conductivity of its liquid counterpart, can enable more energy dense batteries, robust artificial ion pumps, and optimized fuel cells. The mechanisms enabling superionic conductivity still remain elusive, though many-body correlations between the migrating ions, lattice vibrational modes, and charge screening clouds have all been posited to greatly enhance ionic conduction. Most spectroscopic techniques cannot directly probe and validate the role of such correlations due to their inability to transiently resolve these ultrafast dynamics occurring at picosecond timescales. In this work, we develop an ultrafast technique that measures the time-resolved change in impedance while a light source ranging from UV to THz frequencies selectively excites an ion-coupled correlation. The technique is used to compare the relative changes in impedance of a solid-state Li^+ conductor $Li_{0.5}La_{0.5}TiO_3$ (LLTO) before and after light excitation to elucidate the role of charge screening clouds, optical phonons, and acoustic phonons on ion migration. From our techniques, we determine that electronic screening and rocking phonon-mode interactions significantly dominate the ion migration pathway of LLTO compared to acoustic phonons. Although we only present one case study, our technique can extend to O^{2-}, H^+, or other charge carrier transport phenomena where ultrafast correlations control transport. Furthermore, the temporal relaxation of the measured impedance can distinguish ion transport effects caused by many-body correlations, optical heating, correlation, and memory behavior.

PUBLISHED CONTENT AND CONTRIBUTIONS

[1] **K. H. Pham**, V. Begum-Hudde, A. K. Lin, N. A. Spear, J. McClellan, M. Zuerch, A. Schleife, K. A. See, and S. K. Cushing. "The dynamical role of optical phonons and sub-lattice screening in a solid-state ion conductor". In: (Apr. 2025), Submitted. DOI: 10.48550/arXiv.2504.07249.

K.H.P. participated in the conception of the project, led the data collection and data analysis, and wrote the manuscript.

[2] **K. H. Pham**, K. Gordiz, N. A. Spear, A. K. Lin, J. Dallas, J. M. Michelsen, H. Liu, D. Vivona, G. A. Blake, Y. Shao-Horn, A. Henry, K. A. See, and S. K. Cushing. "Correlated Terahertz phonon-ion interactions dominate ion conduction in solid electrolyte $Li_{0.5}La_{0.5}TiO_3$". In: (Mar. 2024), Submitted. DOI: 10.48550/arXiv.2305.01632.

K.H.P. participated in the conception of the project, synthesized and prepared the sample for all measurements, collected impedance data, analyzed and prepared the data, and wrote the manuscript.

[3] **K. H. Pham**, A. K. Lin, N. A. Spear, and S. K. Cushing. "Laser-driven ultrafast impedance spectroscopy for measuring complex ion hopping processes". In: *Review of Scientific Instruments* 95.7 (July 2024), p. 073004. ISSN: 0034-6748. DOI: 10.1063/5.0182323.

K.H.P. participated in the conception of the project and development of the instrument, collected all of the ultrafast and variable power impedance data, analyzed and prepared the data, and wrote the manuscript.

[4] J. McClellan, A. Zong, **K. H. Pham**, H. Liu, Z. W. B. Iton, B. Guzelturk, D. A. Walko, H. Wen, S. K. Cushing, and M. W. Zuerch. "Hidden correlations in stochastic photoinduced dynamics of a solid-state electrolyte". In: (June 2024), Submitted. DOI: 10.48550/arXiv.2406.06832.

K.H.P. synthesized, characterized (structurally and electrochemically), and prepared the samples for the transient synchrotron X-ray diffraction experiments. K.H.P. conducted the solid-state NMR measurements and analyzed the corresponding data on the sample. K.H.P. helped write part of the manuscript.

[5] Z. P. Ifkovits, J. M. Evans, P. A. Kempler, M. B. Morla, **K. H. Pham**, J. A. Dowling, A. I. Carim, and N. S. Lewis. "Powdered $Mn_ySb_{1-y}O_x$ catalysts for cerium-mediated oxygen evolution in acidic environments". In: *ACS Energy Letters* 7.12 (Dec. 2022). Publisher: American Chemical Society, pp. 4258–4264. DOI: 10.1021/acsenergylett.2c01754.

K.H.P. prepared varying particle sizes of the powdered catalyst for experimentation.

CONTENTS

LIST OF FIGURES

LIST OF TABLES

NOMENCLATURE

$\rho_{\mathbf{O_h}}$. octahedral rocking modes.

$\mathbf{E_a}$. activation energy.

AC. alternating current.

CW. continuous wave.

DC. direct current.

DOS. density of states.

LLTO. $Li_{0.5}La_{0.5}TiO_3$.

MIR. mid infrared.

NIR. near infrared.

RF. radio frequency.

SEM. scanning electron microscopy.

SNR. signal to noise ratio.

SSE. solid-state electrolyte.

THz. terahertz.

UV. ulraviolet.

VNA. vector network analyzer.

FDTD. finite-difference time domain.

NEB. nudged elastic band.

PDOS. projected-density of states.

SFIT. single frequency transient impedance.

Chapter 1

INTRODUCTION

1.1 Mechanisms governing solid-state ion conduction

Partially adapted from: Kim H. Pham; Kiarash Gordiz; Natan A. Spear; Amy K. Lin; Jax Dallas; Jonathan M. Michelsen; Hanzhe Liu; Danielle Vivona; Yang Shao-Horn; Asegun Henry; Kimberly A. See; Scott K. Cushing. Correlated Terahertz phonon-ion interactions dominate ion conduction in solid electrolyte $Li_{0.5}La_{0.5}TiO_3$. *arXiv:2305.01632. Submitted.*

Solid-state electrolytes (SSEs) have applications in Li-ion batteries,[1] biological membranes,[2] solid oxide fuel cells,[3] and more. Ongoing research in this field has led to the discovery of superionic conductors, or those that surpass the conductivity of their liquid counterparts, which can enable energy dense solid-state electrochemical systems while maintaining fast conductive properties akin to liquids.[4–8] Realizing an all-solid-state battery comprising a superionic solid-state electrolyte and Li metal anode would meet the necessary commercial metrics for developing electric, long-range vehicles, and large-scale grid storage.[9]

The fundamental mechanism of ion conduction σ_{ion} relies on the Arrhenius form equation shown in Equation 1.1 where σ_{ion} is the Arrhenius prefactor, T is the temperature, E_a is the activation energy, and k_B is the Boltzmann constant.[10]

$$\sigma_{ion} = \sigma_0/T * exp(-E_a/k_BT) \tag{1.1}$$

Throughout literature, researchers have sought out different strategies to increase σ_{ion} by lowering the E_a of the ion migration pathway through targeting lattice structures with corner sharing frameworks[6] and connected migration channel, [9, 11] employing highly polarizable polyanions in the sub-lattice,[12, 13] introducing disorder to cation sites,[6, 8] and leveraging polyanion-motion-mediated ion transport.[14–16] These principles have led to the discovery of several superionic conductors through aliovalent/isovalent substitution strategies[17] and a general search for ideal structural families.[8, 13, 14, 16] For example, $Li_{10}GeP_2S_{12}$(LGPS),[4, 6, 7] $Li_7P_3S_{11}$(LPS),[6, 9, 14, 15] and Li-argyrodites[6, 8, 12] are extraordinarily

conductive, and are postulated to be related to concerted ion hopping mechanisms or polyanion rotational-assisted hopping.

More generally, dynamic lattice interactions with the hopping ion have been suggested to play a significant role in the ion conduction mechanism.[13, 18–21] For example, more polarizable anion sub-lattices will generally exhibit weaker bonding interactions with the migrating ion, flattening the energy landscape of the ion migration pathway. Lowering the average vibrational frequencies of the Li phonon band center is also a key design concept for enhanced ion migration.[13] Minimizing Coulombic interactions have also enabled high Li^+ conduction in $Li_6PS_{5-x}Se_xI$[22] and Li_6PS_5X,[12] and in some cases, competing inductive effects have overpowered the favorable flattening of the ion hopping energy landscape via "soft" lattices,[23, 24] challenging our understanding of how competing dynamical factors influence ion migration. A dynamic picture that includes couplings between the sub-lattice and the migrating ion, such as the vibrational movement of polyhedral orientations, or the Coulombic interactions between the migrating ion and sub-lattice, must be considered along with the static picture.[19, 21, 25]

A method to measure and quantify the interplay of lattice dynamic couplings is still underway. To understand the role of screening or phonon coupling, we can expand the pre-factor σ_0 in Equation 1.1. As shown in Equation 1.2, σ_0 depends on the entropy of migration ΔS_m and enthalpy of migration ΔH_m.

$$\sigma_{ion} = \sigma_0 \propto \exp\left(\frac{\Delta S_m}{k_B}\right) \exp\left(\frac{\Delta H_m}{k_B}\right) \tag{1.2}$$

The value of ΔS_m is determined by lattice dynamic couplings, like collective phonon-ion interactions [26] which are predicted to correlate with and enhance ionic conductivity.[13–21, 26–28] The value of ΔH_m is experimentally measured as the E_a, often with Electrochemical Impedance Spectroscopy (EIS) (determined by Equations 1.3 and 1.1) and Nuclear Magnetic Resonance (NMR).

While EIS cannot decouple conduction caused by multiple mobile charge carriers without the careful consideration of blocking and non-blocking electrodes, EIS remains a useful tool to study ionic conduction.[29] Experimentally, the measured Nyquist plots are fit to an equivalent circuit and used to extract a corresponding resistance value associated with, for instance, ion hopping at grain boundaries or through a bulk grain. The resistance can be used to calculate the ionic conductivity with Equation 1.3:

$$\sigma = \frac{l}{R_{total} * A} \tag{1.3}$$

where σ is the ionic conductivity, R_{total} is the impedance that is approximated as Z_L, l is the sample thickness, and A is the sample area.

Less experimental methods are available to probe the phonon-ion couplings predicted to relate to ΔS_m and are shown in Figure 1.1. NMR techniques have been used to probe phonon-ion coupling in Li-argyrodites[18, 30] and other conductive Li-sulfide, -nitride, and -oxides.[31] However, NMR can only probe dynamics on the megahertz timescale whereas lattice vibrational modes occur on the order of terahertz frequencies.[16, 31] Neutron scattering techniques have been applied to Na-sulfides and -selenides,[16, 19] as well as Na-orthophosphates and -sulphates,[16, 32] specifically by characterizing the reorientation of anions as quasi-elastic structure factors.[31, 32] Although promising, only a time-averaged structural picture of phonon-couplings has been achieved to date. Without time-resolved information, the precise timing of how and when the lattice vibrational modes interact with the ion moving along a single hopping trajectory can only be postulated.[16] Thus, the limited temporal resolution accessed by current spectroscopy techniques limits the ability to probe superionic transport mechanisms on its inherent timescales.[16] A spectroscopic technique that can probe hopping at ultrafast timescales up to picoseconds, but also the complex ion coupling interactions, would expand current knowledge in the field of solid-state ionics.

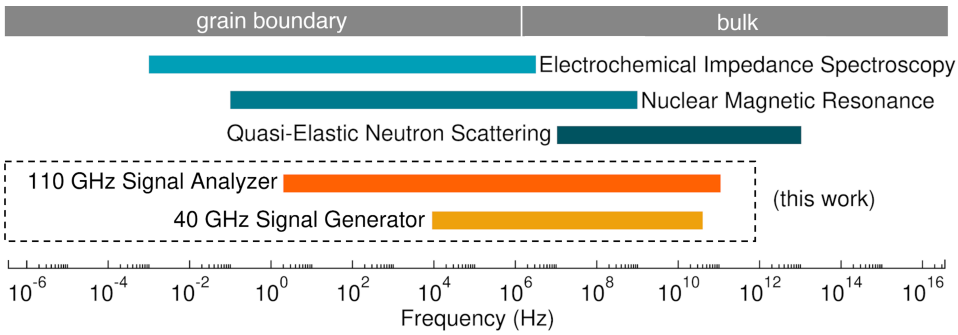

Figure 1.1: Comparison of common techniques that probe ionic conductivity at different frequency ranges and the corresponding hopping time regimes that can be accessed. The grain boundary and bulk ion hopping frequency ranges are approximated based on experiment for LLTO.

1.2 An ultrafast approach to studying ion hopping mechanisms

Partially adapted from: Kim H. Pham; Amy K. Lin; Natan A. Spear; Scott K. Cushing. Laser-driven ultrafast impedance spectroscopy for measuring complex ion hopping processes. *Review of Scientific Instruments* 2024, 95, 073004.

Ultrafast lasers can perturb phonon and electron interactions predicted to affect ion hopping.[33] Superionic conductors are predicted to have complex correlated ion-ion,[34] ion-phonon,[13, 14, 19, 28, 35] and ion-charge screening cloud interactions,[12, 21, 28] all of which can be studied with ultrafast ion hopping spectroscopy techniques.[33]

For instance, many-body type interactions influence ion conduction wherein the ion-host interaction can be perturbed using UV to THz light. For example, UV to visible light can photoexcite charge transfer transitions and create non-equilibrium carrier distributions to modulate screening effects[36–39] or even induce structural changes to enhance ion migration.[40] Near infrared to THz light can resonantly excite optical phonons,[41] phonon modes,[27, 35, 41–44] or trigger ion hopping.[35] Acoustic phonon modes can be selected by anharmonic or Raman interactions,[35] or incoherently heated as a reference.[42, 43]

Several attempts in applying ultrafast measurements to the study of superionic conductors have been reported in literature.[35, 45] Recently in one study, Poletayev et al used impulsive near-resonant terahertz excitation to trigger ion hopping in single-crystal beta-alumina and monitored the transient birefringence as a Terahertz Kerr Effect (TKE) signal, but does not directly probe the actual mobile ion hop.[35]

Even with the growth of new ultrafast spectroscopy techniques, ultrafast measurements are practically challenging because most ionic species do not have appreciable optical cross sections[33] nor do the devices that employ solid-state electrolytes operate under photo-excitation. Both challenges prevent the direct application of ultrafast pulsed laser techniques. While some successful cases exist, like 2D-Infrared spectroscopy of ionic liquids,[46] a signal corresponding to bulk ion transport versus the relaxation of a photoexcited electronic transition, vibrational excitation, or displacement field, is difficult to discern and assign in solids because the many-body correlations and heterogeneity convolute the data.[33] Developing an accurate and direct probe for capturing picosecond ion motion dynamics remains challenging.

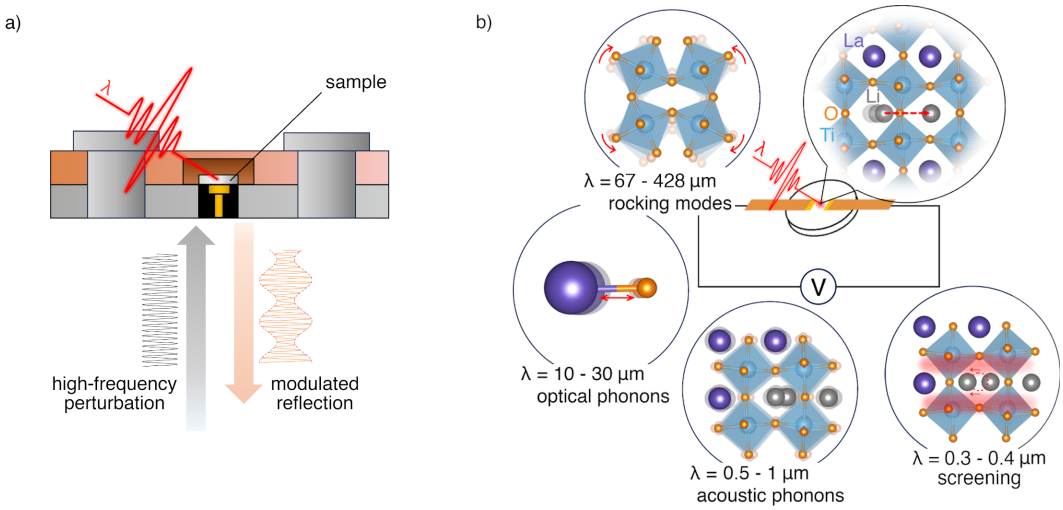

Figure 1.2: General schematic for laser-driven impedance measurements with ultrafast time-resolved and non-time resolved experimental schematics. (a) Sample schematic for ultrafast, time-resolved impedance measurements. An excitation source, λ, excites the sample, which, after an incoming carrier frequency that triggers ion hopping, the reflected amplitude modulated signal upon laser-excitation is retrieved for analysis. (b) General experimental schematic used for the non-time resolved laser-driven impedance measurements with LLTO. An excitation source, λ, excites the sample between two in-plane Au electrodes while EIS measurements are collected. Depending on the wavelength of the excitation source, rocking modes, optical phonons, acoustic phonons, and screening phenomena can be excited to influence the Li^+ migration in LLTO.

1.3 Thesis summary

The following chapters of this thesis outline the creation and application of a laser-driven ultrafast impedance method that can directly measure bulk ion conduction on the picosecond timescale and parse out many-body ion interactions. In particular, the role of optical phonons, acoustic phonons, and electrostatic screening are investigated in a solid-state electrolyte $Li_{0.5}La_{0.5}TiO_3$ (LLTO).

Chapter one describes the methodology of the technique and the practical implementation of the instrument. The described technique leverages communications-based signal generators and oscilloscopes that can apply AC potentials at frequencies from 1 mHz to 110 GHz and record the perturbation effect as a change in dB, current, or impedance. We demonstrate the capabilities of our instrument to capture impedance measurements at picoseconds timescales on LLTO under both steady-state and time-resolved conditions up to 110 GHz and 40 GHz respectively. Figure 1.2a generalizes the schematic for collecting such measurements in a reflection geometry. This work

has been published.

Chapter two focuses on the scientific application of the ultrafast, laser-driven impedance technique, described in chapter one, to study the role of photo-induced optical phonons and screening on ion migration triggered by an above-band gap, charge transfer excitation. We prove through experiment and theory that the opto-ionically induced phenomena directly enhances ion hopping both thermally and non-thermally, rather than photo-generating electron carriers. This work has been submitted.

Finally, chapter three describes the preliminary investigation of phonon-driven ion hopping demonstrated with non-time resolved impedance methods. We show that laser-driving the TiO_6 rocking modes decreases the measured impedance nearly ten-fold compared to exciting acoustic and optical phonons at similar energy densities. We compare and interpret our final results in the calculated ion migration enhancements achieved via above and below gap excitations, mid-IR, and THz frequencies as shown by the schematic in Figure 1.2b. All of the proposed wavelengths of light excite unique lattice dynamic interactions with the hopping ion. This work has been submitted.

References

[1] Shufeng Song, Ning Hu, and Li Lu. "Solid electrolytes for solid-state Li/Na-metal batteries: inorganic, composite and polymeric materials". In: *Chemical Communications* 58.86 (Oct. 27, 2022). Publisher: The Royal Society of Chemistry, pp. 12035–12045. ISSN: 1364-548X. DOI: 10.1039/D2CC04862K. URL: https://pubs.rsc.org/en/content/articlelanding/2022/cc/d2cc04862k (visited on 02/01/2023).

[2] Tingting Mei, Hongjie Zhang, and Kai Xiao. "Bioinspired artificial ion pumps". In: *ACS Nano* 16.9 (Sept. 27, 2022). Publisher: American Chemical Society, pp. 13323–13338. ISSN: 1936-0851. DOI: 10.1021/acsnano.2c04550. URL: https://doi.org/10.1021/acsnano.2c04550 (visited on 02/01/2023).

[3] Shichen Sun et al. "A focused review on structures and ionic conduction mechanisms in inorganic solid-state proton and hydride anion conductors". In: *Materials Advances* 4.2 (Jan. 23, 2023). Publisher: RSC, pp. 389–407. ISSN: 2633-5409. DOI: 10.1039/D2MA01003H. URL: https://pubs.rsc.org/en/content/articlelanding/2023/ma/d2ma01003h (visited on 02/01/2023).

[4] Arihant Bhandari and Jishnu Bhattacharya. "Origin of fast ion conduction in $Li_{10}GeP_2S_{12}$, a superionic conductor". In: *The Journal of Physical Chemistry*

C 120.51 (Dec. 29, 2016), pp. 29002–29010. ISSN: 1932-7447, 1932-7455. DOI: 10.1021/acs.jpcc.6b10967. URL: https://pubs.acs.org/doi/10.1021/acs.jpcc.6b10967 (visited on 06/06/2021).

[5] Yong-Seok Choi and Jae-Chul Lee. "Electronic and mechanistic origins of the superionic conductivity of sulfide-based solid electrolytes". In: *Journal of Power Sources* 415 (Mar. 1, 2019), pp. 189–196. ISSN: 0378-7753. DOI: 10.1016/j.jpowsour.2019.01.071. URL: https://www.sciencedirect.com/science/article/pii/S0378775319300813 (visited on 09/23/2022).

[6] KyuJung Jun et al. "Lithium superionic conductors with corner-sharing frameworks". In: *Nature Materials* 21.8 (Aug. 2022). Number: 8 Publisher: Nature Publishing Group, pp. 924–931. ISSN: 1476-4660. DOI: 10.1038/s41563-022-01222-4. URL: https://www.nature.com/articles/s41563-022-01222-4 (visited on 09/23/2022).

[7] Noriaki Kamaya et al. "A lithium superionic conductor". In: *Nature Materials* 10.9 (Sept. 2011), pp. 682–686. ISSN: 1476-1122, 1476-4660. DOI: 10.1038/nmat3066. URL: http://www.nature.com/articles/nmat3066 (visited on 06/05/2020).

[8] Marvin A. Kraft et al. "Inducing high ionic conductivity in the lithium superionic argyrodites $Li_{6+x}P_{1-x}Ge_xS_5I$ for all-solid-state batteries". In: *Journal of the American Chemical Society* 140.47 (Nov. 28, 2018). Publisher: American Chemical Society, pp. 16330–16339. ISSN: 0002-7863. DOI: 10.1021/jacs.8b10282. URL: https://doi.org/10.1021/jacs.8b10282 (visited on 10/12/2022).

[9] Arumugam Manthiram, Xingwen Yu, and Shaofei Wang. "Lithium battery chemistries enabled by solid-state electrolytes". In: *Nature Reviews Materials* 2.4 (Feb. 14, 2017). Number: 4 Publisher: Nature Publishing Group, pp. 1–16. ISSN: 2058-8437. DOI: 10.1038/natrevmats.2016.103. URL: https://www.nature.com/articles/natrevmats2016103 (visited on 09/29/2022).

[10] John B. Goodenough. "Review Lecture - Fast ionic conduction in solid". In: *Proceedings of the Royal Society of London. A. Mathematical and Physical Sciences* 393.1805 (Jan. 1997). Publisher: Royal Society, pp. 215–234. DOI: 10.1098/rspa.1984.0055. URL: https://royalsocietypublishing.org/doi/abs/10.1098/rspa.1984.0055 (visited on 02/21/2023).

[11] Dominik A. Weber et al. "Structural insights and 3D diffusion pathways within the lithium superionic conductor $Li_{10}GeP_2S_{12}$". In: *Chemistry of Materials* 28.16 (Aug. 23, 2016). Publisher: American Chemical Society, pp. 5905–5915. ISSN: 0897-4756. DOI: 10.1021/acs.chemmater.6b02424. URL: https://doi.org/10.1021/acs.chemmater.6b02424 (visited on 10/23/2024).

[12] Marvin A. Kraft et al. "Influence of lattice polarizability on the ionic conductivity in the lithium superionic argyrodites Li_6PS_5X (X = Cl, Br, I)". In: *Journal of the American Chemical Society* 139.31 (Aug. 9, 2017), pp. 10909–10918. ISSN: 0002-7863, 1520-5126. DOI: 10.1021/jacs.7b06327. URL: https://pubs.acs.org/doi/10.1021/jacs.7b06327 (visited on 06/06/2021).

[13] Sokseiha Muy et al. "Phonon–ion interactions: Designing ion mobility based on lattice dynamics". In: *Advanced Energy Materials* 11.15 (2021), p. 2002787. ISSN: 1614-6840. DOI: 10.1002/aenm.202002787. URL: https://onlinelibrary.wiley.com/doi/abs/10.1002/aenm.202002787 (visited on 10/10/2022).

[14] Zhizhen Zhang et al. "Targeting superionic conductivity by turning on anion rotation at room temperature in fast ion conductors". In: *Matter* 2.6 (June 3, 2020). Publisher: Elsevier, pp. 1667–1684. ISSN: 2590-2393, 2590-2385. DOI: 10.1016/j.matt.2020.04.027. URL: https://www.cell.com/matter/abstract/S2590-2385(20)30233-2 (visited on 10/12/2022).

[15] Jeffrey G. Smith and Donald J. Siegel. "Low-temperature paddlewheel effect in glassy solid electrolytes". In: *Nature Communications* 11.1 (Mar. 20, 2020). Number: 1 Publisher: Nature Publishing Group, p. 1483. ISSN: 2041-1723. DOI: 10.1038/s41467-020-15245-5. URL: https://www.nature.com/articles/s41467-020-15245-5 (visited on 10/14/2022).

[16] Zhizhen Zhang and Linda F. Nazar. "Exploiting the paddle-wheel mechanism for the design of fast ion conductors". In: *Nature Reviews Materials* 7.5 (May 2022). Number: 5 Publisher: Nature Publishing Group, pp. 389–405. ISSN: 2058-8437. DOI: 10.1038/s41578-021-00401-0. URL: https://www.nature.com/articles/s41578-021-00401-0.

[17] John Christopher Bachman et al. "Inorganic solid-state electrolytes for lithium batteries: mechanisms and properties governing ion conduction". In: *Chemical Reviews* 116.1 (Jan. 13, 2016). Publisher: American Chemical Society, pp. 140–162. ISSN: 0009-2665. DOI: 10.1021/acs.chemrev.5b00563. URL: https://doi.org/10.1021/acs.chemrev.5b00563 (visited on 09/29/2022).

[18] Isabel Hanghofer, Bernhard Gadermaier, and H. Martin R. Wilkening. "Fast rotational dynamics in argyrodite-Type Li_6PS_5X (X: Cl, Br, I) as seen by ^{31}P nuclear magnetic relaxation—on cation–anion coupled transport in thiophosphates". In: *Chemistry of Materials* 31.12 (June 25, 2019), pp. 4591–4597. ISSN: 0897-4756, 1520-5002. DOI: 10.1021/acs.chemmater.9b01435. URL: https://pubs.acs.org/doi/10.1021/acs.chemmater.9b01435 (visited on 12/08/2022).

[19] Thorben Krauskopf et al. "Comparing the descriptors for investigating the influence of lattice dynamics on ionic transport using the superionic conductor $Na_3 PS_{4-x}Se_x$ ". In: *Journal of the American Chemical Society* 140.43 (Oct. 31, 2018), pp. 14464–14473. ISSN: 0002-7863, 1520-5126. DOI: 10.

1021/jacs.8b09340. URL: https://pubs.acs.org/doi/10.1021/jacs.8b09340 (visited on 11/17/2022).

[20] Xinyu Li and Nicole A. Benedek. "Enhancement of ionic transport in complex oxides through soft lattice modes and epitaxial strain". In: *Chemistry of Materials* 27.7 (Apr. 14, 2015), pp. 2647–2652. ISSN: 0897-4756, 1520-5002. DOI: 10.1021/acs.chemmater.5b00445. URL: https://pubs.acs.org/doi/10.1021/acs.chemmater.5b00445 (visited on 10/24/2022).

[21] Sokseiha Muy et al. "Tuning mobility and stability of lithium ion conductors based on lattice dynamics". In: *Energy & Environmental Science* 11.4 (2018), pp. 850–859. ISSN: 1754-5692, 1754-5706. DOI: 10.1039/C7EE03364H. URL: http://xlink.rsc.org/?DOI=C7EE03364H (visited on 10/24/2022).

[22] Roman Schlem et al. "Changing the static and dynamic lattice effects for the improvement of the ionic transport properties within the argyrodite $Li_6PS_{5-x}Se_xI$". In: *ACS Applied Energy Materials* 3.1 (Jan. 27, 2020). Publisher: American Chemical Society, pp. 9–18. DOI: 10.1021/acsaem.9b01794. URL: https://doi.org/10.1021/acsaem.9b01794 (visited on 08/06/2024).

[23] Thorben Krauskopf, Sean P. Culver, and Wolfgang G. Zeier. "Bottleneck of diffusion and inductive effects in $Li_{10}Ge_{1-x}Sn_xP_2S_{12}$". In: *Chemistry of Materials* 30.5 (Mar. 13, 2018). Publisher: American Chemical Society, pp. 1791–1798. ISSN: 0897-4756. DOI: 10.1021/acs.chemmater.8b00266. URL: https://doi.org/10.1021/acs.chemmater.8b00266 (visited on 08/06/2024).

[24] Sean P. Culver et al. "Evidence for a solid-electrolyte inductive effect in the superionic conductor $Li_{10}Ge_{1-x}Sn_xP_2S_{12}$". In: *Journal of the American Chemical Society* 142.50 (Dec. 16, 2020). Publisher: American Chemical Society, pp. 21210–21219. ISSN: 0002-7863. DOI: 10.1021/jacs.0c10735. URL: https://doi.org/10.1021/jacs.0c10735 (visited on 08/06/2024).

[25] Saneyuki Ohno et al. "Materials design of ionic conductors for solid state batteries". In: *Progress in Energy* 2.2 (Mar. 2020). Publisher: IOP Publishing, p. 022001. ISSN: 2516-1083. DOI: 10.1088/2516-1083/ab73dd. URL: https://dx.doi.org/10.1088/2516-1083/ab73dd (visited on 08/06/2024).

[26] George H. Vineyard. "Frequency factors and isotope effects in solid state rate processes". In: *Journal of Physics and Chemistry of Solids* 3.1 (Jan. 1, 1957), pp. 121–127. ISSN: 0022-3697. DOI: 10.1016/0022-3697(57)90059-8. URL: https://www.sciencedirect.com/science/article/pii/0022369757900598 (visited on 11/17/2022).

[27] Michael Först et al. "Nonlinear phononics as an ultrafast route to lattice control". In: *Nature Physics* 7.11 (Nov. 2011). Number: 11 Publisher: Nature Publishing Group, pp. 854–856. ISSN: 1745-2481. DOI: 10.1038/nphys2055.

URL: https://www.nature.com/articles/nphys2055 (visited on 09/22/2022).

[28] Zhenming Xu et al. "Anharmonic cation–anion coupling dynamics assisted lithium-ion diffusion in sulfide solid electrolytes". In: *Advanced Materials* 34 (49), p. 2207411. ISSN: 49. DOI: 10.1002/adma.202207411. URL: https://onlinelibrary.wiley.com/doi/abs/10.1002/adma.202207411.

[29] John T. S. Irvine, Derek C. Sinclair, and Anthony R. West. "Electroceramics: Characterization by impedance spectroscopy". In: *Advanced Materials* 2.3 (Mar. 1990), pp. 132–138. ISSN: 0935-9648, 1521-4095. DOI: 10.1002/adma.19900020304. URL: http://doi.wiley.com/10.1002/adma.19900020304 (visited on 06/06/2021).

[30] Marina Brinek et al. "Structural disorder in Li_6PS_5I speeds ^{7}Li nuclear spin recovery and slows down ^{31}P relaxation–implications for translational and rotational jumps as seen by nuclear magnetic resonance". In: *The Journal of Physical Chemistry C* 124.42 (Oct. 22, 2020). Publisher: American Chemical Society, pp. 22934–22940. ISSN: 1932-7447. DOI: 10.1021/acs.jpcc.0c06090. URL: https://doi.org/10.1021/acs.jpcc.0c06090 (visited on 12/15/2022).

[31] Martin Wilkening and Paul Heitjans. "From micro to macro: Access to long-range Li^+ diffusion parameters in solids via microscopic $^{6,7}Li$ spin-alignment echo NMR spectroscopy". In: *ChemPhysChem* 13.1 (2012), pp. 53–65. ISSN: 1439-7641. DOI: 10.1002/cphc.201100580. URL: https://onlinelibrary.wiley.com/doi/abs/10.1002/cphc.201100580.

[32] Dirk Wilmer et al. "Sodium ion conduction in plastic phases: dynamic coupling of cations and anions in the picosecond range". In: *Journal of Materials Research* 20.8 (Aug. 1, 2005), pp. 1973–1978. ISSN: 0884-2914, 2044-5326. DOI: 10.1557/JMR.2005.0277. URL: http://link.springer.com/10.1557/JMR.2005.0277 (visited on 12/08/2022).

[33] Margherita Maiuri, Marco Garavelli, and Giulio Cerullo. "Ultrafast spectroscopy: State of the art and open challenges". In: *Journal of the American Chemical Society* 142.1 (Jan. 8, 2020). Publisher: American Chemical Society, pp. 3–15. ISSN: 0002-7863. DOI: 10.1021/jacs.9b10533. URL: https://doi.org/10.1021/jacs.9b10533 (visited on 05/05/2023).

[34] Xingfeng He, Yizhou Zhu, and Yifei Mo. "Origin of fast ion diffusion in super-ionic conductors". In: *Nature Communications* 8.1 (June 21, 2017). Publisher: Nature Publishing Group, p. 15893. ISSN: 2041-1723. DOI: 10.1038/ncomms15893. URL: https://www.nature.com/articles/ncomms15893 (visited on 08/06/2024).

[35] Andrey D. Poletayev et al. "The persistence of memory in ionic conduction probed by nonlinear optics". In: *Nature* 625.7996 (Jan. 2024). Publisher: Nature Publishing Group, pp. 691–696. ISSN: 1476-4687. DOI: 10.1038/

s41586-023-06827-6. URL: https://www.nature.com/articles/s41586-023-06827-6 (visited on 03/05/2024).

[36] Tae-Youl Yang et al. "The significance of ion conduction in a hybrid organic–inorganic lead-iodide-based perovskite photosensitizer". In: *Angewandte Chemie International Edition* 54.27 (2015), pp. 7905–7910. ISSN: 1521-3773. DOI: 10.1002/anie.201500014. URL: https://onlinelibrary.wiley.com/doi/abs/10.1002/anie.201500014 (visited on 06/07/2023).

[37] Taeyong Kim et al. "Mapping the pathways of photo-induced ion migration in organic-inorganic hybrid halide perovskites". In: *Nature Communications* 14.1 (Apr. 3, 2023). Number: 1 Publisher: Nature Publishing Group, p. 1846. ISSN: 2041-1723. DOI: 10.1038/s41467-023-37486-w. URL: https://www.nature.com/articles/s41467-023-37486-w (visited on 06/07/2023).

[38] Gee Yeong Kim et al. "Large tunable photoeffect on ion conduction in halide perovskites and implications for photodecomposition". In: *Nature Materials* 17.5 (May 2018). Number: 5 Publisher: Nature Publishing Group, pp. 445–449. ISSN: 1476-4660. DOI: 10.1038/s41563-018-0038-0. URL: https://www.nature.com/articles/s41563-018-0038-0 (visited on 06/07/2023).

[39] Thomas Defferriere et al. "Photo-enhanced ionic conductivity across grain boundaries in polycrystalline ceramics". In: *Nature Materials* 21.4 (Apr. 2022). Number: 4 Publisher: Nature Publishing Group, pp. 438–444. ISSN: 1476-4660. DOI: 10.1038/s41563-021-01181-2. URL: https://www.nature.com/articles/s41563-021-01181-2 (visited on 05/09/2023).

[40] Anna Lee et al. "Photo-accelerated fast charging of lithium-ion batteries". In: *Nature Communications* 10.1 (Oct. 30, 2019). Number: 1 Publisher: Nature Publishing Group, p. 4946. ISSN: 2041-1723. DOI: 10.1038/s41467-019-12863-6. URL: https://www.nature.com/articles/s41467-019-12863-6 (visited on 05/09/2023).

[41] Michael Först, Roman Mankowsky, and Andrea Cavalleri. "Mode-selective control of the crystal lattice". In: *Accounts of Chemical Research* 48.2 (Feb. 17, 2015). Publisher: American Chemical Society, pp. 380–387. ISSN: 0001-4842. DOI: 10.1021/ar500391x. URL: https://doi.org/10.1021/ar500391x (visited on 05/09/2023).

[42] Kiarash Gordiz et al. "Enhancement of ion diffusion by targeted phonon excitation". In: *Cell Reports Physical Science* 2.5 (May 19, 2021), p. 100431. ISSN: 2666-3864. DOI: 10.1016/j.xcrp.2021.100431. URL: https://www.sciencedirect.com/science/article/pii/S2666386421001260 (visited on 09/22/2022).

[43] Kim H. Pham et al. “Correlated Terahertz phonon-ion interactions dominate ion conduction in solid electrolyte $Li_{0.5}La_{0.5}TiO_3$”. In: arXiv:2305.01632 (Mar. 6, 2024). DOI: 10.48550/arXiv.2305.01632. arXiv: 2305.01632[cond-mat,physics:physics]. URL: http://arxiv.org/abs/2305.01632 (visited on 03/09/2024).

[44] Tobia F. Nova et al. “An effective magnetic field from optically driven phonons”. In: *Nature Physics* 13.2 (Feb. 2017). Number: 2 Publisher: Nature Publishing Group, pp. 132–136. ISSN: 1745-2481. DOI: 10.1038/nphys3925. URL: https://www.nature.com/articles/nphys3925 (visited on 10/10/2022).

[45] Tomohide Morimoto et al. “Microscopic ion migration in solid electrolytes revealed by terahertz time-domain spectroscopy”. In: *Nature Communications* 10.1 (June 17, 2019). Number: 1 Publisher: Nature Publishing Group, p. 2662. ISSN: 2041-1723. DOI: 10.1038/s41467-019-10501-9. URL: https://www.nature.com/articles/s41467-019-10501-9 (visited on 09/22/2022).

[46] Amr Tamimi and Michael D. Fayer. “Ionic liquid dynamics measured with 2D IR and IR pump–probe experiments on a linear anion and the influence of potassium cations”. In: *The Journal of Physical Chemistry B* 120.26 (July 7, 2016). Publisher: American Chemical Society, pp. 5842–5854. ISSN: 1520-6106. DOI: 10.1021/acs.jpcb.6b00409. URL: https://doi.org/10.1021/acs.jpcb.6b00409 (visited on 05/05/2023).

Chapter 2

CONSTRUCTION OF A LASER-DRIVEN, ULTRAFAST IMPEDANCE SPECTROMETER

ABSTRACT

Partially adapted from: Kim H. Pham; Amy K. Lin; Natan A. Spear; Scott K. Cushing. Laser-driven ultrafast impedance spectroscopy for measuring complex ion hopping processes. *Review of Scientific Instruments* 2024, 95, 073004.

Superionic conductors, or solid-state ion-conductors surpassing 0.01 S/cm in conductivity, can enable more energy dense batteries, robust artificial ion pumps, and optimized fuel cells. However, tailoring superionic conductors requires precise knowledge of ion migration mechanisms that are still not well understood, due to limitations set by available spectroscopic tools. Most spectroscopic techniques do not probe ion hopping at its inherent picosecond timescale, nor the many-body correlations between the migrating ions, lattice vibrational modes, and charge screening clouds—all of which are posited to greatly enhance ionic conduction. In previous literature, Fast Fourier Transform (FFT) EIS, online EIS, and fast-time resolved techniques have been reported that are like the methodologies presented here, relying on a perturbing signal that effects a measurable quantity like current. However, we report, to our knowledge, the first method that can reach up to 110 GHz which has previously been capped between 1-200 kHz for real-time measurements.

We develop an ultrafast technique that measures the time-resolved change in impedance upon light excitation which triggers selective ion-coupled correlations. The technique is used to compare the relative changes in impedance of a solid-state Li^+ conductor LLTO before and after UV excitation to elucidate the corresponding ion-many-body-interaction correlations. From our techniques, we determine that electronic screening and phonon-mode interactions dominate the ion migration pathway of LLTO. Although we only present one case study, our technique can extend to O^{2-}, H^+, or other charge carrier transport phenomena where ultrafast correlations control transport. Furthermore, the temporal relaxation of the measured impedance can distinguish ion transport effects caused by many-body correlations, optical heating, correlation, and memory behavior.

2.1 Theory of high frequency impedance measurements

Ultrafast spectroscopy techniques typically rely on a pump-probe type experiment, where an ultrafast laser pump initiates a non-equilibrium population from which decay and scattering constants can be measured via the probe. In the linear limit, these timescales are assigned to a rare event near equilibrium, such as a thermally activated ion hops, by fluctuation-dissipation theory.[1] Although our technique superficially is akin to pump-probe spectroscopy with an ultrafast pump laser, our technique differs because the ultrafast laser pulse does not trigger the ion hop. To drive ion hopping, a DC or AC potential must be applied with a magnitude strong enough to overcome the hopping activation energy. In solid-state ion conductors, the magnitude of the potential can range from 10 mV to 1 V before non-linear effects occur. Applying an AC field (as opposed to DC) avoids polarization at the electrode interface, which is the operating principle of EIS, and here enables the transient investigation of electrochemical processes unachievable with DC fields.[2, 3]

In the case of an AC potential or perturbation, its frequency determines what dynamic will be probed based on the dynamic's respective time constant, where the time constant τ is the product of resistance R and capacitance C. A low frequency perturbation (<kHz) probes slow processes with large time constants, like ion hopping across grain boundaries which have larger impedances. A high frequency perturbation (>MHz-GHz) probes fast processes, like single or multiple ion hops. Those processes have smaller impedances and capacitances because less energy barriers are encountered for a single ion hop versus the multiple barriers required to hop across the entire electrolyte.

Then, the ultrafast laser can drive electronic transitions to alter Coulombic interactions,[4] phonons to change the local energy minima along the hopping,[5] or adjacent ions to reveal possible migration pathways–all of which are predicted to couple to the hopping ion. Therefore, the experimental technique enables the study of ion-coupled migration phenomena at different hopping regimes at timescales set by the bandwidth of the AC field frequencies that can be generated as shown in Figure 2.1.

Like in the case of EIS, an AC potential perturbing the sample of interest can be described with Equation 2.1, where $V(t)$ is the potential as a function of time t, V_0 is the amplitude of the potential, and f is the frequency:[6]

$$V(t) = V_0 * sin(2\pi * ft) \tag{2.1}$$

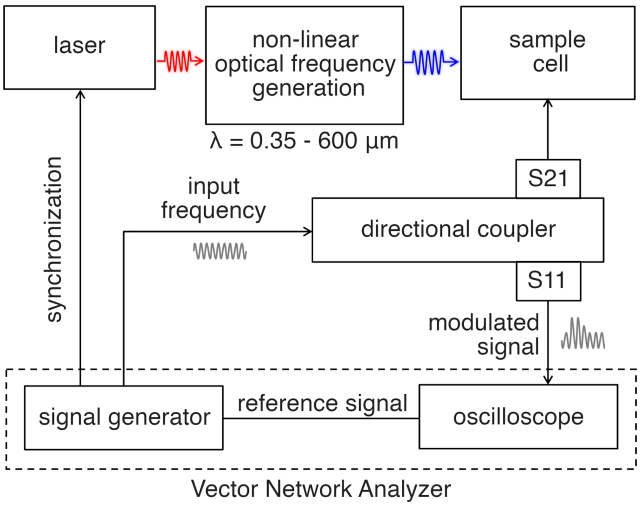

Figure 2.1: Schematic of the time-resolved ultrafast impedance set up, including the laser, a representative nonlinear frequency generation process (to cover the UV to THz excitation range), vector network analyzer, and the sample cell.

The interaction with the sample will cause a change in the phase and amplitude of the measured response (as current or potential) as shown in Equation 2.2, where $I(t)$ is the current as a function of time, I_0 is the amplitude of the current, and Θ is the phase angle. Equation 2.2 can also be rewritten for a change in potential.

$$I(t) = I_0 * sin(2\pi * ft + \Theta) \tag{2.2}$$

The complex impedance can then be derived from the amplitude $Z = V_0/I_0$ and phase angle, i.e., the phase shift between the measured $V(t)$ and $I(t)$ for a frequency f.

In previous literature, FFT EIS,[7–9] online EIS,[10, 11] and fast-time resolved techniques[9, 12, 13] have been developed to both measure the impedance and access faster hopping regimes, but are often limited to 1-3 GHz. We report, to our knowledge, the first method that can reach up to 40-110 GHz due to recent advances in electronics, with previous reports only reaching 1-3 GHz.[6, 9, 10, 14] Ultimately, the bandwidth of the signal generator and oscilloscope determines the temporal and frequency resolution, and using frequency extenders could soon extend measurement capabilities to THz frequencies.

To construct a time-resolved impedance measurement technique, a signal generator that can generate frequencies up to 40-110 GHz is used as the driving AC field to

match the timescales of the ultrafast ion hopping in a bulk grain, shown in Figure 1.1.

The oscilloscope would then measure the potential change, current change, and phase shift for the same frequencies, all of which are used to derive impedance. Above tens of MHz, directly measuring the current or potential change can be on the order of sub-picofarad and sub-nanohenry,[15] so the use of specialized electronics for high-speed detection of small currents and potential changes is critical. Vector Network Analyzers, for instance, can detect such small signal and provide measurements in the form of scattering parameters which derive from current and potential signals, measured in dBm.[15] Scattering parameters are useful measurements that help determine how a sample under test interacts with different waveforms by either transmitting or reflecting some fraction of an input signal. The derivation linking scattering parameters to current and voltage is described further in Appendix A.

Specifically, the reflectance signal (S11) measured at the coupled port is the ratio of the is the reflected signal measured at port 1 from the test port (b_1) and the input RF signal in volts of dB (a_1), if the boundary conditions $a_2 = 0$ (at the port 2 output) holds as shown in Equation 2.3. The S11 parameter can also be represented as the reflection scattering parameter Γ. The transmission signal measured at the test port (S21) is the ratio of the signal transmitted to the load and the input RF signal as shown in Equation 2.4.

$$S11 = \left.\frac{b_1}{a_1}\right|_{a_2=0} \tag{2.3}$$

$$S21 = \left.\frac{b_2}{a_1}\right|_{a_2=0} \tag{2.4}$$

The measurement of the reflection signal to obtain part of the sample impedance can be loosely described by Equations 2.5-2.7 where VSWR is the voltage standing wave ratio, or the efficiency of transmission of a radio frequency power source to the load though a transmission line, $S11$ is the reflection scattering parameter, Γ is the reflection coefficient, Z_0 is the reference ohm (typically 50 ohm), and Z_L is the sample impedance or load. A more complete interpretation of scattering parameters and its connection to impedance and ionic conductivity is described further in Appendix A and in reference [16] by Kuek Chee Yaw.

$$VSWR = \frac{1 + |S11|}{1 - |S11|} \tag{2.5}$$

$$\Gamma = \frac{VSWR - 1}{VSWR + 1} \tag{2.6}$$

$$Z_L = Z_0 \frac{1 + \Gamma}{1 - \Gamma} \tag{2.7}$$

In the experimental set up as shown in Figure 2.1, an input RF signal can be sent to the sample at port $S21$, or the test port, via a directional coupler. The characteristic reflection signal determines how the sample interacts with the input frequency. Since the reflection signal is measured directly from the Vector Network Analyzer (VNA) via a directional coupler, the Z_L can be calculated and used to roughly estimate the ionic conductivity. The transmission signal can also be calculated to understand how the sample in study changes the input waveform, but is beyond the scope of this study.[17] From reflection and transmission measurements, the sample impedance can be measured to determine the complex conductivity.

To connect the sample to the directional coupler, a vertical launch is used which contains a conductive pin that electronically contacts the sample in series in a transmission line geometry[18] as shown in Figure 2.2.

The experimental geometry can be modeled as a simple circuit like EIS, where the sample has an associated resistance and capacitance in parallel with the resistance of the short as described in previous literature and mentioned in more depth in Chapter 2.2. Additionally, by adding the copper plate as a short in the circuit, the conditions required for the reflection measurement is met, or i.e., ensuring that $a_2 = 0$. A microstrip line type geometry is configured for measurements below 32 MHz measurements in this work, but can also be optimized for measurements above 1 GHz. In a transmission line or microstrip geometry, the $S21$ can be measured to obtain the transmission coefficient which can be used to determine the complete complex impedance together with the measured reflection signal. In this work, we focus on the experimental set up of only reflection measurements which is described in more detail in the next section.

2.2 General instrument construction

A schematic of the instrument is shown in Figure 2.1. For the excitation laser source, a Ti:Sapphire laser oscillator and amplifier (Legend Elite and Astrella-V-

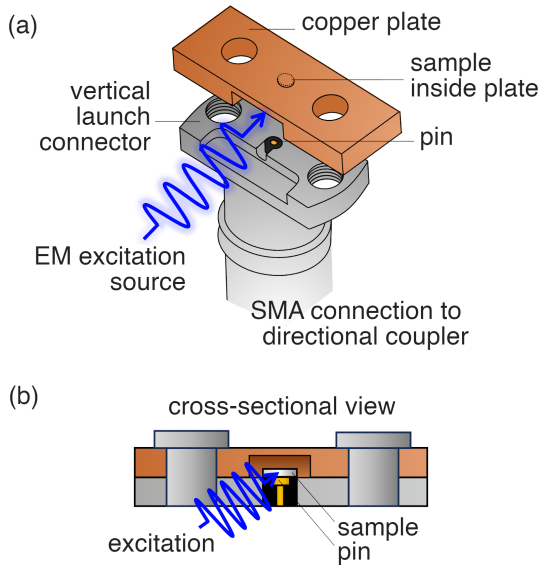

Figure 2.2: Ultrafast impedance sample holder. (a) Schematic of the sample holder. The exposed pin from the vertical launch makes electrical contact with the sample under study. (b) A cross-sectional view of the sample holder. A cavity is machined out from the side of the copper plate to expose the sample for irradiation

USP) from Coherent are used to create the visible to THz light from non-linear optical frequency generation methods. UV to NIR light is created using an optical parametric amplifier (TOPAS) and NirUVis from Light Conversion. 350 nm light is generated using fourth harmonic generation from the TOPAS and NirUVIS. A 349 nm laser diode (Explorer One 349-60, Spectra-physics, 60 uJ pulse energy, 1 kHz repetition rate) is also used for comparison with UV light. Difference frequency generation is used to cover the 5 to 15 μm range. THz frequencies are generated using a DAST crystal and the 1400 nm output of the optical parametric amplifier, described in more detail in Chapter 4.3.

A 2 Hz – 110 GHz Keysight N9041B UXA Signal Analyzer is employed as a VNA for steady-state measurements. To measure the time-resolved impedance signal, a 40 GHz, Keysight, N5173B EXG X-Series Microwave Analog Signal Generator coupled with a Keysight UXR0334A Infiniium UXR Real-time 33 GHz, 128 GSa/s, 13.3 ps rise-time Oscilloscope is used. The noise floor determines the lowest differential signal that can be measured and depends on the exact signal generator and oscilloscope used. With the described equipment, a signal to noise ratio of 10^{-4}-10^{-6} is possible.

For reflection measurements, the VNA generates an AC signal that transmits to the

sample, or load, via a directional coupler with an SMA connection into the sample and a copper short at the test port with circuit modeling reported from previous literature[14, 19, 20] as shown in Figure 2.1. A cavity is drilled out from the side of the copper short to allow laser excitation during the time-resolved measurements as shown in Figure 2.2. The powder sample is densified into a 2 mm diameter pellet under high force (up to 2 tons), or 6.25 GPa of pressure, annealed to achieve at least 80% of its theoretical density (specific to the composition), and subsequently ground to fit inside the 300 μm well. In addition to minimizing air gaps, the sample must make physical contact with the pin inside of the vertical launch connector to create a resonator, which is critical for accurate measurements.[17, 21] The RF input perturbs the sample at the test port and the resulting perturbation is measured at the coupled port ($S11$) to measure the reflected wave. To physically measure the $S11$ parameter, the sample adopts a transmission line configuration with the internal pin of the vertical launch, enabling high frequency transmission to over 10 GHz.[15] The electrical connection between the sample, contacting pin, and the oscilloscope is established with a co-axial cable with appropriate adapters rated for GHz frequencies, such as SMA connections.

The laser clock can be used as an external reference to phase sync with the custom VNA, but in some cases, syncing can be difficult because of excessive clock jitter from the pulse laser arrival and signal generator. Many signal generators only accept a 10 MHz reference signal that a laser clock will not output. Even after frequency dividing the laser clock output to achieve 10 MHz, the resulting signal may not have sufficient phase stability. An IQ demodulation approach could help to then extract the amplitude and phase information. Here, a 35-picosecond photodiode is used to phase sync the signal by triggering off the 1 kHz laser. Next, the reflection measurement is conducted for a combination of varying laser excitation frequencies and signal generator frequencies, depending on the experiment.

2.3 Demonstration of the capabilities of a laser-driven, ultrafast impedance spectrometer

LLTO is used as the test sample for the developed instrument due to its stability in air,[22] and well characterized ion migration pathway,[23] band gap energy,[24] vibrational modes,[25] and phonon modes,[26, 27] all of which are predicted to be involved in ionic conduction. LLTO experimentally crystallizes in the R$\bar{3}$m space group as an orthorhombic or pseudo-cubic perovskite with an ABO_3 structure as shown in Figure 2.3, where the Li and La occupy the A-site and Ti occupies the

B-site. Li^+ conduction in LLTO is mediated by adjacent vacancies in between bottlenecks formed by four oxygens from four corner shared TiO_6 octahedra.[23, 25]

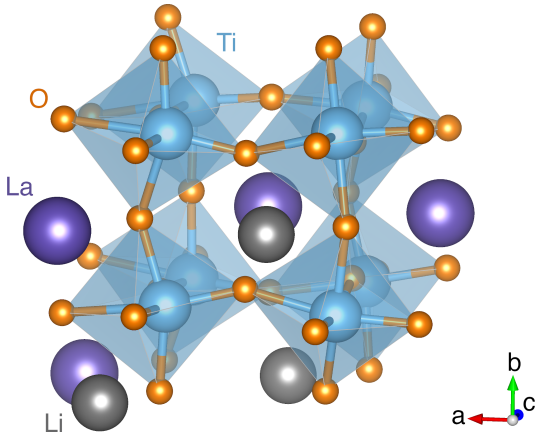

Figure 2.3: Crystal structure of LLTO, where the La, Li, Ti, and O are purple, gray, blue, and orange, respectively.

The exact lattice-dynamic correlations are investigated in more depth in Chapters 3 and 4. In Chapter 3, the dynamical role of optical phonons and sub-lattice screening triggered by an above-band gap excitation are explored. In Chapter 4, the role of phonon-coupled ion dynamics are explored.

For the initial demonstration of the described ultrafast impedance techniques, we probe the role of screening effects and optical phonons via an above-band gap excitation on LLTO. Screening effects have been predicted to aid ionic conduction by minimizing electrostatic interactions between the host lattice and migrating ion, enabling fast ion migration for several solid-state Li^+ and O^{2-} conductors.[4, 28–30] In LLTO, a ligand to-metal charge transfer transition can occur upon band gap excitation (see Chapter 3.2) which promotes electronic carriers from the O 2p orbitals to the Ti 3d orbitals.[24] By transferring charge density from the O 2p orbitals to the Ti 3d orbitals, the electrostatic hindrance in the ion conduction pathway is likely reduced, leading to a lower activation energy. The effects triggered by the UV excitation are compared to 700-800 nm light which is sufficiently below the band gap energy and should only induce thermal effects. Additionally, the time constant associated with bulk ion hopping is reported to be on the order of nanoseconds for LLTO, indicating that measurements using GHz frequencies should be able to detect modulations related to the hopping ion.[31]

LLTO was synthesized according to literature.[22] A stoichiometric amount of La_2O_3, Li_2CO_3, and TiO_2 were mixed in an agate mortar and pressed into pellets under 100 MPa of pressure. The pellets were placed on a bed of sacrificial powder and calcined at 800°C for 4 hours and heated to 1200°C for 12 hours at a 1°C per minute ramp rate[22]. The following material was routinely characterized using a Rigaku X-ray diffractometer with CuKα radiation and scanned from 20 to 80 2θ at a scan rate of 0.4° per second as shown in Figure 2.4.

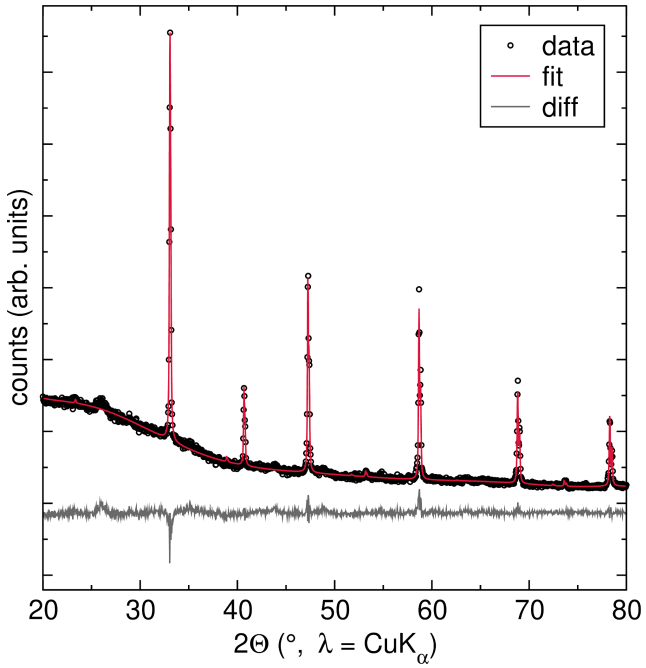

Figure 2.4: X-ray diffraction of LLTO using the CuK_α source. Small peaks found below 30 2θ correspond to impurities.

The following X-ray diffraction pattern was fitted using a Rietveld refinement with the GSAS II software. High resolution synchrotron powder diffraction data were collected using beamline 11-BM at the Advanced Photon Source, Argonne National Laboratory as shown in Figure 2.5.

Scanning electron microscopy (SEM) was taken (Figure 2.6a) looking down the cross-section, and (Figure 2.6b) on the surface of an annealed LLTO pellet. SEM was performed using the SE2 detector of a ZEISS 1550VP field emission SEM with an acceleration voltage of 10 kV at 10xK magnification.

To prepare the sample for ultrafast impedance tests, the resulting powder was pressed into a pellet with a diameter of 2 mm and a thickness of 500 μm under 6.25 GPa of

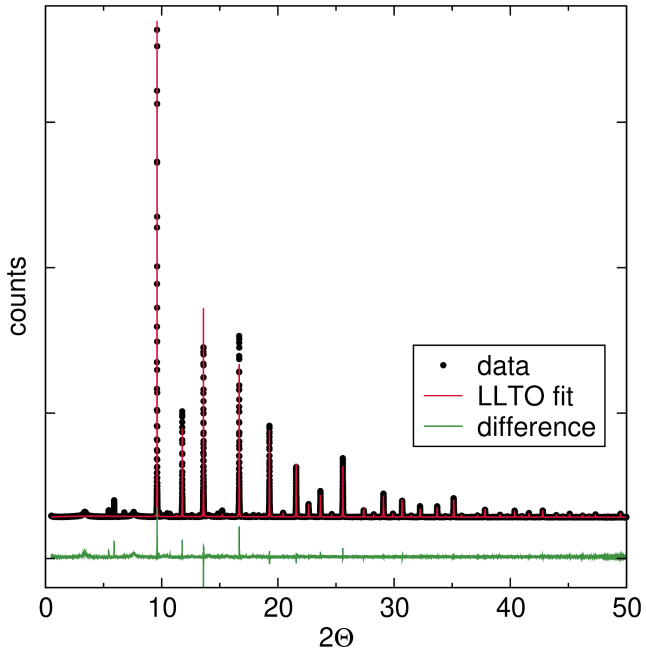

Figure 2.5: Synchrotron X-ray diffraction of LLTO. Small peaks found below 10 2θ correspond to impurities.

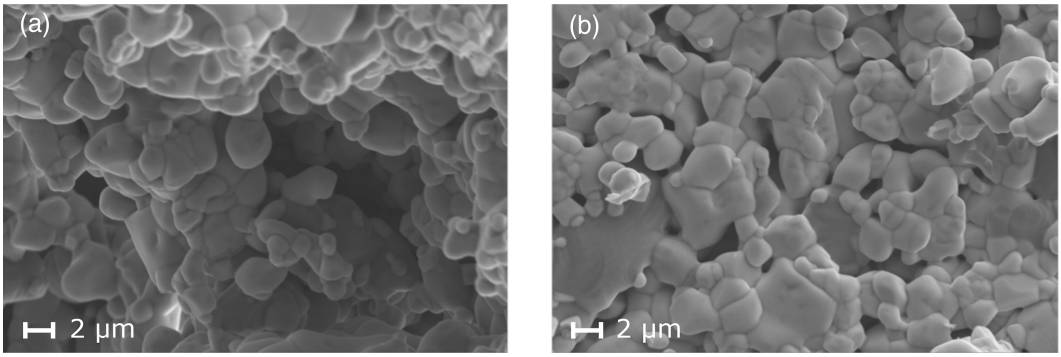

Figure 2.6: SEM image of LLTO (a) looking down the cross-section, and (b) on the surface of the annealed LLTO pellet. Grains are 1-10 μm in size.

pressure. The pellet was subsequently annealed at 1100°C for 6 h at a ramp rate of 2°C per minute over a bed of its mother powder. The sample was then ground down to 300 μm using 1500 grit SiC paper to fit within the empty cavity of the vertical launch geometry (Figure 2.2) that includes a side cavity through which the sample is excited.

Steady-state measurements up to 110 GHz

The 2 Hz – 110 GHz Keysight N9041B UXA Signal Analyzer is used to perform steady state measurements on LLTO upon CW 350 nm and 700 nm excitation to explore the conceptual capabilities of the instrument before the application of time-resolved experiments. The use of a CW source is crucial to prevent the decay of excited processes slower than the laser repetition rate, in this case slower than 1 kHz. The VNA is, at its essence, a coupled signal generator and oscilloscope, enabling direct comparisons between steady-state and time-resolved measurements. The reflection signal is Fourier-filtered to remove the carrier signal frequencies and is used to calculate Z_L using Equation 2.5-2.7. The Z_L can then be used to calculate the ionic conductivity using Equation 1.3.

An optical, above band gap excitation is achieved by accessing the LLTO sample through the cavity in the vertical launch geometry. The steady-state response is measured and used to calculate and plot the enhancement ratio $\Delta\sigma/\sigma$ as a function of frequency as shown in Figure 2.7, which combines the low frequency range of an impedance analyzer and higher frequency ranges of the Vector Network Analyzer. The plot shows the enhancement in conductivity of LLTO after photo-excitation with a 350 nm CW laser at approximately 500 mW. The shaded red region in Figure 2.7 shows the difference in the changed ionic conductivity due to laser heating of the incoherent phonon bath with 700 nm light at similar powers versus the modulated Li^+-electron coupling from the 350 nm band gap excitation. The largest increase in the enhancement ratio is observed in the site-to-site hopping region below 1 GHz and is likely due to the shift in charge density from the O 2p to Ti 3d orbitals which we predict to lower the activation energy for the ion hop. The differences observed due to the 350 nm and 700 nm at the grain boundary and across the electrode-electrolyte surface regions is also observed and are likely related to the population of thermal baths.

Beyond 1 GHz, the steady-state noise exceeds the signal measurements and begins to reach the limit suggested by the reported time constant for LLTO, determined by EIS.[31] Additionally, the vertical launch configuration acts as a poor resonator, also limiting measurement capabilities at high GHz frequencies. A printed circuit geometry could be designed to address such noise issues and optimize the measurement.

Although the generation of electronic carriers can convolute the quantification of Li^+ mobility via EIS, the electronic and ionic conductivities can be deconvoluted by

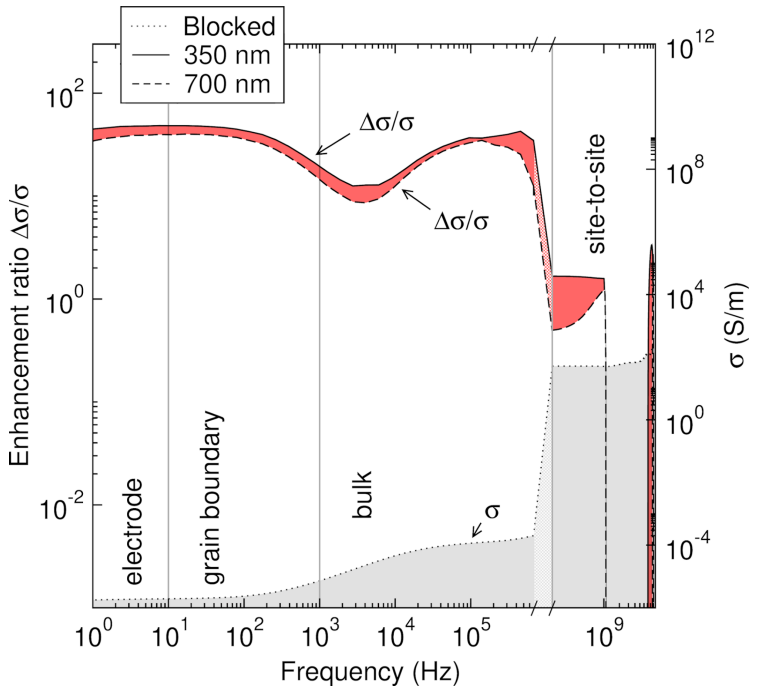

Figure 2.7: The enhancement ratio or change in ionic conductivity of LLTO from 2 Hz to 110 GHz. The excitation of the charge-transfer transition reduces the coulombic hopping barrier, increasing conductivity, shown as the black solid line. The differential change between the 700 nm and 350 nm excitation, shown as the red area, is greater than optically heating the lattice (black dashed line). The black dotted line shows the conductivity of LLTO with the blocked laser. The light red and gray area indicates unmeasured regions in the data.

other experimental methods like DC polarization or Hall-effect measurements.[28–30] In Chapter 3.6, we demonstrate the near-negligible contribution of electronic carriers compared to ionic carriers experimentally via DC polarization experiments. Our observed results corroborate the fact that the reported electronic conductivity of LLTO is four to five orders of magnitude lower than the ionic conductivity, so an extraordinarily large enhancement would have to take place to make the electronic carriers as mobile as the ionic ones. Such enhancements in electronic conductivity have not been observed using photoconductivity measurements on similar materials like TiO_2.[32, 33] As discussed more in Chapter 3, we believe our observations of enhanced ion migration due to this charge transfer process holds, after accounting for heat generation (with the 700 nm excitation) and electronic carrier generation.

One practical limitation with the steady-state measurements is the ability to accurately capture modulations that occur faster than the laser repetition rate, which certainly cannot be ruled out in the measurements shown in Figure 2.7. Thus, we

propose and use the time-resolved custom VNA set up described in Chapter 2 to measure the nanosecond modulations at picosecond timescales. This proposed time-resolved set up is demonstrated to address concerns proposed by the steady-state measurements.

Time-resolved measurements up to 33 GHz

The custom, time-resolved version of the VNA comprising the 40 GHz signal generator and 33 GHz real-time oscilloscope is used to measure the time resolved enhancement in ionic conduction in LLTO due to an above and below band gap excitation.

A 350 nm, fs pulsed beam focused to approximately 800-900 μm in diameter is used for the above band gap excitation. The below band gap, 800 nm, fs pulsed beam approximately 3,000 μm in diameter is focused through a 7.56 cm focal lens to excite the sample. The sample cell configuration shown in Figure 2.2 is used to conduct the measurement and follows the experimental configuration shown in Figure 2.1.

Figure 2.8 shows the direct AC voltage measurement at the $S11$ port with and without the 800 nm, using a 19 GHz, 19 dBm high frequency carrier signal to drive the ion hopping in LLTO. A 20 mW, 800 nm source is focused with a 76 mm focal lens to approximately 50 microns in diameter to excite the sample.

A very small low frequency modulation is barely detectable on the AC voltage measurement occurring between 0 – 200 ps without internal averaging, but ultimately results in an amplitude modulated signal. To improve the noise, the internal hardware averaging is applied and set to 1024 averages to improve the signal quality. To extract the low frequency modulation from the high frequency carrier signal and achieve high signal to noise measurements, an amplitude demodulation function is applied afterward, such that an envelope detector and low-pass filter removes the carrier signal and leaves behind the low frequency modulation, i.e., the signal caused by the light excitation.[34] A more detailed description of the amplitude demodulation function is described in Appendix B. As shown in Figure 2.8b, the amplitude demodulated signal reveals an impulse peak followed by a growth and decay of the signal over 1 ns. The noise can be further reduced by subsequently averaging the amplitude demodulated signal with 1024 averages. The low-pass filter can be applied on top of the averaged signal to further reduce the noise but should be used with caution to avoid completely removing a signal that would otherwise

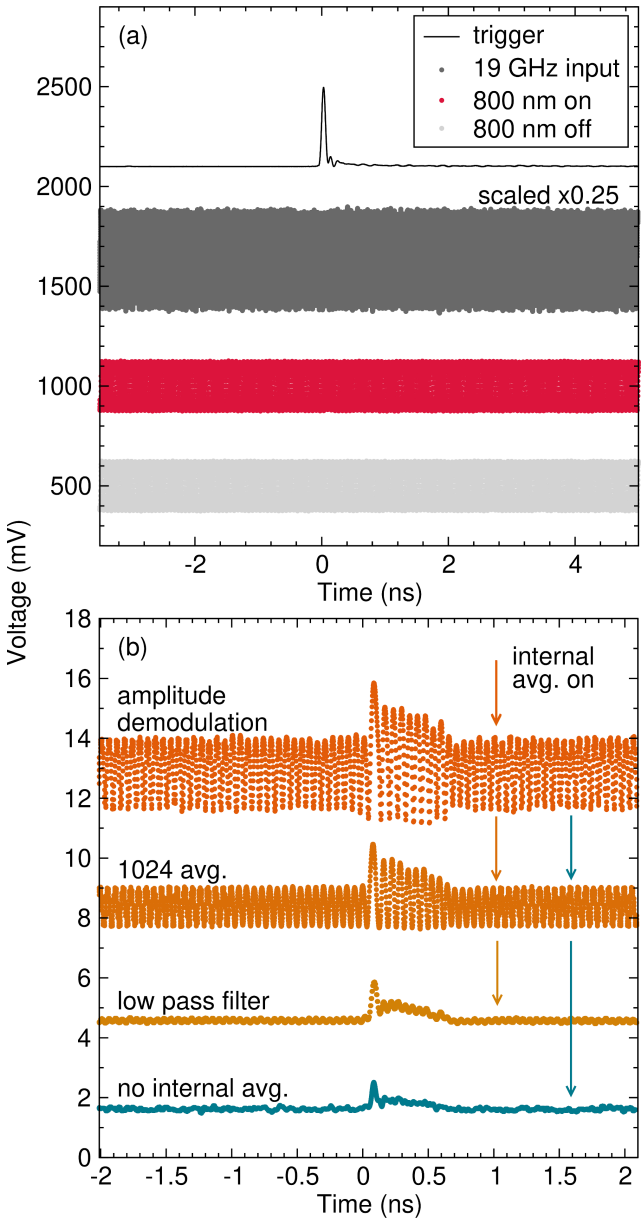

Figure 2.8: Raw and processed ultrafast, time-resolved impedance measurements. (a) A voltage versus time trace of the 800 nm trigger source (black), 19 GHz 19 dBm signal at the S21 port (dark gray), reflected sample signal upon 800 nm excitation (red), and blocked sample signal (light gray). The signals show the accumulated waveform over the collection time of the real-time oscilloscope. The sine wave is not phase-synchronized with the laser because of the high timing jitter of the laser oscillators. (b) The amplitude demodulated signals from the raw red trace obtained in (a), showing the sequential application of software functions to recover the low frequency demodulated signal and optimize signal to noise. Note that the amplitude demodulation, 1024 avg., and low pass filter functions all have the internal hardware averages set to 1024 avg. The bottom teal trace has no internal hardware averages on but contains the same applied functions showed in the above three traces.

be present. The gradual appearance of the nanosecond signal originates from increasing occupation of the acoustic phonon bath, which is similar to raising the sample temperature. While deserving further investigation, the measured nanosecond dynamics can be compared to the standard response of most transition metal oxide semiconductors to ultrafast laser pulses. Following the optical excitation, the electron bath of these materials thermalize by interacting with optical phonons on the few picosecond timescale. Acoustic phonons can also be involved in electron thermalization, but are predominately excited when the optical phonon bath decays into acoustic phonons like that shown for Li_3PO_4,[35] occurring at tens of picoseconds. At nanosecond timescales, all added heat and energy into the system eventually recombines and is lost to the environment.[36–39]

To confirm that the 350 nm excitation alters the ion migration mechanism of LLTO differently via the charge-transfer excitation versus the 800 nm excitation, a 13 mW, 350 nm beam (800-900 microns in diameter) is excited onto the sample. Due to the low efficiency of fourth harmonic generation, a similar average power of 20 mW could not be achieved like the 800 nm source and necessitated a larger spot size to excite more of the sample volume, at the expense of slightly lower power for the time-resolved measurement. As shown in Figure 2.9, the 350 nm excitation results in the appearance of an impulse limited response, similar to the 800 nm.

However, a distinct decay with a time constant of roughly 100 ps is the only feature for the 350 nm signal. In the 800 nm case, there is a growth and decay after the impulse response. Since the timescale observed for the 350 nm signal corresponds to optical phonons, the charge transfer transition likely modifies the 4-O bottleneck optical phonons that gate ion transport.

To obtain measurements like the steady state measurements in Figure 2.7, a frequency sweep is performed on the custom VNA to show how the sample signal changes with carrier frequency. As a proof of concept, we conduct a frequency sweep from 2 - 32 GHz for both the 800 nm excitation and the 350 nm excitation as shown in Figure 2.10a-b and 2.10c-d, respectively.

For the 800 nm excitation frequency sweep data, the characteristic modulation observed in Figure 2.9 is shown to persist between 16 to 32 GHz while at frequencies below 16 GHz, the characteristic shape disappears. A low pass filter is applied to the measurements in 2.10a-b to optimize the signal to noise. The bandwidth for the filter is adjusted to be less than 50-70% of the carrier frequency signal to reduce noise and not remove any characteristic features associated with the

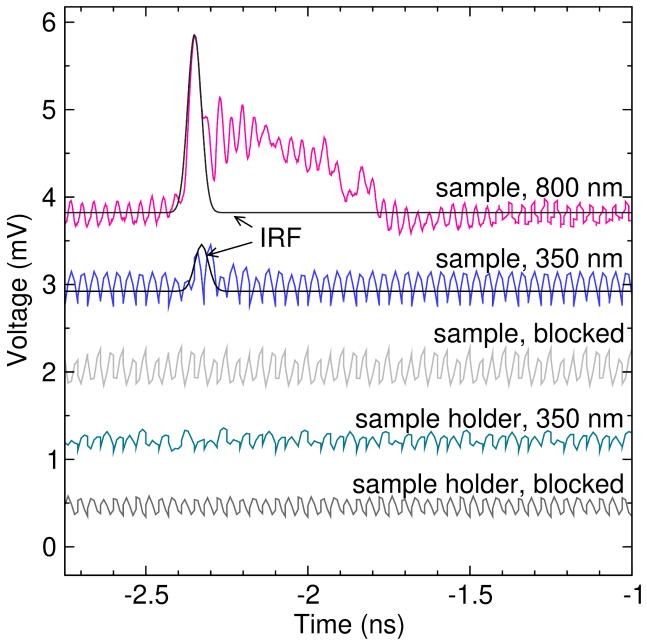

Figure 2.9: Comparison of modulation responses from the blocked and unblocked 800 and 350 nm excitations with the sample and sample holder. The black lines represent the instrument response function (IRF), with a bandwidth cutoff of 33 GHz. The input carrier frequency is at 28 GHz and 19 dBm for the 800 nm measurement and 10 dBm for the 350 nm measurement. The amplitude is optimized to obtain the best signal to noise ratio. The 800 nm excitation is offset by approximately -2.3 ns to compare the characteristics signal peaks with the 350 nm.

sample signal. For the frequency sweep of the sample excited at 350 nm, the characteristic signal seems consistent between 26–32 GHz and variable in shape below 26 GHz. We hypothesize that the characteristic signal becomes more distorted at lower frequencies because of the sample holder geometry's inability to amplify the resonant signal in addition to our current setup using excessively lossy cables for lower frequency ranges. Further work is needed to explore and optimize the described experimental methodology to extend measurements to lower frequencies, in addition to measurements at high GHz frequencies through optimization of the sample holder and sample size. Ultimately, the time resolved data at the picosecond timescale gives insight to how site-to-site hopping is influenced by screening at the local scale which has, to our knowledge, never been demonstrated previously. Our technique would expand existing knowledge on how the unique local structure of hopping channels collectively influences ionic conduction. Even though our observations and hypotheses are preliminary and require more studies to conclude the true nature of the temporal features, we still demonstrate the ability to measure

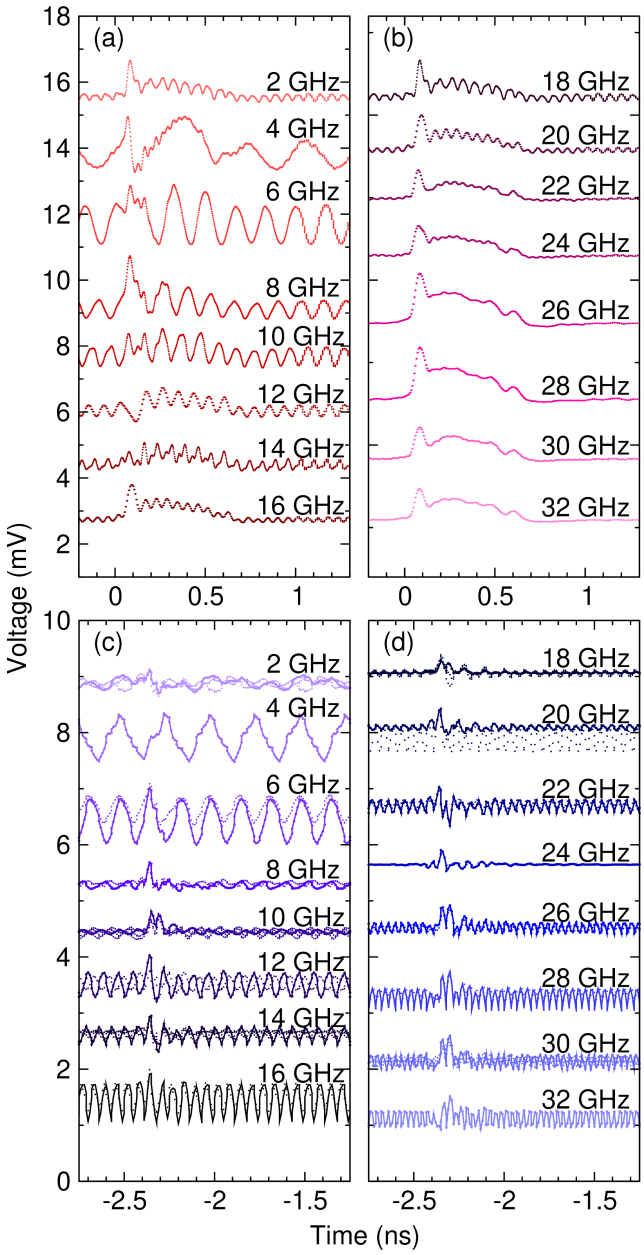

Figure 2.10: Comparison of modulation responses from the blocked and unblocked 800 nm excitation using (a) 2 to 16 GHz and (b) 18 to 32 GHz carrier frequencies, and 350 nm excitations using (c) 2 to 16 GHz and (d) 18 to 32 GHz carrier frequencies. The black lines represent the instrument response function (IRF), with a bandwidth cutoff of 33 GHz. The input carrier frequency is at 28 GHz and 19 dBm for the 800 nm measurement and 10 dBm for the 350 nm measurement. The amplitude is optimized to obtain the best signal to noise ratio. The 350 nm excitation is offset by approximately -2.3 ns to compare the characteristics signal peaks with the 800 nm.

picosecond ion hopping dynamics and correlate the observed lifetimes with optical

and acoustic phonons. In the next two chapters, we further explore the role of lattice dynamic correlations triggered by impulse light on ion migration by measuring the resulting change in impedance with second to picosecond time resolution.

The work presented in this chapter was possible through financial support from the National Science Foundation and Air Force Office of Science & Research (FA9550-21-1-0022).

References

[1] Ryogo Kubo. "The fluctuation-dissipation theorem". In: *Reports on Progress in Physics* 29.1 (Jan. 1966), p. 255. ISSN: 0034-4885. DOI: 10.1088/0034-4885/29/1/306. URL: https://dx.doi.org/10.1088/0034-4885/29/1/306 (visited on 08/14/2023).

[2] Shangshang Wang et al. "Electrochemical impedance spectroscopy". In: *Nature Reviews Methods Primers* 1.1 (June 10, 2021). Number: 1 Publisher: Nature Publishing Group, pp. 1–21. ISSN: 2662-8449. DOI: 10.1038/s43586-021-00039-w. URL: https://www.nature.com/articles/s43586-021-00039-w (visited on 05/01/2023).

[3] John T. S. Irvine, Derek C. Sinclair, and Anthony R. West. "Electroceramics: Characterization by impedance spectroscopy". In: *Advanced Materials* 2.3 (Mar. 1990), pp. 132–138. ISSN: 0935-9648, 1521-4095. DOI: 10.1002/adma.19900020304. URL: http://doi.wiley.com/10.1002/adma.19900020304 (visited on 06/06/2021).

[4] Thomas Defferriere et al. "Photo-enhanced ionic conductivity across grain boundaries in polycrystalline ceramics". In: *Nature Materials* 21.4 (Apr. 2022). Number: 4 Publisher: Nature Publishing Group, pp. 438–444. ISSN: 1476-4660. DOI: 10.1038/s41563-021-01181-2. URL: https://www.nature.com/articles/s41563-021-01181-2 (visited on 05/09/2023).

[5] Sokseiha Muy et al. "Phonon–ion interactions: Designing ion mobility based on lattice dynamics". In: *Advanced Energy Materials* 11.15 (2021), p. 2002787. ISSN: 1614-6840. DOI: 10.1002/aenm.202002787. URL: https://onlinelibrary.wiley.com/doi/abs/10.1002/aenm.202002787 (visited on 10/10/2022).

[6] G. S. Popkirov and R. N. Schindler. "A new impedance spectrometer for the investigation of electrochemical systems". In: *Review of Scientific Instruments* 63.11 (Nov. 1992), pp. 5366–5372. ISSN: 0034-6748, 1089-7623. DOI: 10.1063/1.1143404. URL: http://aip.scitation.org/doi/10.1063/1.1143404 (visited on 04/17/2023).

[7] Sam. C. Creason, John W. Hayes, and Donald E. Smith. "Fourier transform faradaic admittance measurements III. Comparison of measurement efficiency for various test signal waveforms". In: *Journal of Electroanalytical Chemistry and Interfacial Electrochemistry* 47.1 (Sept. 25, 1973),

pp. 9–46. ISSN: 0022-0728. DOI: 10.1016/S0022-0728(73)80343-2. URL: https://www.sciencedirect.com/science/article/pii/S0022072873803432 (visited on 04/17/2023).

[8] Aušra Valiūnienė et al. "Towards the application of fast Fourier transform - scanning electrochemical impedance microscopy (FFT-SEIM)". In: *Journal of Electroanalytical Chemistry* 864 (May 1, 2020), p. 114067. ISSN: 1572-6657. DOI: 10.1016/j.jelechem.2020.114067. URL: https://www.sciencedirect.com/science/article/pii/S1572665720302502 (visited on 04/17/2023).

[9] Chao Lyu et al. "A Fast Time Domain Measuring Technique of Electrochemical Impedance Spectroscopy Based on FFT". In: *2018 Prognostics and System Health Management Conference (PHM-Chongqing)*. 2018 Prognostics and System Health Management Conference (PHM-Chongqing). ISSN: 2166-5656. Oct. 2018, pp. 450–455. DOI: 10.1109/PHM-Chongqing.2018.00083.

[10] Zhiyong Xia and Jaber A. Abu Qahouq. "High Frequency Online Battery Impedance Measurement Method Using Voltage and Current Ripples Generated by DC-DC Converter". In: *2020 IEEE Applied Power Electronics Conference and Exposition (APEC)*. 2020 IEEE Applied Power Electronics Conference and Exposition (APEC). ISSN: 2470-6647. Mar. 2020, pp. 1333–1338. DOI: 10.1109/APEC39645.2020.9124465.

[11] Zhiyong Xia and Jaber A. Abu Qahouq. "Method for online battery AC impedance spectrum measurement using dc-dc power converter duty-cycle control". In: *2017 IEEE Applied Power Electronics Conference and Exposition (APEC)*. 2017 IEEE Applied Power Electronics Conference and Exposition (APEC). ISSN: 2470-6647. Mar. 2017, pp. 1999–2003. DOI: 10.1109/APEC.2017.7930973.

[12] G. S. Popkirov. "Fast time-resolved electrochemical impedance spectroscopy for investigations under nonstationary conditions". In: *Electrochimica Acta*. Electrochemical Impendance Spectroscopy 41.7 (May 1, 1996), pp. 1023–1027. ISSN: 0013-4686. DOI: 10.1016/0013-4686(95)00434-3. URL: https://www.sciencedirect.com/science/article/pii/00134686%5C%5C95004343 (visited on 04/17/2023).

[13] Taesic Kim, Wei Qiao, and Liyan Qu. "Real-time state of charge and electrical impedance estimation for lithium-ion batteries based on a hybrid battery model". In: *2013 Twenty-Eighth Annual IEEE Applied Power Electronics Conference and Exposition (APEC)*. 2013 Twenty-Eighth Annual IEEE Applied Power Electronics Conference and Exposition (APEC). ISSN: 1048-2334. Mar. 2013, pp. 563–568. DOI: 10.1109/APEC.2013.6520266.

[14] Algimantas Kežionis et al. "Broadband high frequency impedance spectrometer with working temperatures up to 1200K". In: *Solid State Ionics*. 9th International Symposium on Systems with Fast Ionic Transport 188.1 (Apr. 22,

2011), pp. 110–113. ISSN: 0167-2738. DOI: 10.1016/j.ssi.2010.09.034. URL: https://www.sciencedirect.com/science/article/pii/S0167273810005370 (visited on 06/08/2023).

[15] Peter C. L. Yip. *High-Frequency Circuit Design and Measurements*. 1st. Chapman & Hall, 1990. 224 pp.

[16] Kuek Chee Yaw. *Measurement of Dielectric Material Properties*. Retrieved from https://scdn.rohde-schwarz.com/ur/pws/dl_downloads/dl_application/00 aps_undefined/RAC-0607-0019_1_5E.pdf.

[17] Michael Steer. *Fundamentals of Microwave and RF Design*. 3rd.

[18] Maria A. Stuchly and Stanislaw S. Stuchly. "Coaxial Line Reflection Methods for Measuring Dielectric Properties of Biological Substances at Radio and Microwave Frequencies-A Review". In: *IEEE Transactions on Instrumentation and Measurement* 29.3 (1980), pp. 176–183. ISSN: 0018-9456. DOI: 10.1109/TIM.1980.4314902. URL: http://ieeexplore.ieee.org/document/4314902/ (visited on 03/03/2024).

[19] Nathaniel. E. Hager III. "Broadband time-domain-reflectometry dielectric spectroscopy using variable-time-scale sampling". In: *Review of Scientific Instruments* 65 (Apr. 1, 1994). ADS Bibcode: 1994RScI...65..887H, pp. 887–891. ISSN: 0034-6748. DOI: 10.1063/1.1144917. URL: https://ui.adsabs.harvard.edu/abs/1994RScI...65..887H (visited on 08/14/2023).

[20] Robert. H. Cole et al. "Time domain reflection methods for dielectric measurements to 10 GHz". In: *Journal of Applied Physics* 66.2 (July 15, 1989), pp. 793–802. ISSN: 0021-8979. DOI: 10.1063/1.343499. URL: https://doi.org/10.1063/1.343499 (visited on 08/14/2023).

[21] *Basics of measuring the dielectric properties of materials*. https://www.keysight.com/us/en/assets/7018-01284/application-notes/5989-2589.pdf.

[22] Jean. L. Fourquet, H. Duroy, and M. P. Crosnier-Lopez. "Structural and microstructural studies of the series $La_{3/2-x}Li_{3x}\square_{1/3-2x}TiO_3$". In: *Journal of Solid State Chemistry* 127.2 (Dec. 1, 1996), pp. 283–294. ISSN: 0022-4596. DOI: 10.1006/jssc.1996.0385. URL: https://www.sciencedirect.com/science/article/pii/S0022459696903850 (visited on 10/19/2022).

[23] Sonia Stramare, Venkataraman Thangadurai, and Werner. Weppner. "Lithium lanthanum titanates: A review". In: *Chemistry of Materials* 15.21 (Oct. 2003), pp. 3974–3990. ISSN: 0897-4756, 1520-5002. DOI: 10.1021/cm0300516. URL: https://pubs.acs.org/doi/10.1021/cm0300516 (visited on 06/06/2021).

[24] Lu Zhang et al. "Lithium lanthanum titanate perovskite as an anode for lithium ion batteries". In: *Nature Communications* 11.1 (Dec. 2020), p. 3490. ISSN: 2041-1723. DOI: 10.1038/s41467-020-17233-1. URL: http://www.nature.com/articles/s41467-020-17233-1 (visited on 06/06/2021).

[25] Xin Guo, Pardha Saradhi Maram, and Alexandra Navrotsky. "A correlation between formation enthalpy and ionic conductivity in perovskite-structured $Li_{3x}La_{0.67-x}TiO_3$ solid lithium ion conductors". In: *Journal of Materials Chemistry A* 5.25 (2017), pp. 12951–12957. ISSN: 2050-7488, 2050-7496. DOI: 10.1039/C7TA02434G. URL: http://xlink.rsc.org/?DOI=C7TA02434G (visited on 06/07/2021).

[26] Kim H. Pham et al. "Correlated Terahertz phonon-ion interactions dominate ion conduction in solid electrolyte $Li_{0.5}La_{0.5}TiO_3$". In: arXiv:2305.01632 (Mar. 6, 2024). DOI: 10.48550/arXiv.2305.01632. arXiv: 2305.01632[cond-mat,physics:physics]. URL: http://arxiv.org/abs/2305.01632 (visited on 03/09/2024).

[27] Tomas Šalkus et al. "Peculiarities of ionic transport in LLTO solid electrolytes". In: *physica status solidi c* 6.12 (2009), pp. 2756–2758. ISSN: 1610-1642. DOI: https://doi.org/10.1002/pssc.200982527. URL: https://onlinelibrary.wiley.com/doi/abs/10.1002/pssc.200982527 (visited on 06/07/2021).

[28] Tae-Youl Yang et al. "The significance of ion conduction in a hybrid organic–inorganic lead-iodide-based perovskite photosensitizer". In: *Angewandte Chemie International Edition* 54.27 (2015), pp. 7905–7910. ISSN: 1521-3773. DOI: 10.1002/anie.201500014. URL: https://onlinelibrary.wiley.com/doi/abs/10.1002/anie.201500014 (visited on 06/07/2023).

[29] Taeyong Kim et al. "Mapping the pathways of photo-induced ion migration in organic-inorganic hybrid halide perovskites". In: *Nature Communications* 14.1 (Apr. 3, 2023). Number: 1 Publisher: Nature Publishing Group, p. 1846. ISSN: 2041-1723. DOI: 10.1038/s41467-023-37486-w. URL: https://www.nature.com/articles/s41467-023-37486-w (visited on 06/07/2023).

[30] Gee Yeong Kim et al. "Large tunable photoeffect on ion conduction in halide perovskites and implications for photodecomposition". In: *Nature Materials* 17.5 (May 2018). Number: 5 Publisher: Nature Publishing Group, pp. 445–449. ISSN: 1476-4660. DOI: 10.1038/s41563-018-0038-0. URL: https://www.nature.com/articles/s41563-018-0038-0 (visited on 06/07/2023).

[31] Chunhua H. Chen and Khalil Amine. "Ionic conductivity, lithium insertion and extraction of lanthanum lithium titanate". In: *Solid State Ionics* 144.1 (Sept. 1, 2001), pp. 51–57. ISSN: 0167-2738. DOI: 10.1016/S0167-2738(01)00884-0. URL: https://www.sciencedirect.com/science/article/pii/S0167273801008840 (visited on 05/09/2024).

[32] Katerina. Pomoni, Anthanassios. Vomvas, and Christos. Trapalis. "Electrical conductivity and photoconductivity studies of TiO_2 sol–gel thin films and the effect of N-doping". In: *Journal of Non-Crystalline Solids*. Functional and

Nanostructured Materials 354.35 (Oct. 1, 2008), pp. 4448–4457. ISSN: 0022-3093. DOI: 10.1016/j.jnoncrysol.2008.06.069. URL: https://www.sciencedirect.com/science/article/pii/S0022309308004456 (visited on 07/18/2024).

[33] Ruan Shuang Chen et al. "Photoconduction Properties in Single-Crystalline Titanium Dioxide Nanorods with Ultrahigh Normalized Gain". In: *The Journal of Physical Chemistry C* 116.6 (Feb. 16, 2012). Publisher: American Chemical Society, pp. 4267–4272. ISSN: 1932-7447. DOI: 10.1021/jp209999j. URL: https://doi.org/10.1021/jp209999j (visited on 07/18/2024).

[34] David A. Rice, V. Venkatachalam, and Matt J. Wegmann. "A simple envelope detector". In: *IEEE Transactions on Instrumentation and Measurement* 37.2 (June 1988), pp. 223–226. ISSN: 00189456. DOI: 10.1109/19.6056. URL: http://ieeexplore.ieee.org/document/6056/ (visited on 03/06/2024).

[35] Qiwei Hu et al. "Anharmonic lattice dynamics dominated ion diffusion in γ-Li_3PO_4". In: *Journal of Solid State Chemistry* 333 (May 1, 2024), p. 124636. ISSN: 0022-4596. DOI: 10.1016/j.jssc.2024.124636. URL: https://www.sciencedirect.com/science/article/pii/S0022459624000902 (visited on 06/13/2024).

[36] Ye-Jin Kim et al. "Coherent charge hopping suppresses photoexcited small polarons in $ErFeO_3$ by antiadiabatic formation mechanism". In: *Science Advances* 10.12 (Mar. 20, 2024). Publisher: American Association for the Advancement of Science, eadk4282. DOI: 10.1126/sciadv.adk4282. URL: https://www.science.org/doi/10.1126/sciadv.adk4282 (visited on 06/13/2024).

[37] Hanzhe Liu et al. "Measuring photoexcited electron and hole dynamics in ZnTe and modeling excited state core-valence effects in transient extreme ultraviolet reflection spectroscopy". In: *The Journal of Physical Chemistry Letters* 14.8 (Mar. 2, 2023). Publisher: American Chemical Society, pp. 2106–2111. DOI: 10.1021/acs.jpclett.2c03894. URL: https://doi.org/10.1021/acs.jpclett.2c03894 (visited on 06/13/2024).

[38] Scott K. Cushing et al. "Hot phonon and carrier relaxation in Si(100) determined by transient extreme ultraviolet spectroscopy". In: *Structural Dynamics* 5.5 (Sept. 11, 2018), p. 054302. ISSN: 2329-7778. DOI: 10.1063/1.5038015. URL: https://doi.org/10.1063/1.5038015 (visited on 06/13/2024).

[39] Lucas M. Carneiro et al. "Excitation-wavelength-dependent small polaron trapping of photoexcited carriers in α-Fe_2O_3". In: *Nature Materials* 16.8 (Aug. 2017). Publisher: Nature Publishing Group, pp. 819–825. ISSN: 1476-4660. DOI: 10.1038/nmat4936. URL: https://www.nature.com/articles/nmat4936 (visited on 06/13/2024).

Chapter 3

ULTRAFAST TIME-RESOLVED PHOTO-MODULATION OF OPTICAL PHONON-ION COUPLINGS AND ELECTROSTATIC SCREENING DYNAMICS

ABSTRACT

Partially adapted from: Kim H. Pham, Vijaya Begum-Hudde, Amy K. Lin, Natan A. Spear, Jackson McClellan, Michael Zuerch, Andre Schleife, Kim A. See, and Scott K. Cushing. "The dynamical role of optical phonons and sub- lattice screening in a solid-state ion conductor". *arXiv:2504.07249. Submitted.*

Although numerous candidate SSEs have been discovered, the underlying mechanisms enabling superionic conduction remain elusive. In particular, the role of ultrafast lattice dynamics in mediating ion migration, which involves couplings between ions, phonons, and electrons, is rarely explored experimentally at their corresponding timescales. To investigate the complex contributions of coupled lattice dynamics on ion migration, we photo-modulate the charge density occupations within the crystal framework of a candidate SSE,$Li_{0.5}La_{0.5}TiO_3$ (LLTO), and then measure the time-resolved change of its impedance at picosecond timescales. Upon perturbation, we observe enhanced ion migration at ultrafast timescales that are shorter than laser-induced heating. The respective transients match the timescales of optical and acoustic phonon vibrations, suggesting their involvement in ion migration. We further computationally evaluate the effect of a charge transfer from the O $2p$ to Ti $3d$ band on the electronic and physical structure of LLTO. We hypothesize that the charge transfer excitation distorts the TiO_6 polyhedra by altering the local charge density occupancy of the hopping site at the migration pathway saddle point, thereby causing a reduction in the migration barrier for the Li^+ hop, as shown using Nudged Elastic Band (NEB) calculations. We additionally rule out the contribution of photogenerated electron carriers and laser heating through EIS and theoretical modeling of laser-induced heating effects. Overall, our investigation introduces a new spectroscopic tool to probe fundamental ion hopping mechanisms transiently at ultrafast timescales, while other techniques are limited to time-averaged measurements or rely purely on computational methods.

3.1 Introduction

The discovery of numerous superionic conductors like $Li_{10}GeP_2S_{12}$ (LGPS)[1] and related LGPS-type crystal structures,[2] $Li_7P_3S_{11}$,[3] $Li_7La_3Zr_2O_{12}$,[4] $Li_{6+x}P_{1-x}Ge_xS_5I$,[5] and $Li_{6-x}PS_{5-x}Br_{1+x}$[6] have guided general design principles known to promote high ionic conductivity.[7] However, current design principles often rely on a static or quasi-static picture of the ionic conduction process.

Ultrafast spectroscopic tools have the ability to transiently resolve ion-sub-lattice couplings on correspondingly ultrafast timescales (picoseconds) to elucidate the role of lattice dynamics on ion migration. Ultrafast broadband and narrowband pulsed light sources can be used to photo-excite and study how coupling effects from optical phonons,[8–10] acoustic phonons,[10] and electrons,[11] influence ion migration. For example, intensity-modulated photocurrent spectroscopy [12] and similar techniques have been used to study enhanced ion mobility under photo-excitation in some solar-cell materials like $CH_3NH_3PBI_3$,[13–15] $CsPbI_3$,[16] and $SrTiO_3$,[17] where ion migration is enhanced by up to five orders in magnitude due to the decomposition of the parent material to create vacancies or defects.[13] However, other instances of enhanced mobility have also been shown to be possible without material decomposition.[14, 18] More recently, such techniques have also been applied to solid-state ion conductors to study opto-ionic effects.

For instance, Defferriere *et al* studied the role of the grain boundary space charge potential in an oxygen solid-state conductor 3 mol % $Ce_{1-x}Gd_xO_2$, enabling a four-fold increase in grain boundary conduction at 250°C.[19] However, what is still missing from many of these previous studies is the ultrafast transient measurement of parameters directly related to ion migration at the timescales that optical phonons, acoustic phonons, and charge transfer phenomena occur at. Such measurements would experimentally prove the exact dynamics that enable ion migration at the site-to-site and picosecond time resolution, which have traditionally been predicted only through computational methods.[20] Furthermore, the highly tunable nature of light generation at frequencies that can photo-excite electron, ion, and lattice correlations selectively, can enable the large-scale screening of mechanisms that could enhance ionic conductivity by orders of magnitude across multiple family-structure types without relying on initial exploratory synthesis approaches.

In this chapter, we use the ultrafast, time-resolved methodology described in Chapter 2 to study how localized charge densities within the crystal framework couple to and enhance Li^+ migration in a well-characterized solid-state ionic conductor, LLTO,

which has an excitable band gap in the UV range. We employ the ultrafast impedance technique to transiently resolve the contributions from acoustic and optical phonons on picosecond to nanosecond timescales. We measure electron-lattice-ion dynamic coupling effects by perturbing those dynamics with different light excitations. We then measure the transient change in impedance from millisecond to picosecond timescales. For the photoexcitation of the O $2p$ - Ti $3d$ charge transfer transition, we measure decay signatures in the impedance measurements that correspond to the modification of ion hopping on the timescales of optical phonon vibrations, lasting tens of picoseconds. We compare these dynamics with those induced by indirectly exciting the acoustic phonon bath of the sample, leading to laser-induced heating. The signal takes more than a hundred picoseconds to decay, matching the longer baseline perturbation in the charge-transfer photoexcitation. Finally, we examine these photoinduced dynamics on longer timescales of milliseconds to seconds using single frequency impedance transient (SFIT) measurements.

Transiently resolving the changed impedance due to selective photoexcitation allows us to assign the role of high-energy optical phonons and heating in the ion hopping mechanism. NEB calculations[21] also support our experimental observations. When the barrier against Li^+ diffusion through LLTO is calculated via NEB in the excited state after promoting an electron from the highest occupied to the lowest unoccupied band, a reduction in the activation energy by 8 meV compared to the ground state is observed. The saddle point structure in the migration path and activation energy are also likely altered due to the modifications in the occupancy of the valence states from the O atoms upon excitation in the LLTO. We also prove that the measured effect is not attributed to the photogeneration of electronic carriers by using DC polarization methods with blocking electrodes and EIS.

Our results suggest that the decrease in charge density of the O anions, which form the 4-O bottleneck through which Li^+ hops, leads to a decrease in Coulombic interactions. Distorted octahedral modes in oxide perovskites are also theorized to assist the ion hop and are likely at play in the form of phonons during the charge transfer.[22] Our findings give insight into the dynamics of the crystal during an ion hop in LLTO, which can be translated to other Li^+ conductor design principles. Although we specifically investigate a Li^+ solid-state electrolyte, our methodology can extend to other ion-conducting systems with applications ranging from solid oxide fuel cell membranes to bio-inspired ion membranes. The developed technique presents a new method to understand the dynamical aspects of electronic screening

and lattice vibrations in the ion hopping process.

3.2 Theoretical and spectroscopic characterization of LLTO

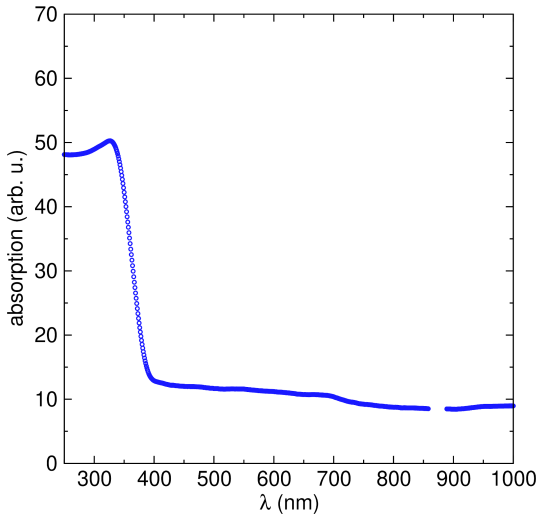

Figure 3.1: UV-VIS spectrum of LLTO. The sudden decrease in absorption at 700 nm is due to the internal switching to another detector. Gap between 860 to 890 nm is also related to the instrument detector.

To determine the laser frequencies relevant for a charge transfer excitation, we first characterize LLTO spectroscopically via UV-Vis to determine the experimental band gap energy as shown in Figure 3.1. To obtain the UV-Vis spectrum, a Shimadzu SolidSpec-3700i UV-VIS-NIR spectrophotometer was employed over a wavelength range of 250 nm – 1000 nm in diffuse reflectance mode. The sudden decrease in absorption between 870 - 880 nm is due to the internal switching from the PMT detector to the InGaAs dectector at 870 nm. A Kubelka-Munk transform was applied to obtain the relative absorption spectrum. The sharp decrease in absorption occurs at approximately 326 nm and reaches the minimum absorption value at 380 nm (3.26 eV) which we assign as the experimental band gap. Based on the absorption spectrum of LLTO, we choose to conduct experiments with pulsed, 350 nm light generated from a 1 kHz, 38 fs, 13 mJ Ti: Sapphire laser and OPA. We also conduct the same experiments with 800 nm light to further understand the wavelength dependency, especially below-band gap energies, in LLTO.

Density of states (DOS) plotted in Figure 3.2 for the fully-ordered structure shows that La and Li ions have a negligible contribution to the valence and conduction band manifold in the energy range of -4.5 to 4.5 eV. The O $2p$ and Ti $3d$ orbitals are hybridized in this energy range, indicating that Ti-O form covalent bonds. Moreover,

the valence band maximum (VBM) and conduction band minimum (CBM) have predominant O-2p and Ti-3d character, respectively, matching previous calculations. [23] We note that the calculated band gap shows the typical DFT underestimation and can be improved by using a more accurate description of the electron-electron interaction, e.g., via hybrid exchange-correlation functionals or many-body perturbation theory, among other methods. For the purpose of this paper, more precise methods are not required, as we also determine the band gap experimentally.

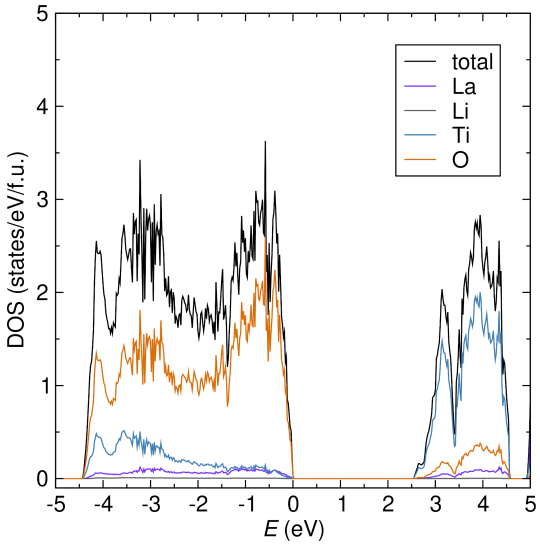

Figure 3.2: Calculated density of states (DOS) for the fully-ordered structure marked by the solid black line, and projected-density of states (PDOS) of La, Li, Ti, and O marked by purple, gray, blue, and orange lines respectively.

To predict how an above band gap excitation can influence the ion migration barrier, an electron is promoted from the valence band to the conduction band to simulate the photoexcitation. NEB calculations are first performed for the fully- and partially-ordered phase to obtain the migration barrier of Li^+ along the a-b plane, starting from the edge of the fully-ordered LLTO structure. For the ground state Li^+ migration in the ordered phase, a barrier of 159 meV is obtained along the NEB path (see Figure 3.3a). The positions of the migrating Li^+ ion and the NEB path in the fully-ordered structure are shown in Figure 3.3b-c. For the partially-ordered phase a barrier of 220 meV is obtained with NEB along the path shown in Figure C.1a and Figure C.1b-c, respectively. Constrained-density functional theory (CDFT) calculations coupled with NEB were performed by promoting an electron from the highest occupied band to the lowest unoccupied band at the $\Gamma-$point in both spin channels, [21, 24] corresponding to a carrier density of 6.9×10^{19} carriers/cm^3. Based on

the experimental excitation parameters used in this study, we approximate carrier densities ranging between 1.9×10^{17} to 5.6×10^{17} carriers/cm^3.[25] A reduction of the barrier of about 8 meV is observed, indicating an enhanced migration. For the partially-ordered phase, a similar reduction of the barrier is calculated.

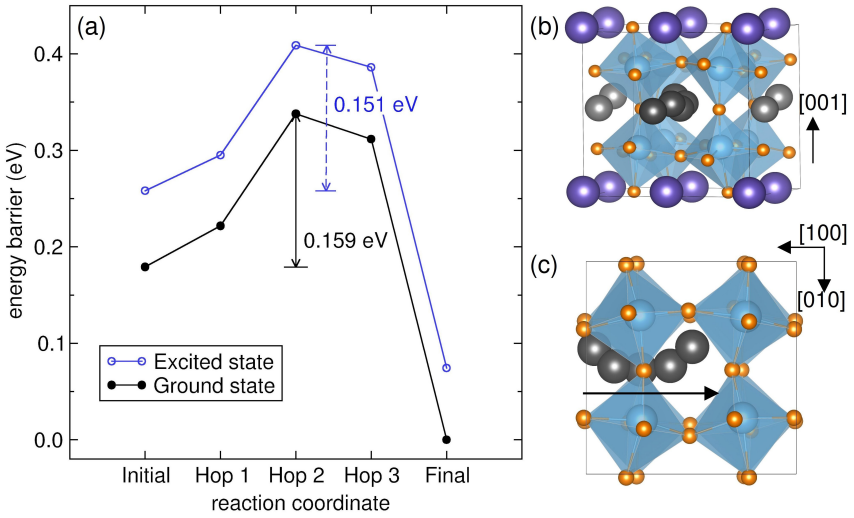

Figure 3.3: Calculated energy barriers of the hopping Li^+ at the ground and excited state for the fully-ordered phase. (a) The ground and excited state migration pathways are shown as the solid black and blue lines respectively. The arrows represent the energy difference between the saddle point and the initial starting energy. (b) side and (c) top view of the complete NEB path, where the migrating Li atoms are marked in dark gray. In the top view, the La and non-migrating Li atoms are not shown for clarity, and the direction of migration is shown by a black arrow.

Analysis of the band structures of the ground state geometries of the fully/partially-ordered phase along the NEB path shows a reduction in the band gap from the starting structure (2.53/2.61 eV) to the saddle point (2.26/2.30 eV), which then increases for the final structure (2.37/2.47 eV) of the NEB path (see Figure C.2/C.3). The band gap narrowing observed at the saddle point seems to correlate with the reduction of the migration barrier, likely due to the charge transfer altering the saddle-point crystal structure which has a non-trivial impact on the migration pathway. The saddle point of the migration pathway can be physically interpreted as the four oxygen (4-O) bottleneck window formed by four corner-sharing TiO_6 octahedra as shown in Figure 3.3b.[26] The distortions in the TiO_6 octahedra in LLTO are predicted to originate from electronic repulsions between the Ti-d and O-p orbitals in the Ti-O bond, as well as tilts and rotations driven by the disordering of the Li and La in the crystal.[23, 27] Therefore, the above band gap photo-excitation likely

alters the degree of distortions associated with the TiO_6 octahedra, thus lowering the migration barrier.

3.3 Preliminary investigation with non-time resolved impedance measurements

After structurally characterizing LLTO (as discussed in detail in Chapter 2.2), the sample was prepared for electrochemical characterization via EIS. The resulting LLTO powder was pressed into a pellet with a diameter of 9 mm and a thickness of 0.8 mm under 2 tons of force (or 308.3 MPa of pressure), yielding a 75-76% pellet density. The pellet was subsequently annealed at 1100°C for 6 hours at a ramp rate of 2°C / min over a bed of its mother powder. A 1.6 mm thick strip of Au was sputtered for 360 seconds at 8 W under 5 Pa onto one side of the pellet with a 1 mm gap in the center using the MSE PRO compact magnetron ion sputtering coater as shown in Figure E.1a. The 350 nm or 800 nm beam would excite the LLTO within the un-sputtered gap to eliminate possible effects on the impedance from illuminating the Au. Since the thickness of the sputtered Au electrodes are not well-defined, the accurate determination of the ionic conductivity is not possible. However, since all pellets are prepared with the same sputtering conditions, sample thickness, and diameter, the relative changes in impedance due to excitation are reproducible and reliable within error over a set of three pellets and three trials per pellet.

EIS measurements of pelletized LLTO were collected first without any optical excitation sources, shown by the lightest purple circles in Figure 3.4a-b to characterize the impedance. The grain boundary feature is fit to an $R_1 + R_{GB}/Q_2$ circuit while the bulk feature is fit to an $R_1 + R_{Bulk}/Q_2$. The R values for each semi-circular feature are assigned to the grain boundary or bulk ion conduction based on the corresponding capacitance values obtained from the circuit fit.

To conduct simultaneous photo-excitation EIS experiments, the 350 nm and 800 nm light sources were generated using a regenerative Ti:Sapphire laser amplifier operating at 1 kHz. The 4.6 W, 800 nm output from the Ti:Sapphire laser was split using a beam splitter. One path was used directly for 800 nm excitation experiments while the other path was sent through an optical parametric amplifier and NIRUVis to generate 350 nm light at a maximum power of 12 mW - 16 mW. The power was adjusted to 2-8 mW using neutral density filters for EIS measurements under illumination. The total power of the 800 nm beam was decreased using neutral density filters to achieve 5-20 mW of average power for measurements under

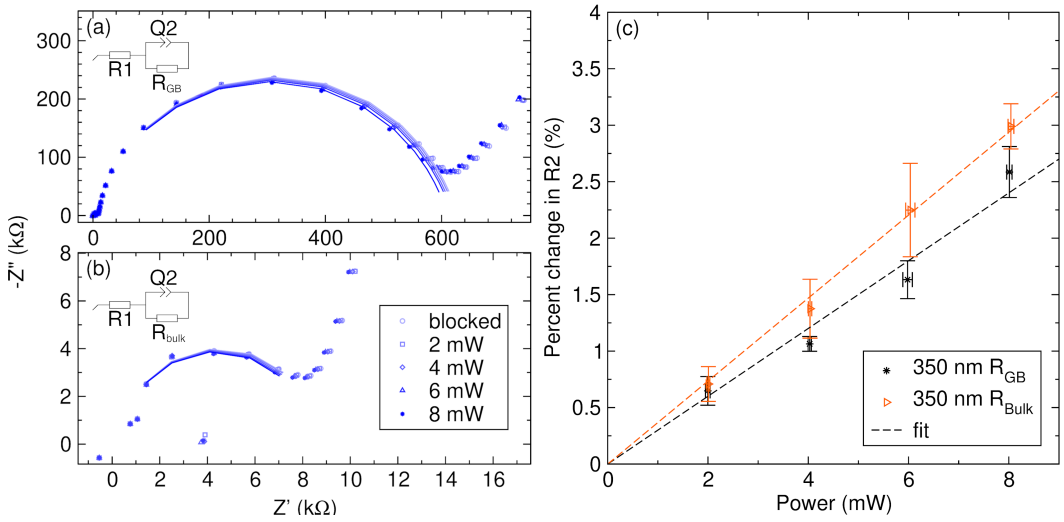

Figure 3.4: Nyquist plots of LLTO showing the decrease in impedance upon 350 nm excitation from 0 to 8 mW of average pulse power and corresponding plot of linear shift in impedance with increasing average power. (a) Grain boundary semi-circle fit to a $R1 + R_{GB}/Q2$ circuit. (b) Bulk impedance semi-circle fit to a $R1 + R_{Bulk}/Q2$ circuit. The symbols represent the raw data and the lines represent the respective equivalent circuit fits. (c) Percent change in R_{GB} and R_{bulk} upon irradiation of a 350 nm excitation source (1 kHz repetition rate, fs pulsed). The R^2 is 0.9924 and 0.9991 for the R_{GB} and R_{bulk} respectively. 1 mW of power causes a 0.30% and 0.37% change in the grain boundary and bulk impedances respectively.

illumination. The beam area of the 350 nm beam and 800 nm beam is $3.76x10^{-4}cm^2$ and $1.06x10^{-3}cm^2$ respectively at their experimental maximum power. The beam size of both excitation sources were determined using a knife-edge technique.

The change in impedance caused by UV-excitation is shown in Figure 3.4a-b, where the lightest purple line represents the dark measurement and varied darker blue lines represent the illuminated measurements from 5 to 20 mW. With increasing average power, the intercept of the semi-circles corresponding to the grain boundary and bulk measurements shift to lower impedances, indicating enhanced ion transport.

The final R_{GB} and R_{Bulk} extracted from the fit is plotted against UV power in Figure 3.4c, demonstrating that the measured change in impedance is linearly proportional to power. The data in Figure 3.4c is reported as a change in impedance rather than ionic conductivity because the sample electrode geometry tests the surface or planar impedance, rather than through the entire sample pellet with a defined thickness (see methods for further discussion). For comparison, the measured

change in impedance with increasing average power is also demonstrated with the 800 nm excitation, predicted to thermally heat the sample, shown in Figure 3.5. When compared to the 350 nm excitation, the 800 nm excitation leads to a 3x lower decrease in the impedance, suggesting that thermally heating the sample leads to a smaller change in enhanced ion migration compared to the collective lattice dynamics triggered by the 350 nm excitation.

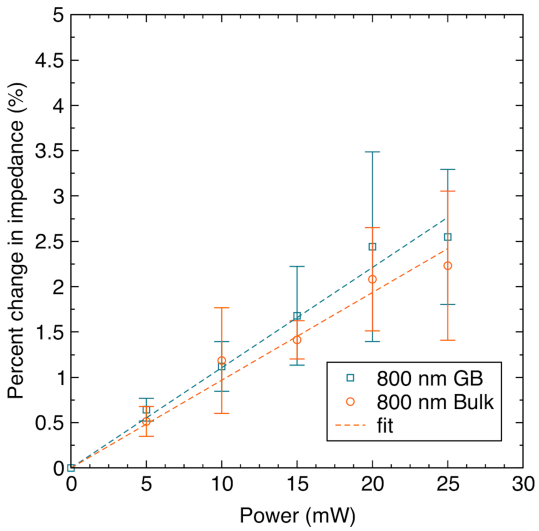

Figure 3.5: The percent change in impedance as a function of power using a 1 kHz pulsed 800 nm laser with a 250 μm beam diameter. 1 mW of power causes a 0.11% change in grain boundary impedance (R^2 = 0.9936) and 0.10% in bulk impedance (R^2 = 0.9918).

To study the reversibility of the enhancement for both the 350 nm and 800 nm case, we conduct SFIT measurements using a sinusoidal signal at a 251 kHz frequency with an amplitude of 100 mV, corresponding to the intercept of the bulk semi-circular feature determined first by EIS (as shown in Figure 3.4c). As shown in Figure 3.6, a single impedance value corresponding to the bulk feature is measured as a function of time with a resolution of 326 ms.

A higher average power is used for the 800 nm excitation source compared to the 350 nm source to match the magnitude of change in the measured Z' and show the clear decrease in impedance as seen in Figure 3.7. At 11 mW, the 800 nm excitation source shows a smaller decrease in Z', rendering the transient analysis more difficult as shown in Appendix H. The difference in required power between photoexcitation wavelengths is due to the differences in penetration depth that are wavelength-dependent, which is discussed later in Chapter 3.

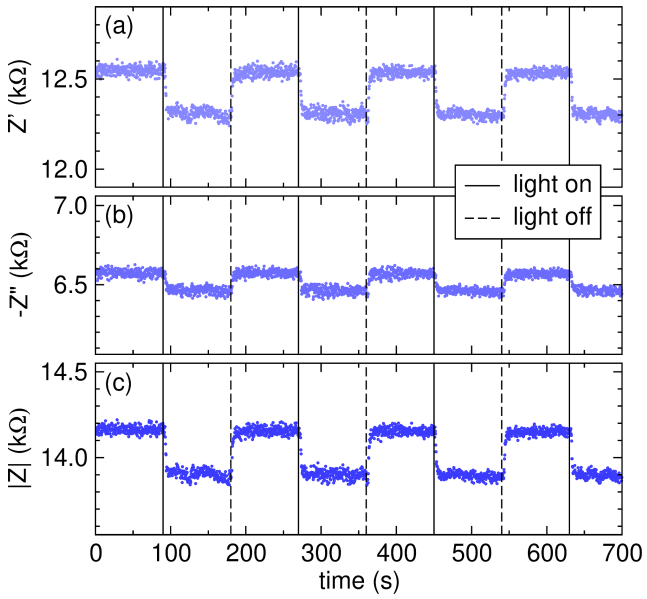

Figure 3.6: SFIT measurements of (a) the real impedance, (b) the imaginary impedance, and (c) the total impedance of LLTO upon 350 nm excitation at 251 kHz and 100 mV sinusoidal frequency amplitude. The on and off lines indicate when the impulse excitation is active or not.

For both the charge-transfer and laser-induced heating excitation, the original Z' measured with the laser reproducibly returns to its initial impedance value after removal of the laser, suggesting that the observed photo-induced effect is reversible. The overall timescales for reaching steady-state impedance during the light off to on transition lasts between 9 to 14 seconds for excitation with the 800 nm source versus 6 to 8 seconds for the 350 nm source. For the opposite transition, the 350 nm impedance transient to steady-state is slower, lasting 6 to 8 seconds versus the 4 to 6 seconds in the 800 nm case. However, this conclusion is ambiguous because of the measurement resolution. More importantly, the 10s of seconds required to reach steady-state between light on and off conditions is present for both excitation wavelengths, suggesting that at long timescales, the decay of acoustic or optical phonons ultimately lead to heat (as discussed in the next section), which promotes ion hopping via increased thermal vibrations.

Although the SFIT measurements shown for LLTO provide interesting preliminary information regarding the hysteresis-like effects triggered by an above-band gap excitation, the exact interpretation of the effect's relation to single ion hops cannot be discerned solely based on the data presented thus far.

The SFIT measures the resulting impedance after a train of multiple femtosecond

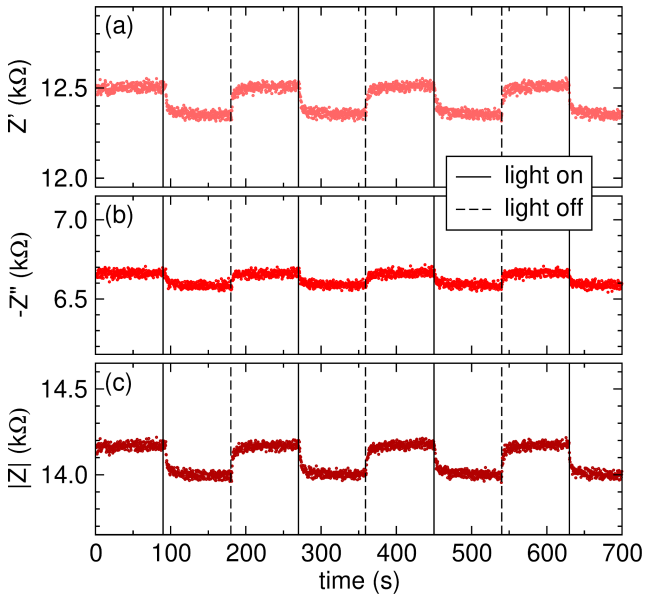

Figure 3.7: SFIT measurements of (a) the real impedance, (b) the imaginary impedance, and (c) the total impedance of LLTO upon 800 nm excitation at 251 kHz and 100 mV sinusoidal frequency amplitude. The on and off lines indicate when the impulse excitation is active or not.

pulses, i.e., an averaged, non-time resolved measurement. Additionally, the slow timescales of the SFIT measurements make this tool unsuitable for determining what mechanisms are at play within the few-seconds transition between the dark and illuminated states of LLTO, especially considering that the faster impulse UV light lasts several femtoseconds. The dynamical processes predicted to be triggered by the 350 nm excitation occurs at much faster timescales (picoseconds), requiring an equally fast probe to elucidate the charge transfer and subsequent phonon-type effects computationally predicted to enhance ion migration.

3.4 Analysis of an ultrafast, time-resolved impedance measurement

Thus, to investigate the transient role of Coulombic interactions and subsequent lattice dynamics on ion migration in LLTO at sub-nanosecond to picosecond timescales, we use an ultrafast impedance probe that we introduced in Chapter 2. Briefly, we utilize high speed electronics to measure the photo-induced change in ionic migration following a femtosecond excitation at different laser frequencies selected to excite the dynamic of interest.

The technique utilizes high-frequency electronics to measure the photo-induced change in ion migration following a femtosecond excitation at laser frequencies se-

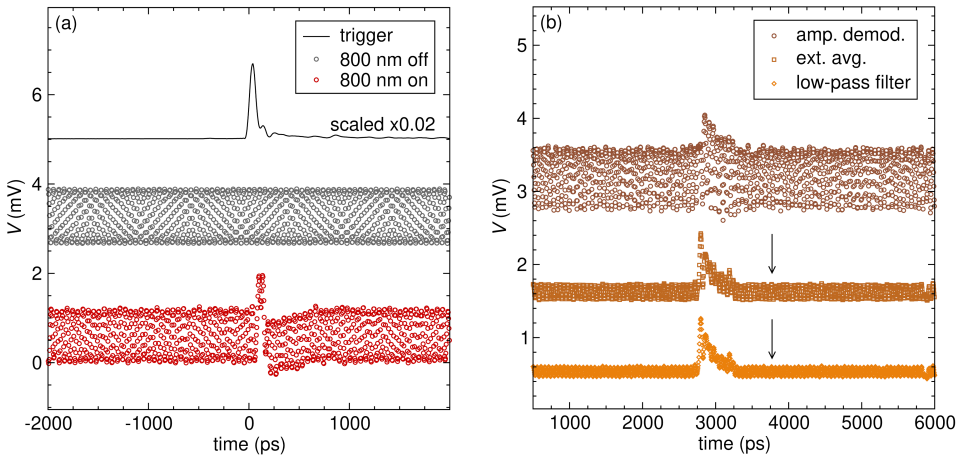

Figure 3.8: Measurement of the ultrafast modulated and processed amplitude demodulated signal of LLTO from 800 nm excitation. (a) The measured modulated signal of the sample upon impulse 800 nm excitation at 5 mW. The black line corresponds to the 800 nm pulse used as the trigger, and the gray and red open circles represent the sample response under light off and light on conditions respectively. (b) The amplitude demodulated signal from (a) (in dark orange open circles), further processed to minimize the sinusoidal background by applying an external average (orange open squares) and a low-pass filter cut off at 17 GHz (light-orange open diamonds).

lected to excite the crystal structure or electronic dynamic of interest. In this chapter, the charge-transfer excitation from the O $2p$ to Ti $3d$ orbitals is photomodulated with pulsed 350 nm light which lies above the measured band gap onset of LLTO (3.26 eV). We use 800 nm light to indirectly heat the acoustic phonon bath as a control experiment through a defect excitation route in the band gap tail. We then resolve the impedance signal using a high frequency signal generator and real-time oscilloscope, which functions similarly to a frequency response analyzer to collect EIS measurements up to gigahertz frequencies. The picosecond-resolution transients of the GHz signal are resolved after photoexcitation.

The advantage of utilizing the signal generator and oscilloscope as separate instruments that couple to each other is the ability to access both high gigahertz frequencies and time-resolved picosecond transients which traditional potentiostats or FRAs like the Solartron1260A cannot achieve.

The ultrafast impedance measurement from data acquisition to post-measurement processing is shown in Figures 3.8 and 3.9. The 800 nm and 350 nm excitation modulates the amplitude of a 19 GHz 1dBm carrier signal reflected off of the sample, shown in Figure 3.8a and 3.9a. The frequency and amplitude of the carrier

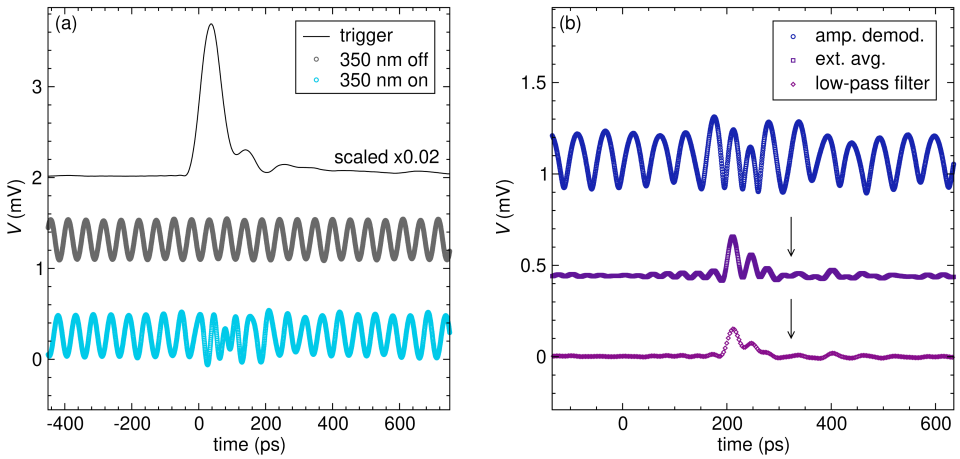

Figure 3.9: Measurement of the ultrafast modulated and processed amplitude demodulated signal of LLTO from 350 nm excitation. (a) The measured modulated signal of the sample upon impulse 350 nm excitation at 5 mW. The black line corresponds to the 800 nm pulse used as the trigger, and the gray and blue open circles represent the sample response under light off and light on conditions respectively. (b) The amplitude demodulated signal from (a) (in blue open circles), further processed to minimize the sinusoidal background by applying an external average (purple open squares) and a low-pass filter cut off at 17 GHz (red-violet open diamonds).

signal were selected to increase the signal-to-noise ratio of the signal.

We apply an amplitude demodulation function on the measured signal to extract the change in impedance. We decrease the background sinusoidal response with further averaging and a 17 GHz low pass filter, as shown in Figure 3.8b and 3.9b. After applying an upper root-mean-square (RMS) envelope for the processed data sets, we can accurately compare the transient impedance response of LLTO upon 800 nm laser-induced heating (Figure 3.10a) and 350 nm charge-transfer excitation (Figure 3.10b).

The decay features of the fully processed demodulation signals are fit to an exponential decay function shown in Equation 3.1:[28, 29]

$$S = Aexp\frac{-t}{\tau} \tag{3.1}$$

Where S represents the measured signal, A represents a scaling factor, t represents time, and τ represents the lifetime associated with the decay. The τ is calculated from the optimized fit as shown by the black line in Figure 3.10 and reported with a 95% confidence interval. From the average of three fits, we determine τ to be

136.3 - 144.9 ps and 27.6-30.7 ps for the laser-induced heating and charge-transfer excitation signals, respectively. After the dominant exponential decay in the charge-transfer signal, the signal persists for 600 ps, consistent with the effects seen in the laser-induced heating data. We note that the instrument response function is bounded on the lower end at 7.8 picoseconds by the oscilloscope's sampling limit. Capacitive effects are likely to be present in the measurement circuit, but no signal distortion was measured up to the oscilloscope's limit of 33 GHz.

The measured signal response from the 800 nm excitation is consistent with laser-induced heating, with the 350 nm response also eventually decaying into heat. The response from the 800 nm photoexcitation follows the known timescales of acoustic phonon excitation and decay, which would match the free carrier or defect heating mechanism present for excitation wavelengths longer than the band gap. The picosecond response triggered by the 350 nm excitation occurs on the same timescales as the decay of optical phonon vibrations following a band gap excitation, many of which are known to couple strongly to the migrating Li^+.[30] In later sections, we also conclude that photogenerated electronic effects are absent in these measurements.

Finally, we conduct a time-resolved synchrotron diffraction measurement to rule out laser-induced phase decomposition or the stabilization of a photo-induced meta-stable structural phase. The measurement is conducted on a single grain of LLTO with 100 ps resolution under 349 nm pulsed excitation. We observe that the expanded lattice constant relaxes post-illumination within 1 millisecond as shown in Figure 3.11 at 302 K. This upper bound is a result of the 1 kHz repetition rate of both the 349 nm pump and X-ray probe used in the study. Since there was no overhead time between each scan, the pre-time-zero data corresponds to an effective time delay of approximately 1 millisecond between the previous pump pulse and current probe pulse. Because the observed lattice constant is equal and stagnant for each scan before time zero, the lattice must relax to equilibrium within the 1 millisecond time window between pulse events. The observed changes are associated with thermally induced lattice expansions, rather than the evolution of a new phase. We also do not measure any octahedral rotations in the transient X-ray diffraction experiments. More details regarding the time-resolved synchrotron measurement methodology can be found in previous work by McClellan and Zong *et al*. [31]

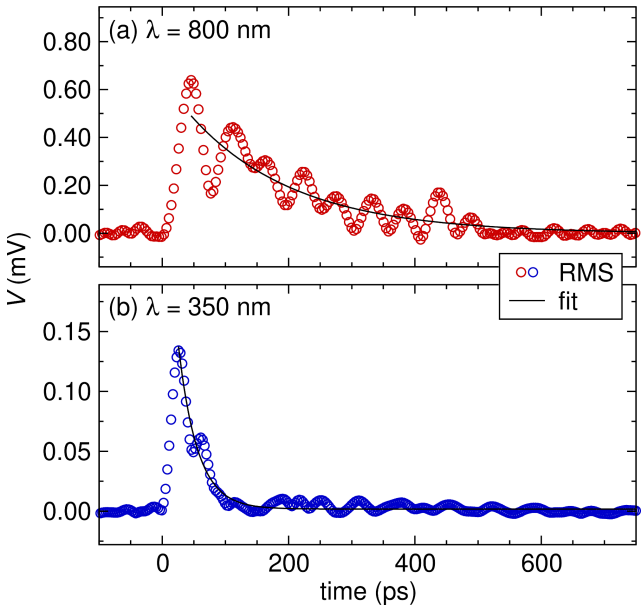

Figure 3.10: Comparison of the ultrafast modulation responses of LLTO from the laser-induced heating or charge-transfer excitation. (a) The red and (b) blue circles represent the Root-Mean-Square (RMS) of the measured signal due to the 5 mW, 800 nm and 350 nm excitation, respectively, after the application of internal and external averaging, amplitude demodulation, and low pass frequency filtering. The black solid lines represent the exponential fit corresponding to the decay of the modulated signal. The input carrier frequency is at 19 GHz with an amplitude of 1 dBm. All excitations are offset to zero to compare the characteristic signal peaks and features.

Discussion

The measured transients and calculated τ suggest that different dynamical processes are at play involving the migrating Li^+ and its interaction with the surrounding crystal. The measured response in Figure 3.10 suggests that the photoexcited electron bath induced by the charge-transfer excitation thermalizes by interacting with optical phonons on a few picoseconds timescale. The laser-induced heating excitation leads to a longer decay, more consistent with the acoustic phonon bath. Acoustic phonons can also participate in electron thermalization but are more commonly observed following the decay of the optical phonon bath like that shown for γ-Li_3PO_4.[10] The charge-transfer excitation decay is nearly five times faster than the decay from the laser-induced heating excitation, possibly due to the modified phonons from the change in O $2p$ charge density occupancy. In the charge-transfer transition decay signal, a smaller background signal from heat also persists on the same timescale as the acoustic phonon bath that followed the excitation of laser-induced heating,

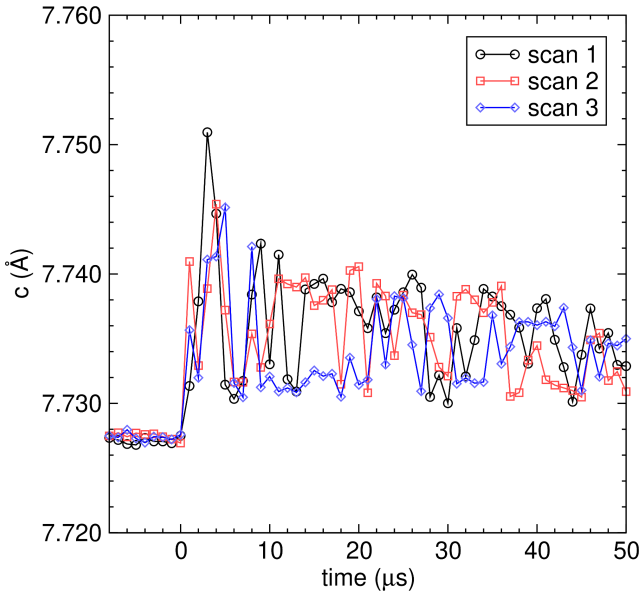

Figure 3.11: Time-resolved synchrotron x-ray diffraction of the c-parameter of a single grain of LLTO, upon excitation of a 349 nm, 67 mJ/cm^2, 1 kHz repetition rate source. The excitation occurs after 0 μs, increasing the lattice parameter initially which then eventually recovers back to the original value over time.

extending out to 600 ps. The matching timescales of both types of signals indicates that laser heating is present in both cases, but at a lower relative amplitude for the charge-transfer case. This charge-transfer, therefore, plays a more significant role in the modulated ionic conductivity than laser heating.

Based on these findings, we propose the following mechanism for photo-enhanced Li^+ hopping: the above band gap, photo-induced charge-transfer excitation modifies the electronic repulsion between the Ti $3d$ and O $2p$ orbitals within the Ti-O bond. The modified repulsion then modulates the optical phonon bath. The changed electronic interaction distorts TiO_6 octahedra, and consequentially, the 4-O bottleneck window at the saddle point of the ion migration pathway of the Li^+. The combined effects of screening and the excited phonons lead to enhanced ion migration.

Consistent with the hypothesis, theoretical partial charge density plots of the VBM show charge localization near the O sites, verifying their dominant contribution during optical excitation. Partial-charge-density plots for the fully-ordered phase in the ground state are presented in Figure 3.12 for the VBM and in Figure C.4 for the CBM at all k-points in the Brillouin zone and at the Γ-point. The O $2p$ orbitals for the VBM and Ti $3d$ for the CBM are consistent with the density of states analysis (see Figure 3.2). The Li sites do not participate in the optical excitation, as shown

by the absence of charge distribution around those sites. O $2p$ states are observed around a majority of the O sites when the full set of k-points in the Brillouin zone are considered. However, at the Γ point where the excitation is initiated in the NEB calculations, the equatorial O atoms contribute significantly in the start and end structure, while predominant contributions from the apical O are observed in the saddle point structure. Notably, the O $2p$ states are only observed in the TiO_6 octahedra to the left of the migrating Li^+.

Figure C.5 shows the relative displacements of the relaxed excited-state geometry with respect to the relaxed ground-state geometry along the NEB path. The start and end structures reveal that the displacements of the equatorial O atoms are along the $a - b$ plane and possible twisting of the TiO_6 octahedra, whereas the saddle point structure shows tilting motion of the TiO_6 octahedra as seen by the displacement of the corner sharing apical O atoms mostly along the $a - b$ plane and the equatorial O atoms along the $c-$axis. We note that these displacements are observed predominantly for the TiO_6 octahedra to the left of the migrating Li^+ and impact the Coulombic interactions in the crystal. The photoinduced charge transfer transition thus changes the screening of the crystal framework on the Li^+ hop, altering the migration barrier. By modifying the charge density occupancy, the structural distortions of the TiO_6 octahedra are initiated, thereby changing both the 4-O bottleneck structure and the behavior of corresponding phonons, consistent with the ultrafast studies that measured a signal decay matching the timescales of optical phonons.

3.5 Explanations for observed photo-enhancement in ion migration at long timescales

For both the 350 nm and 800 nm excitation, the dark impedances during the off period consistently returns to its initial impedance value after removal of the excitation source as seen in Figures 3.6 and 3.7, suggesting that the observed photo-induced effect is reversible. What is certain from the SFIT measurements is that a much slower response on the order of seconds is observed upon continuous irradiation of a femtosecond pulse.

Explanations for long-lasting photo-induced states and dynamics involving electron, ion, and crystal lattice couplings include irreversible phase changes and light-induced material decomposition,[13] reversible phase changes,[14, 32, 33] direct energy transfer to migrating ions,[33, 34] and dipole orientations or lattice distor-

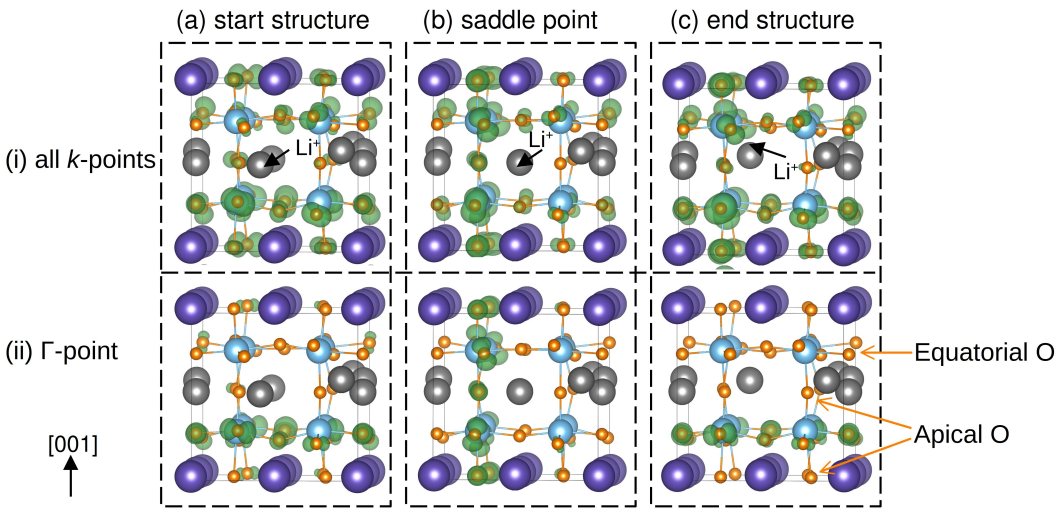

Figure 3.12: Band-decomposed partial charge density plot for the fully-ordered phase at Γ-point: (a) starting structure (b) saddle point and (c) end structure of the NEB path. The top row depicts charge density of the valence band maximum (VBM) and the bottom row is for the conduction band minimum (CBM). Iso-surface (in green) of the plot is set to 0.007 e/Å^3. The migrating Li^+ ion is marked with a black arrow and the NEB path is along the a-b plane towards the centre of the structure. *Figure courtesy of Dr. Vijaya Begum-Hudde.*

tions.[35, 36] In all cases, the dynamics observed are unequivocally too slow to be assigned purely to linear electronic effects,[14, 36, 37] considering that charge injection times can range from nanoseconds to microseconds[32] while the migration of vacancies and defects occur up to microseconds, and in some cases for vacancies up to minute time-scales.[38] In the case of photo-excited LLTO, we investigate the possibility long-lasting relaxations caused by phase changes, significant octahedral re-orientations, or phase segregation.

As shown by the synchrotron diffraction study of LLTO under 350 nm pulsed excitation[31] the results suggest that neither the decomposition nor the formation of new phases occurred. Rather, a lattice expansion of 0.2 Å was measured along the c-axis, likely of the absorbed laser power eventually heating the material. In a previous study, octahedral rotations have been shown to contribute highly to ionic migration in LLTO.[30] Since the octahedra are slightly distorted due to the electronic repulsion of Ti and O orbitals,[23] the potential for dipole re-orientations is possible. Dipole orientations have the potential to screen charges,[14, 35, 39] thereby enhancing ion mobility. However, we do not measure any octahedral rotations in the transient X-ray diffraction experiments.

Second, in addition to possible effects from dipole orientations or lattice distortions, the convoluted effects of direct energy transfer to migrating ions must also be considered. The mechanism of direct energy transfer via light proposed by Shishiyanu *et al* portrays an over-simplified picture of how light energy can be decomposed into a thermal and quantum component as shown in Equation 3.2, where D is the diffusion coefficient, D_0 is the pre-factor term, E_D is the activation energy, k is the Boltzmann constant, and T is the temperature, E_T and E_{hv} are the thermal and quantum parts of energy respectively, and η is the efficiency of light radiation:[34]

$$D(T, hv) = D_0 exp(-[E_D - \frac{\eta(E_{hv} - E_g(T))}{kT}) \tag{3.2}$$

Equation 3.2 is narrow in scope and assumes that all absorbed optical energy goes into the ion hopping, which is not always the case. However, Equation 3.2 still broadly suggests the important effect of thermal and quantum energy transfer to ion migration.

The equation for ionic conductivity σ_{ion} is shown in Equation 3.3 where σ_0 is the Arrhenius pre-factor, T is temperature, E_a is the activation energy, and k_B is the Boltzmann constant:

$$\sigma_{ion} = \frac{\sigma_0}{T} exp(-E_a/k_B T) \tag{3.3}$$

When the pre-factor σ_0 in Equation 3.3 is expanded, we see that σ_{ion} also depends on the entropy of migration ΔS_m and the enthalpy of migration ΔH_m:[40]

$$\sigma_{ion} \propto exp(\Delta S_m/k_B) * exp(\Delta H_m/k_B T) * \frac{1}{T} \tag{3.4}$$

The value of ΔS_m is determined by collective phonon-ion interactions which are predicted to correlate with and enhance ionic conductivity[41]. The value of ΔH_m is experimentally measured as the E_a. If the band gap excitation is truly causing lattice distortions or dipole orientations, the increase in ΔS_m would consequentially increase the ionic conductivity which we confirmed previously by driving phonon modes with THz fields in LLTO.[30] The reorientation of dipoles can be confirmed with X-ray diffraction, as was shown for $MAPbI_3$, where the ratio of 2θ angles corresponding to the change in rotation angle along the c-axis of the octahedra were measured and shown to change upon illumination.[14] However, again, in the case

of our time-resolved synchrotron data, only a thermal expansion is measured. The measured optical phonon vibrations in the ultrafast impedance measurements would not show up in the transient X-ray diffraction timescales.

Finally, the 10's of seconds timescale required to return to the pre-illumination impedance in LLTO is similar to the relaxation timescales measured by Hoke *et al* with $(CH_3NH_3)Pb(Br_xI_{1-x})_3$ upon removal of white light, measured by photoluminescence spectroscopy.[18] In that study, the minute timescale for relaxation was attributed to photo-driven halide segregation into I-rich and Br-rich domains, corroborated by X-ray diffraction. In more extreme cases, even longer relaxation timescales in dark measurements can last up to several hours like that measured by published by Gottesman *et al* for $CH_3NH_3PbBrI_3$ under white light.[14] Considering that the observed relaxation time scales are shorter than minutes time scales and that a major photo-induced structure or phase change was absent according to time-resolved XRD, the slightly faster timescales may indicate a more reversible local change like the slight TiO_6 distortions predicted to occur at the saddle point of the migration pathway. Unfortunately, such small photo-induced distortions are difficult to confirm experimentally which renders this hypothesis inconclusive. A more rigorous molecular dynamic simulation could investigate this phenomena further, though it is beyond the scope of our study.

3.6 Consideration of photo-induced thermal and electronic effects on ion mobility

An important consideration for interpreting photo-induced enhancement in ion migration is the possibility of increased electronic conductivity or predominant thermal heating triggered by photoexcitation. First, we conduct DC polarization experiments with Li^+ blocking and non-blocking electrode geometries to separate the change in electronic conductivity and total conductivity under photoexcitation. Second, we conduct elevated temperature EIS measurements under photoexcitation to factor temperature into the final measured change in impedance values. Finally, we use theory to model contributions from optical heating unaccounted for by our control experiment. These control experiments corroborate our conclusions derived from the ultrafast impedance transients and NEB calculations.

First, we conduct DC polarization experiments using a Li^+-blocking Au electrode to measure electron carrier mobility during photoexcitation. The potential for enhanced electronic conductivity must be considered given that the excitation energy for the

UV light (3.54 eV) exceeds the bandgap energy (3.26 eV), and considering that both the electrons and ions can be mobile charged carriers that contribute to the total measured impedance or conductivity.

To conduct the DC Polarization experiment, a voltage step is applied to the sample which first charges the double layer formed at the electrode-sample interface (non-Faradaic current that exponentially decays with time), and then at longer timescales, the charging of the double layer completes and the steady-state current (Faradaic current) is measured.

The behavior of the current, i, with time, t, when applying a potential step of magnitude E is described by Equation 3.5:[42]

$$i = \frac{E}{R_s} e^{-t/R_s C_d} \tag{3.5}$$

Where R_s is the solution resistance, and C_d is the differential capacitance of the double layer.

The steady-state current measured at long timescales is associated with the electronic conductivity or total conductivity, depending on the type of electrodes used and the mobile species. To discriminate between both carriers during photo-excitation, we conduct DC polarization experiments with a blocking Au electrode to measure the current decay associated with electron conductivity and a non-blocking Li electrode to measure the total conductivity, further described in the methods section and supplementary information. By subtracting the enhancement of the electronic conductivity from that of the total conductivity, we can extract the enhanced Li^+ conductivity.

To measure the resulting steady-state current under photo-excitation with both blocking and non-blocking electrodes, we use the custom optical cell described in more detail in Appendix E.1 and prepared the cell with Au as the ion-blocking electrode. The electronic conductivity is determined by polarizing the cell with a series of applied voltages (200, 300, 400, and 500 mV). For the non-blocking DC polarization experiment, we adopt a similar procedure as Inaguma *et al*[43] to prevent the LLTO from reacting with Li metal. Li foil was used in combination with a 9 mm diameter glass fiber separator sliced in half containing 30μL per side of 1 M LiTFSI salt dissolved in equal volume of ethylene carbonate to dimethyl carbonate to prevent the decomposition of LLTO and measure the total conductivity. To isolate the current enhancement induced by laser illumination in both the ion-blocking

and non-blocking cases, the current is first held steady without illumination for 120 seconds, then for the next 10.5 minutes the laser beam is alternately covered and uncovered every 90 seconds. The difference between these blocked and unblocked states determines the magnitude of current enhancement in both cases of electronic (Au electrode) and total (Li electrode) conductivity.

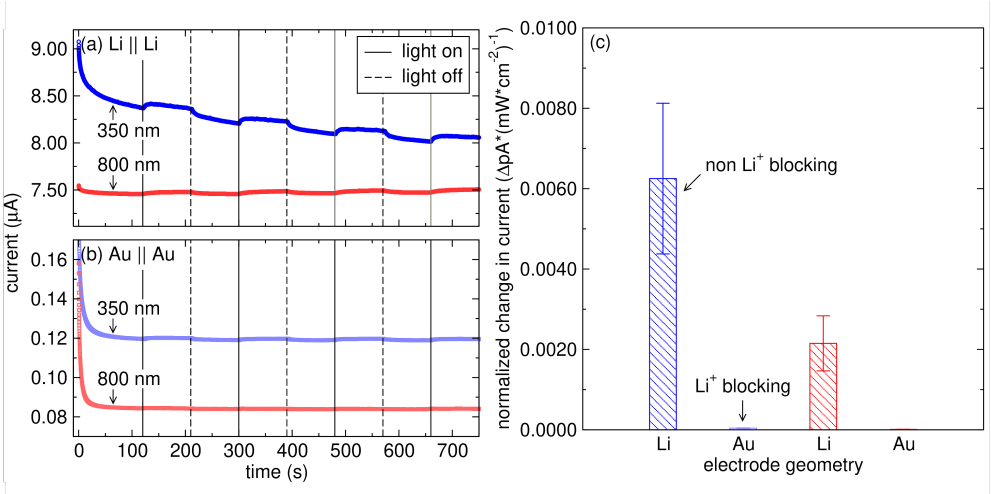

Figure 3.13: Steady-state current responses upon impulse 350 nm and 800 nm light with blocking and non-blocking electrodes. (a) Steady-state current responses after a 200 mV potential step and impulse 13 mW, 350 nm and 20 mW, 800 nm light with blocking (Au) and non-blocking (Li) electrodes. (b) Average change in current normalized by power density (in $\Delta pA/mW * cm^2$) extracted from the DC polarization measurements.

The non-blocking electrode experiment with the 350 nm charge-transfer excitation and the 800 nm laser-induced heating excitation is shown in Figure 3.13a and Appendix F, Figures F.1-F.3. After the non-Faradaic current decay is measured, the Faradaic current associated with both Li^+ and electron mobility is measured. After 90 seconds of illumination, the 350 nm photoexcitation increases the measured current by 70-150 nA while the 800 nm heating excitation increases the current by 20-50 nA. When normalized by the power density, the charge-transfer excitation increases the total current by nearly three-fold as compared to laser-induced heating (5.90×10^{-3} pA/mW*cm^2 and 2.12×10^{-3} pA/mW*cm^2). The ion-blocking electrode experiment is shown in Figure 3.13b and Figures F.2-F.4. After the non-Faradaic current is measured, the Faradaic current associated only with electron mobility can be measured because the Li^+ does not alloy with the Au. The enhancement in current after illumination at 350 nm is 0.6-0.9 nA, which is much smaller than that measured with Li electrodes, seen in Figure 3.13b. Our observa-

tions are consistent with the measured ionic conductivity from the DC polarization measurements being three orders of magnitude larger than the measured electronic conductivity of 8×10^{-10} S/cm, similar to previous reports.[43] Electronic carriers following the photoexcitation are, therefore, unlikely to be responsible for the measured change in impedance in the EIS measurements and the ultrafast impedance experiments.

Second, we explore the contribution of laser heating to the observed enhancement of ion migration. The impedance of the sample is measured upon irradiation at temperatures between 298 K - 343 K using a custom heating cell that is described in greater detail in the Appendix E.2. The outlined experiment enables the normalization of changed impedance by changed sample temperature.

The EIS spectra is first taken at room temperature using the 1260A solartron impedance analyzer with an applied sinusoidal voltage amplitude of 100 mV and a frequency range of 32 MHz to 1 Hz. 5 points are measured per decade and each point is averaged over 5 measurements. To achieve higher resolution EIS spectra at variable temperatures from 298 K to 343 K for the bulk feature, the frequency range is adjusted to a range of 32 MHz to 20 kHz and 10 points are measured per decade. The power used for the elevated temperature EIS experiments were 7-12 mW and 20-25 mW for the 350 nm and 800 nm excitation sources respectively.

The change in impedance at elevated temperatures is shown in Figure 3.14, where the Nyquist plots of LLTO are measured before (light off) and after (light on) optical excitation.

The optical excitation causes an additional enhancement on top of that caused by increased temperature. The difference between the light on and light off experiments is plotted as ΔR and $\Delta Z'$ for the bulk ion migration region in Figure 3.15a and Figure 3.15b, respectively. Beyond 313 K, the impedance measurements become noisier because the higher temperatures cause the Nyquist plots to shift toward lower impedance and beyond the impedance analyzer's measurement capabilities. The resolvable semi-circular features are then buried in the noisy, high frequency region, causing poorer fits as evidenced in Figure 3.14b. The red dashed lines corresponding to the light on fit also overlap poorly with the data shown as open triangles, contributing to the uncertainty in the fit. To account for the larger standard deviation, the change in the Z' intercept of the bulk semi-circular feature at 804 kHz between 298 K – 323 K and 2.02 MHz between 333 – 343 K is also plotted for comparison in Figure 3.15, yielding smaller standard deviations.

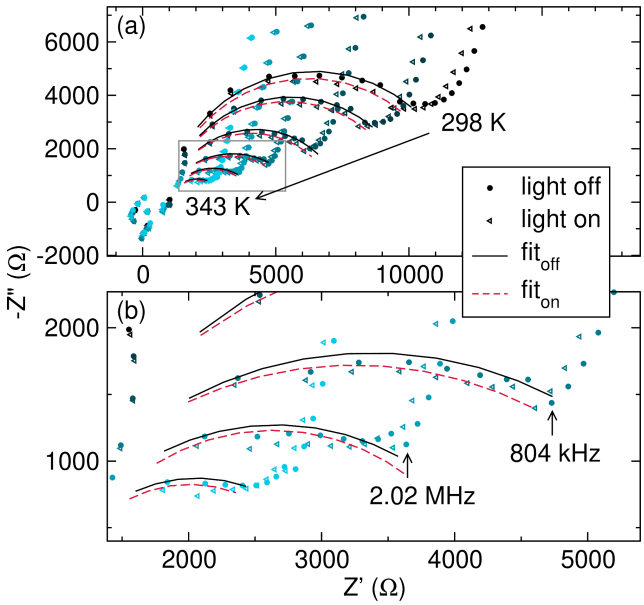

Figure 3.14: Nyquist plots of LLTO upon impulse 350 nm light at 7 mW (1kHz repetition rate, femtosecond pulse) from 298 K to 343 K (increasing first by 5 K, then increments of 10 K after 303 K). (a) Bulk impedance semi-circle fitted to a $R1 + R_{Bulk}/Q2$ circuit. The filled circles and open triangles correspond to the light off measurements and light on measurements respectively. The solid black lines and dashed red lines correspond to the fits for the light off and light off measurements respectively. The gray box corresponds to the region plotted in (b) between 323 K to 343 K. (b) expanded view of the 323 K to 343 K region, highlighting the poorer fits at high temperatures compared to the 298 K – 313 K measurements.

By calculating the slope of the measured data, the absolute change in impedance caused by the optical excitation can be normalized by temperature and power density, allowing for direct comparison between excitation wavelengths. The slope of the linear fit of the 350 nm charge-transfer excitation is -6×10^{-4} and -4×10^{-4} Ω*(mW*cm^{-2})$^{-1}$K^{-1} for ΔR_{on-off} and $\Delta Z'_{on-off}$, respectively, and is double that of the 800 nm laser-induced heating excitation (-3×10^{-4} and -2×10^{-4} Ω*(mW*cm^{-2})$^{-1}$K^{-1} for ΔR_{on-off} and $\Delta Z'_{on-off}$, respectively. The larger slope of the charge-transfer excitation suggests that the associated phonon bath is more sensitive to changes in ionic conduction which increases linearly with temperature.[26]

The temperature-dependent photoexcited impedance measurements presented in Figure 3.15 reveal that the magnitude of photoenhancement is dependent upon the availability of phonon baths that can be populated to enhance ion migration. Relevant phonon baths can be excited either via heating or laser-induced photomodulation. Because the 350 nm charge-transfer excitation induces a greater enhancement in

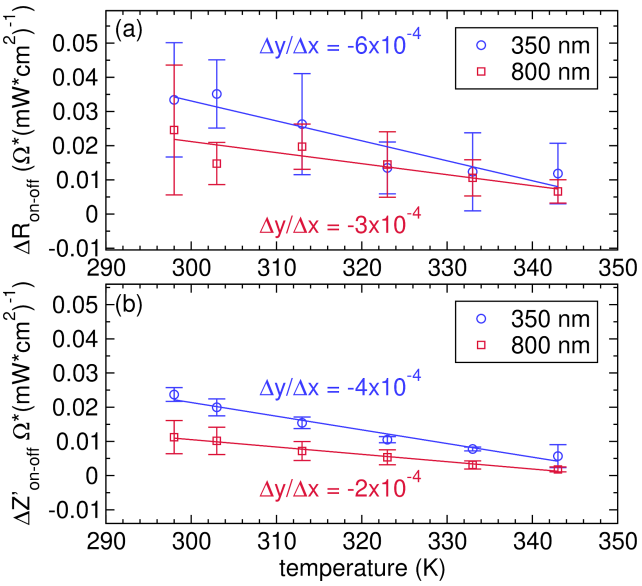

Figure 3.15: The difference in the fitted R_{bulk} (a) and non-fitted intercept of the bulk semi-circle Z' (b) between the light on and light off measurements between 298 K and 343 K from a 350 nm or 800 nm excitation. The blue circle and diamonds correspond to the 350 nm femtosecond pulsed light and the red square and triangles correspond to the 800 nm femtosecond pulsed light. The final difference is normalized by the respective power density. R2 = 0.88 and 0.78 for ΔR_{bulk} and $R2 = 0.97$ and 0.99 for $\Delta Z'$ for 350 nm and 800 nm respectively.

ionic conduction near 298 K in Figure 3.15, we believe that the phonon modes excited via this excitation couple more closely with ion transport than laser-induced heating brought about by the 800 nm pulse. More precisely, the optical phonons indicated by the ultrafast impedance measurement and excited by a charge-transfer excitation, modulate the ion hop pathway more than simply increasing thermal vibrations in the sample. If processes unrelated to ion conduction are excited, the shift in impedance would be constant and independent of temperature, yielding a slope close to zero. Additionally, if the change in impedance is purely from a heating mechanism for both the 350 nm and 800 nm excitation, the slopes would be equal when normalized by absorbed laser power density, which does not appear to be the case according to Figure 3.15. While Figure 3.15 indicates that the charge-transfer and heating excitation interact differently with the sample, it does not inform us about the role of thermal heating caused by a laser excitation.

We decouple the impacts of laser heating from the bulk heating that was discussed in Figure 3.14 and 3.15 using a finite-difference time-domain (FDTD) heat conduction model, discussed in more detail in our submitted work.[44]

The FDTD model, adapted from previous literature [45, 46] and further detailed in the methods section, describes the sample's change in temperature as a function of time due to laser excitation. The model is designed to account for differences in penetration depth, reflection, and additional laser power parameters when comparing the 350 nm and 800 nm photoexcitation data. In brief, the simulation generates heating maps that show the spatial temperature variation along the cross section of the sample upon impulse light. As seen in Figures D.3 and D.4, an 800 nm, 20 mW beam is predicted to increase the sample temperature by 0.5 K, while an IR thermal gun measures an increase in sample temperature between 0.4 and 0.8 K (Figure D.5). For the 350 nm, 16 mW beam, the simulation predicts an increase of 1.7 K while the measured sample temperature increase varies between 1 to 3 K (Figure D.5).

Using the results of the model, we estimate an upper bound for the sample's increase in temperature on millisecond to second timescales. As seen in Figures D.1 and D.2, the sample reaches the maximum peak temperature along the surface. The volume probed in the EIS experiment geometry is difficult to define, but is expected to exceed the depth heated by the laser. Future work can more rigorously explore the thermal effects from the laser with improved computational models, while also utilizing electrode geometries that increase the overlap of the laser pulse with the electrochemical probe. However, these advancements are beyond the scope of this work. As such, we use the modeled surface temperature as an upper bound to estimate the laser-induced heating effects on ionic migration in LLTO.

Our results reveal that the predicted $\Delta K/mW$ of 350 nm laser power is 0.11, while the 800 nm light induces a 0.03 $\Delta K/mW$ increase. The difference in surface heating arises due to the two orders of magnitude shorter LLTO absorption depth at 350 nm compared to 800 nm light. We then determine the decrease in resistance attributable to thermal effects by multiplying the computed heating factor by a measured heat-induced enhancement factor of 2.16 $\%\Delta R/K$ from Figure 3.15. The final calculated thermal enhancement values, in units of $\%\Delta R/mW$, are shown in Table 3.1 and compared to the measured enhancements determined in Figure 3.4c for the 350 nm light and Figure 3.5 for the 800 nm light.

From Table 3.1, the total measured enhancement is larger than the contribution from thermal effects for both wavelengths. With 800 nm light, there is an excess photo-modulation effect (0.04 $\%\Delta R/mW$), found by subtracting the thermal from the measured enhancement. The comparable values suggest that the excited acous-

Wavelength (nm)	Thermal Enhancement (%ΔR/mW)	Measured Enhancement (%ΔR/mW)
350	0.24	0.37 ±0.01
800	0.06	0.10 ±0.01

Table 3.1: Deconvolution of laser-induced thermal enhancements on ion migration.

tic phonons, which ultimately dissipate as heat, are responsible for the measured decrease in impedance. However, we make the distinction that non-resonant laser heating is not equivalent to raising the bulk sample temperature due to the presence of additional photo-modulation effects which appear to be activated, as shown by the difference in thermal and total enhancement values. In comparison, the measured change in impedance using 350 nm light is larger than the thermally-induced effects (Table 3.1) by 0.13 $\%\Delta R/mW$. Considering that the thermally-induced impact comprises 65 % of the total measured enhancement ratio, the sample is likely heated via similar mechanisms as the 800 nm light on longer timescales. The remaining 35 % of the total measured effects are likely attributed to above bandgap excitation effects, or the population of optical phonon baths that are inaccessible using 800 nm light. Populating the optical phonon bath leads to a greater enhancement, and is demonstrated both computationally with NEB and experimentally with the ultrafast impedance transients. Altogether, the control experiments and ultrafast impedance transients strongly indicate that the measured phenomena reflect a photo-induced change in ion migration rather than thermal or electronic effects alone.

In conclusion, we conduct time-resolved impedance measurements to investigate how an above and below band gap photoexcitation enhances ion migration with picosecond resolution. We measure the role of screening and optical phonons using a charge-transfer transition. The role of 4-O phonon modes and apical oxygen charge density occupancies is explored. Our computational results support a charge transfer mechanism from the O $2p$ to Ti $3d$ band which leads to slight distortions in the TiO_6 octahedra that form the migration bottleneck and changes in the occupied charge density surrounding the hopping Li^+. The interplay of optical phonon modes with these dynamics leads to a reduced migration barrier and reduced impedance at ultrafast and slow timescales, as shown by NEB, EIS, and SFIT measurements. We rule out the contribution of photo-generated electronic carriers by performing DC polarization experiments with ion-blocking and non-blocking electrodes. We also explore contributions from thermal heating by conducting EIS measurements

at elevated temperatures under simultaneous photoexcitation and simulating optical heating effects via FDTD methods.

Overall, our investigation serves as an instrumental study in developing new spectroscopic tools to probe fundamental ion hopping mechanisms transiently at ultrafast timescales. We demonstrate the coupled role of optical and acoustic phonons with the migrating ion, which can be selectively excited experimentally. Our work expands upon the dynamical mechanisms of solid-state ionic conduction and motivates future work on conductive meta-stable states, memory effects, and more. Although our study only investigates one type of solid-state ion conductor, our methodology has wider applications for other types of ion and mixed solid-state conductors.

The work presented in this chapter was possible through financial support from the National Science Foundation, Air Force Office of Science & Research, and David & Lucile Packard Foundation. This work was supported by the U.S. Army DEVCOM ARL Army Research Office (ARO) Energy Sciences Competency, Advanced Energy Materials Program award #W911NF-23-1-0001. The equipment used in this work was funded by the Air Force Office of Scientific Research (AFOSR), DURIP grant number FA9550-23-1-0197. Financial support for creating the heating cell is from grant #CS-CSA-2022-068 from the Research Corporation for Science Advancement.

The views and conclusions contained in this document are those of the authors and should not be interpreted as representing the official policies, either expressed or implied, of the U.S. Army or the U.S. Government.

References

[1] Noriaki Kamaya et al. “A lithium superionic conductor”. In: *Nature Materials* 10.9 (Sept. 2011), pp. 682–686. ISSN: 1476-1122, 1476-4660. DOI: 10.1038/nmat3066. URL: http://www.nature.com/articles/nmat3066 (visited on 06/05/2020).

[2] Yuki Kato et al. “High-power all-solid-state batteries using sulfide superionic conductors”. In: *Nature Energy* 1.4 (Mar. 21, 2016). Number: 4 Publisher: Nature Publishing Group, pp. 1–7. ISSN: 2058-7546. DOI: 10.1038/nenergy.2016.30. URL: https://www.nature.com/articles/nenergy201630 (visited on 03/11/2023).

[3] Yoshikatsu Seino et al. “A sulphide lithium super ion conductor is superior to liquid ion conductors for use in rechargeable batteries”. In: *Energy & Environmental Science* 7.2 (Jan. 23, 2014). Publisher: The Royal Society of Chemistry, pp. 627–631. ISSN: 1754-5706. DOI: 10.1039/C3EE41655K.

URL: https://pubs.rsc.org/en/content/articlelanding/2014/ee/c3ee41655k (visited on 03/11/2023).

[4] Junji Awaka et al. "Synthesis and structure analysis of tetragonal $Li_7La_3Zr_2O_{12}$ with the garnet-related type structure". In: *Journal of Solid State Chemistry* 182.8 (Aug. 1, 2009), pp. 2046–2052. ISSN: 0022-4596. DOI: 10.1016/j.jssc.2009.05.020. URL: http://www.sciencedirect.com/science/article/pii/S002245960900228X (visited on 02/21/2020).

[5] Marvin A. Kraft et al. "Inducing high ionic conductivity in the lithium superionic argyrodites $Li_{6+x}P_{1-x}Ge_xS_5I$ for all-solid-state batteries". In: *Journal of the American Chemical Society* 140.47 (Nov. 28, 2018). Publisher: American Chemical Society, pp. 16330–16339. ISSN: 0002-7863. DOI: 10.1021/jacs.8b10282. URL: https://doi.org/10.1021/jacs.8b10282 (visited on 10/12/2022).

[6] Pengbo Wang et al. "Fast ion conduction and its origin in $Li_{6-x}PS_{5-x}Br_{1+x}$". In: *Chemistry of Materials* 32.9 (May 12, 2020). Publisher: American Chemical Society, pp. 3833–3840. ISSN: 0897-4756. DOI: 10.1021/acs.chemmater.9b05331. URL: https://doi.org/10.1021/acs.chemmater.9b05331 (visited on 03/11/2023).

[7] KyuJung Jun et al. "Diffusion mechanisms of fast lithium-ion conductors". In: *Nature Reviews Materials* (Sept. 12, 2024). Publisher: Nature Publishing Group, pp. 1–19. ISSN: 2058-8437. DOI: 10.1038/s41578-024-00715-9. URL: https://www.nature.com/articles/s41578-024-00715-9 (visited on 11/01/2024).

[8] Michael Först, Roman Mankowsky, and Andrea Cavalleri. "Mode-selective control of the crystal lattice". In: *Accounts of Chemical Research* 48.2 (Feb. 17, 2015). Publisher: American Chemical Society, pp. 380–387. ISSN: 0001-4842. DOI: 10.1021/ar500391x. URL: https://doi.org/10.1021/ar500391x (visited on 05/09/2023).

[9] Carlo Vicario et al. "Narrow-band and tunable intense terahertz pulses for mode-selective coherent phonon excitation". In: *Applied Physics Letters* 117.10 (Sept. 8, 2020). Publisher: American Institute of Physics, p. 101101. ISSN: 0003-6951. DOI: 10.1063/5.0015612. URL: https://aip.scitation.org/doi/10.1063/5.0015612 (visited on 09/22/2022).

[10] Qiwei Hu et al. "Anharmonic lattice dynamics dominated ion diffusion in γ-Li_3PO_4". In: *Journal of Solid State Chemistry* 333 (May 1, 2024), p. 124636. ISSN: 0022-4596. DOI: 10.1016/j.jssc.2024.124636. URL: https://www.sciencedirect.com/science/article/pii/S0022459624000902 (visited on 06/13/2024).

[11] Margherita Maiuri, Marco Garavelli, and Giulio Cerullo. "Ultrafast spectroscopy: State of the art and open challenges". In: *Journal of the American Chemical Society* 142.1 (Jan. 8, 2020). Publisher: American Chemical So-

ciety, pp. 3–15. ISSN: 0002-7863. DOI: 10.1021/jacs.9b10533. URL: https://doi.org/10.1021/jacs.9b10533 (visited on 05/05/2023).

[12] Sandheep Ravishankar et al. "Intensity-Modulated Photocurrent Spectroscopy and Its Application to Perovskite Solar Cells". In: *The Journal of Physical Chemistry C* 123.41 (Oct. 17, 2019). Publisher: American Chemical Society, pp. 24995–25014. ISSN: 1932-7447. DOI: 10.1021/acs.jpcc.9b07434. URL: https://doi.org/10.1021/acs.jpcc.9b07434 (visited on 08/08/2024).

[13] Yi-Cheng Zhao et al. "Quantification of light-enhanced ionic transport in lead iodide perovskite thin films and its solar cell applications". In: *Light: Science & Applications* 6.5 (May 2017). Publisher: Nature Publishing Group, e16243–e16243. ISSN: 2047-7538. DOI: 10.1038/lsa.2016.243. URL: https://www.nature.com/articles/lsa2016243 (visited on 07/16/2024).

[14] Ronen Gottesman et al. "Photoinduced reversible structural transformations in free-Standing $CH_3NH_3PbI_3$ perovskite films". In: *The Journal of Physical Chemistry Letters* 6.12 (June 18, 2015). Publisher: American Chemical Society, pp. 2332–2338. DOI: 10.1021/acs.jpclett.5b00994. URL: https://doi.org/10.1021/acs.jpclett.5b00994 (visited on 07/23/2024).

[15] Taeyong Kim et al. "Mapping the pathways of photo-induced ion migration in organic-inorganic hybrid halide perovskites". In: *Nature Communications* 14.1 (Apr. 3, 2023). Number: 1 Publisher: Nature Publishing Group, p. 1846. ISSN: 2041-1723. DOI: 10.1038/s41467-023-37486-w. URL: https://www.nature.com/articles/s41467-023-37486-w (visited on 06/07/2023).

[16] Jincheng Huang et al. "Introducing ion migration and light-induced secondary ion redistribution for phase-stable and high-efficiency inorganic perovskite solar cells". In: *ACS Applied Materials & Interfaces* 12.36 (Sept. 9, 2020). Publisher: American Chemical Society, pp. 40364–40371. ISSN: 1944-8244. DOI: 10.1021/acsami.0c12068. URL: https://doi.org/10.1021/acsami.0c12068 (visited on 08/13/2024).

[17] Alexander Viernstein et al. "Mechanism of photo-ionic stoichiometry changes in $SrTiO_3$". In: *Solid State Ionics* 383 (Oct. 1, 2022), p. 115992. ISSN: 0167-2738. DOI: 10.1016/j.ssi.2022.115992. URL: https://www.sciencedirect.com/science/article/pii/S0167273822001412 (visited on 07/16/2024).

[18] Eric T. Hoke et al. "Reversible photo-induced trap formation in mixed-halide hybrid perovskites for photovoltaics". In: *Chemical Science* 6.1 (Dec. 1, 2014). Publisher: The Royal Society of Chemistry, pp. 613–617. ISSN: 2041-6539. DOI: 10.1039/C4SC03141E. URL: https://pubs.rsc.org/en/content/articlelanding/2015/sc/c4sc03141e (visited on 08/14/2024).

[19] Thomas Defferriere et al. “Photo-enhanced ionic conductivity across grain boundaries in polycrystalline ceramics”. In: *Nature Materials* 21.4 (Apr. 2022). Number: 4 Publisher: Nature Publishing Group, pp. 438–444. ISSN: 1476-4660. DOI: 10.1038/s41563-021-01181-2. URL: https://www.nature.com/articles/s41563-021-01181-2 (visited on 05/09/2023).

[20] Zhizhen Zhang and Linda F. Nazar. “Exploiting the paddle-wheel mechanism for the design of fast ion conductors”. In: *Nature Reviews Materials* 7.5 (May 2022). Number: 5 Publisher: Nature Publishing Group, pp. 389–405. ISSN: 2058-8437. DOI: 10.1038/s41578-021-00401-0. URL: https://www.nature.com/articles/s41578-021-00401-0.

[21] Graeme Henkelman, Blas P. Uberuaga, and Hannes Jónsson. “A climbing image nudged elastic band method for finding saddle points and minimum energy paths”. In: *The Journal of Chemical Physics* 113.22 (Dec. 2000), pp. 9901–9904. ISSN: 0021-9606. DOI: 10.1063/1.1329672. URL: https://doi.org/10.1063/1.1329672.

[22] Xinyu Li and Nicole A. Benedek. “Enhancement of ionic transport in complex oxides through soft lattice modes and epitaxial strain”. In: *Chemistry of Materials* 27.7 (Apr. 14, 2015), pp. 2647–2652. ISSN: 0897-4756, 1520-5002. DOI: 10.1021/acs.chemmater.5b00445. URL: https://pubs.acs.org/doi/10.1021/acs.chemmater.5b00445 (visited on 10/24/2022).

[23] Abdelhak Chouiekh et al. “Experimental and DFT analysis of structural, optical, and electrical properties of $Li_{3x}La_{2/3-x}TiO_3$ (3x = 0.1, 0.3 and 0.5) solid electrolyte”. In: *Ceramics International* 49.15 (Aug. 1, 2023), pp. 25920–25934. ISSN: 0272-8842. DOI: 10.1016/j.ceramint.2023.05.141. URL: https://www.sciencedirect.com/science/article/pii/S0272884223013998 (visited on 07/03/2024).

[24] Adam Gali et al. “Theory of Spin-Conserving Excitation of the $N–V^-$ Center in Diamond”. In: *Phys. Rev. Lett.* 103 (18 Oct. 2009), p. 186404. DOI: 10.1103/PhysRevLett.103.186404. URL: https://link.aps.org/doi/10.1103/PhysRevLett.103.186404.

[25] Scott K. Cushing et al. “Hot phonon and carrier relaxation in Si(100) determined by transient extreme ultraviolet spectroscopy”. In: *Stuctural Dynamics* 5.5 (Sept. 1, 2018), p. 054302. DOI: 10.1063/1.5038015. URL: https://pubs.aip.org/sdy/article/5/5/054302/366054/Hot-phonon-and-carrier-relaxation-in-Si-100 (visited on 04/03/2025).

[26] Sonia Stramare, Venkataraman Thangadurai, and Werner. Weppner. “Lithium lanthanum titanates: A review”. In: *Chemistry of Materials* 15.21 (Oct. 2003), pp. 3974–3990. ISSN: 0897-4756, 1520-5002. DOI: 10.1021/cm0300516. URL: https://pubs.acs.org/doi/10.1021/cm0300516 (visited on 06/06/2021).

[27] Kim Junghwa et al. “Revealing the Interplay of Local Environments and Ionic Transport in Perovskite Solid Electrolytes”. In: *ACS Nano* 18.45 (Nov. 7, 2024), pp. 31234–31243. DOI: 10.1021/acsnano.4c09552. URL: https://pubs.acs.org/doi/10.1021/acsnano.4c09552 (visited on 10/24/2023).

[28] Scot T. Martin et al. “Time-resolved microwave conductivity. Part 1.—TiO2 photoreactivity and size quantization”. In: *Journal of the Chemical Society, Faraday Transactions* 90.21 (Jan. 1, 1994). Publisher: The Royal Society of Chemistry, pp. 3315–3322. ISSN: 1364-5455. DOI: 10.1039/FT9949003315. URL: https://pubs.rsc.org/en/content/articlelanding/1994/ft/ft9949003315 (visited on 02/20/2025).

[29] Christian Kupfer et al. “Unravelling material properties of halide perovskites by combined microwave photoconductivity and time-resolved photoluminescence spectroscopy”. In: *Journal of Materials Chemistry C* 12.1 (Dec. 21, 2023). Publisher: The Royal Society of Chemistry, pp. 95–102. ISSN: 2050-7534. DOI: 10.1039/D3TC03867J. URL: https://pubs.rsc.org/en/content/articlelanding/2024/tc/d3tc03867j (visited on 02/20/2025).

[30] Kim H. Pham et al. “Correlated Terahertz phonon-ion interactions dominate ion conduction in solid electrolyte $Li_{0.5}La_{0.5}TiO_3$”. In: arXiv:2305.01632 (Mar. 6, 2024). DOI: 10.48550/arXiv.2305.01632. arXiv: 2305.01632[cond-mat,physics:physics]. URL: http://arxiv.org/abs/2305.01632 (visited on 03/09/2024).

[31] Jackson McClellan et al. “Hidden correlations in stochastic photoinduced dynamics of a solid-state electrolyte”. In: arXiv:2406.06832 (June 10, 2024). DOI: 10.48550/arXiv.2406.06832. arXiv: 2406.06832[cond-mat,physics:physics]. URL: http://arxiv.org/abs/2406.06832 (visited on 08/16/2024).

[32] Angelo D. Marshall et al. “Probing the origin of light-enhanced ion diffusion in halide perovskites”. In: *ACS Applied Materials & Interfaces* 13.28 (July 21, 2021). Publisher: American Chemical Society, pp. 33609–33617. ISSN: 1944-8244. DOI: 10.1021/acsami.1c05268. URL: https://doi.org/10.1021/acsami.1c05268 (visited on 07/08/2024).

[33] Joshua C. Shank, M. Brooks Tellekamp, and W. Alan Doolittle. “Evidence of ion intercalation mediated band structure modification and opto-ionic coupling in lithium niobite”. In: *Journal of Applied Physics* 117.3 (Jan. 16, 2015), p. 035704. ISSN: 0021-8979. DOI: 10.1063/1.4906125. URL: https://doi.org/10.1063/1.4906125 (visited on 07/16/2024).

[34] Sergiu Shishiyanu et al. “The mechanism of enhanced diffusion of phosphorus in silicon during rapid photothermal processing of solar cells”. In: *IEEE Transactions on Electron Devices* 58.3 (Mar. 2011). Conference Name: IEEE Transactions on Electron Devices, pp. 776–781. ISSN: 1557-9646. DOI: 10.1109/TED.2010.2096511. URL: https://ieeexplore.ieee.org/document/5676195/?arnumber=5676195 (visited on 08/14/2024).

[35] Xiaojing Wu et al. “Composition-dependent light-induced dipole moment change in organometal halide perovskites”. In: *The Journal of Physical Chemistry C* 119.2 (Jan. 15, 2015). Publisher: American Chemical Society, pp. 1253–1259. ISSN: 1932-7447. DOI: 10.1021/jp511314a. URL: https://doi.org/10.1021/jp511314a (visited on 07/23/2024).

[36] Emilio J. Juarez-Perez et al. “Photoinduced giant dielectric constant in lead halide perovskite solar cells”. In: *The Journal of Physical Chemistry Letters* 5.13 (July 3, 2014). Publisher: American Chemical Society, pp. 2390–2394. DOI: 10.1021/jz5011169. URL: https://doi.org/10.1021/jz5011169 (visited on 08/14/2024).

[37] Dane W. deQuilettes et al. “Photo-induced halide redistribution in organic–ino rganic perovskite films”. In: *Nature Communications* 7.1 (May 24, 2016). Publisher: Nature Publishing Group, p. 11683. ISSN: 2041-1723. DOI: 10.1038/ncomms11683. URL: https://www.nature.com/articles/ncomms11683 (visited on 08/14/2024).

[38] Jon M. Azpiroz et al. “Defect migration in methylammonium lead iodide and its role in perovskite solar cell operation”. In: *Energy & Environmental Science* 8.7 (July 3, 2015). Publisher: The Royal Society of Chemistry, pp. 2118–2127. ISSN: 1754-5706. DOI: 10.1039/C5EE01265A. URL: https://pubs.rsc.org/en/content/articlelanding/2015/ee/c5ee01265a (visited on 08/14/2024).

[39] Kenshi Harada et al. “Light-dependent ionic-electronic conduction in an amorphous octahedral molybdenum cluster thin film”. In: *NPG Asia Materials* 14.1 (Mar. 11, 2022). Publisher: Nature Publishing Group, pp. 1–9. ISSN: 1884-4057. DOI: 10.1038/s41427-022-00366-8. URL: https://www.nature.com/articles/s41427-022-00366-8 (visited on 08/16/2024).

[40] Sokseiha Muy et al. “Phonon–ion interactions: Designing ion mobility based on lattice dynamics”. In: *Advanced Energy Materials* 11.15 (2021), p. 2002787. ISSN: 1614-6840. DOI: 10.1002/aenm.202002787. URL: https://onlinelibrary.wiley.com/doi/abs/10.1002/aenm.202002787 (visited on 10/10/2022).

[41] George H. Vineyard. “Frequency factors and isotope effects in solid state rate processes”. In: *Journal of Physics and Chemistry of Solids* 3.1 (Jan. 1, 1957), pp. 121–127. ISSN: 0022-3697. DOI: 10.1016/0022-3697(57)90059-8. URL: https://www.sciencedirect.com/science/article/pii/0022369757900598 (visited on 11/17/2022).

[42] Allen J. Bard and Larry R. Faulkner. *Electrochemical Methods: Fundamentals and Applications*. 2nd. Hoboken, NJ: Wiley, 2000.

[43] Yoshiyuki Inaguma et al. “High ionic conductivity in lithium lanthanum titanate”. In: *Solid State Communications* 86.10 (June 1, 1993), pp. 689–693. ISSN: 0038-1098. DOI: 10.1016/0038-1098(93)90841-A. URL: https://

www.sciencedirect.com/science/article/pii/003810989390841A (visited on 07/01/2024).

[44] Kim H. Pham et al. *The dynamical role of optical phonons and sub-lattice screening in a solid-state ion conductor*. Apr. 11, 2025. DOI: 10.48550/arXiv.2504.07249. arXiv: 2504.07249[cond-mat]. URL: http://arxiv.org/abs/2504.07249 (visited on 05/03/2025).

[45] Lauren L. Taylor, Jun Qiao, and Jie Qiao. "Optimization of femtosecond laser processing of silicon via numerical modeling". In: *Optical Materials Express* 6.9 (Sept. 1, 2016). Publisher: Optica Publishing Group, pp. 2745–2758. ISSN: 2159-3930. DOI: 10.1364/OME.6.002745. URL: https://opg.optica.org/ome/abstract.cfm?uri=ome-6-9-2745 (visited on 02/20/2025).

[46] Lauren L. Taylor, Ryan E. Scott, and Jie Qiao. "Integrating two-temperature and classical heat accumulation models to predict femtosecond laser processing of silicon". In: *Optical Materials Express* 8.3 (Mar. 1, 2018). Publisher: Optica Publishing Group, pp. 648–658. ISSN: 2159-3930. DOI: 10.1364/OME.8.000648. URL: https://opg.optica.org/ome/abstract.cfm?uri=ome-8-3-648 (visited on 02/20/2025).

Chapter 4

NON TIME-RESOLVED, CORRELATED PHONON-ION MODE DRIVING WITH TERAHERTZ (THZ) FREQUENCIES

ABSTRACT

Partially adapted from: Kim H. Pham; Kiarash Gordiz; Natan A. Spear; Amy K. Lin; Jax Dallas; Jonathan M. Michelsen; Hanzhe Liu; Danielle Vivona; Yang Shao-Horn; Asegun Henry; Kimberly A. See; Scott K. Cushing. Correlated Terahertz phonon-ion interactions dominate ion conduction in solid electrolyte $Li_{0.5}La_{0.5}TiO_3$. *arXiv:2305.01632. Submitted.*

Ionic conduction in solids that exceeds 0.01 S/cm is predicted to involve collective phonon-ion interactions in the crystal lattice. Here, we use theory and experiment to measure the contribution of possible collective phonon-ion modes to Li^+ migration in LLTO. *Ab initio* calculations predict that the targeted excitation of individual TiO_6 rocking modes can lead to a three order of magnitude increase in the Li^+ jump rate as compared to the excitation of single vibrational modes in the lattice associated with heating. Experimentally, coherently driving the TiO_6 rocking via terahertz illumination leads to a ten-fold decrease in the normalized impedance compared to the excitation of acoustic and optical phonons that are associated with heating. These findings provide new insights into phonon-coupled ion migration mechanisms and material design rules for ion conductors and opto-ionic materials.

4.1 Introduction

To experimentally quantify the role of distinct phonon-ion couplings on ionic conduction, select frequencies of light can be used to drive relevant modes and its degree of enhancement on ionic conductivity can be measured. The THz region, in particular, can selectively target polyanion modes theorized to mediate ion transport.[1–5] Specifically, modes that involve PS_4^{3-},[6, 7] SiS_4^{4-},[6] PO_4^{3-},[5] YBr_6^{3-},[8] and $ErCl_6^{3-}$[8] polyanion vibrations all fall within the low THz frequencies[1, 5, 8, 9]—equivalent to picosecond hopping timescales.[10] The same modes are theorized to be responsible for coupled hopping in LISICON-like conductors ($Li_{10}SiP_2S_{12}$,[11] LGPS,[1, 12] Li_3PO_4,[5, 13] LPS, [1, 6]) Li-argyrodites (Li_6PS_5Cl, Li_6PS_5Br),[9, 14] and superionic Li-halides(Li_3YBr_6, Li_3ErCl_6[1, 8]). Similarly, octahedral rotations are also reported to promote fast ionic transport in several perovskite-related phases,[15–17] making phonon-driven ionics widely applicable for understanding phonon-ion coupling in many known superionic conductors.

While driving acoustic and optical modes to change electronic and magnetic properties is common in condensed matter physics,[18–20] very few studies directly drive phonon-ion couplings to promote ion transport.[2, 3] In one report, Poletayev *et al* employed a THz pump to induce a Na^+, K^+, and Ag^+ ion hop in $\beta - Al_2O_3$ and then measured the change in birefringence using an 800 nm probe. The THz Kerr Effect measured the anisotropy caused by an ion hop, reporting a 20x increase in hop anisotropy compared to thermal conditions.[3] In addition, Gordiz et al. used Nudged- Elastic Band (NEB) calculations and Molecular Dynamic (MD) simulations to predict that over 87% of the lattice energy during the ion hop in Li_3PO_4 came from less than 10% of the modes in the system.[5] By computationally exciting highly contributing modes while fixing the sample temperature, they showed enhancement of the ionic conductivity by orders of magnitude without increasing the bulk temperature.

To further explore the role of phonons on ion migration in LLTO, we use ab initio calculations, MD simulations, and experiments that combine laser driving and EIS to determine the role of rocking TiO_6 modes on Li^+ hopping. The bottleneck of Li^+ migration in LLTO comprises four oxygen atoms formed by four corner sharing TiO_6 octahedra[16, 17] that are reported to "rock" in place at low THz frequencies and its distortions could lead to enhanced ion migration.

These "rocking modes" are depicted in 1.2. To determine the contribution of

the rocking TiO_6 modes on Li^+ migration, we first excite those modes with THz irradiation from 0.7 to 4.5 THz, or 67 - 428 μm (general schematic shown in 1.2. We compare the driving of targeted phonon modes predicted to enhance Li^+ conduction to laser-induced heating, which is performed via the indirect excitation of acoustic phonon modes with NIR light (800 nm or 0.8 μm). Acoustic phonons can mediate ion conduction via increased random thermal vibrations.[21] Lastly, we excite relevant optical phonon modes within the MIR light range. The La-O mode (11.6 μm) is predicted to weaken if Li^+ interactions with the TiO_6 octahedra are strong,[17] so we test whether driving the La-O vibrations with MIR light (9.4 - 14.16 μm) can weaken Li^+-TiO_6-coupling and modulate Li^+ transport. Finally, we use EIS to probe the subsequent change in impedance due to NIR–THz excitation, correlating with changes in the ion transport behavior. We quantify the role of the differing phonon couplings that mediate ionic conduction by measuring shifts in impedance at each excitation wavelength and normalizing the measured enhancement by the power density of the impulse laser beam. We separately quantify the impacts of laser-induced heating on the sample, finding that long-lasting thermalization effects do not account for the differences in the measured enhancement, indicating that photoinduced lattice dynamics play an outsized role in promoting ion migration.

In agreement with the *ab initio* calculations, our measurements confirm that selectively exciting the THz rocking modes leads to an order of magnitude decrease in the bulk resistance, or R_{bulk}, as compared to exciting acoustic or optical modes, likely due to coupling between the TiO_6 and hopping Li^+. Reminiscent of other metastable phases induced by light in inorganic-organic hybrid perovskites,[22–25] the enhancement that we measured is persistent and reversible, even though the recorded changes are averaged over the 250 Hz repetition rate for the THz source and 1 kHz for the generated NIR-MIR light. Our results intriguingly suggest that laser driving select phonon modes can facilitate fast ion transport in a solid and can inform new design principles to achieve ionic conductivities greater than 1 mS/cm. Our results also motivate future work in picosecond temporal impedance measurements to further explore the dynamics of ion hopping and metastability, as suggested by the seconds-to-minutes long steady states which are induced by a femtosecond pulsed laser.

4.2 *Ab Initio* calculations of modal contributions to ion hopping in LLTO

In collaboration with Dr. Kiarash Gordiz, the modal contributions of the phonon modes in LLTO on the hopping Li^+ were calculated. The contributions of vibrational

modes to the energy needed by Li^+ to reach its transition state (herein referred to as ion hopping) in LLTO were calculated via *ab initio* based on the magnitude of the projection of the atomic displacement field obtained for the transition state on the eigenvectors of vibration for each specific phonon.

To identify the contribution of different phonons to the Li^+ hop in the lattice, we combine methodologies from lattice dynamics and NEB calculations as outlined from literature.[5] The NEB calculations were used to identify the minimum energy pathway for the Li^+ hop. The displacement field obtained from the transition state (saddle point) was then projected onto the eigenvectors of vibration belonging to the structure at the beginning of the hop. The magnitude of the projection shows the degree to which each normal mode contributes to that displacement field, which can be quantified using the following expression:[26, 27]

$$Q_n = \sum_{i=1}^{N} \sqrt{m_i} e^*_{i,n} u_i \tag{4.1}$$

where u_i is the displacement of atom i from its equilibrium position in the configuration at the hopping origin; $e_{i,n}$ is the eigenvector for mode n, assigning the direction and displacement magnitude of atom i obtained from the lattice dynamics calculation[26, 28, 29] for the structure at the hopping origin; * denotes the complex conjugate operator; and m_i is the mass of atom i. Q_n is the modal displacement coordinate, the square of which is proportional to the mode potential energy E_n according to the following equation:

$$E_n = \frac{1}{2}\omega_n^2 Q_n^2 \tag{4.2}$$

The total energy of the system E is equal to the summation over all modal energy values $E = \sum_n E_n$; Here, E_n is the contribution by mode n to the potential energy of the displaced lattice during the ion migration, which can be interpreted as the contribution by mode n to the ion hop along its migration pathway. ω_n is the frequency of vibration of mode n.

E_n can be divided by E to calculate the normalized contribution of that phonon to the Li^+ hop in that specific ion hop event.

Moreover, by normalizing E_n through division by the total number of ion hopping events considered in the study, the resultant normalized E_n can be regarded as the

normalized contribution of mode n to the Li^+ hopping events in the LLTO compound under investigation.

The structure parameters for the calculations were obtained from quantitative Rietveld refinements of experimental synchrotron diffraction data Figure 2.5. To efficiently sample different possible Li^+ ion hops and relevant contributing vibrational modes, 22 unique Li^+ ion hops based on two different hopping mechanisms (single and concerted) across three degrees of La | Li disorder in the LLTO lattice were chosen and analyzed as shown in Figure 4.1.

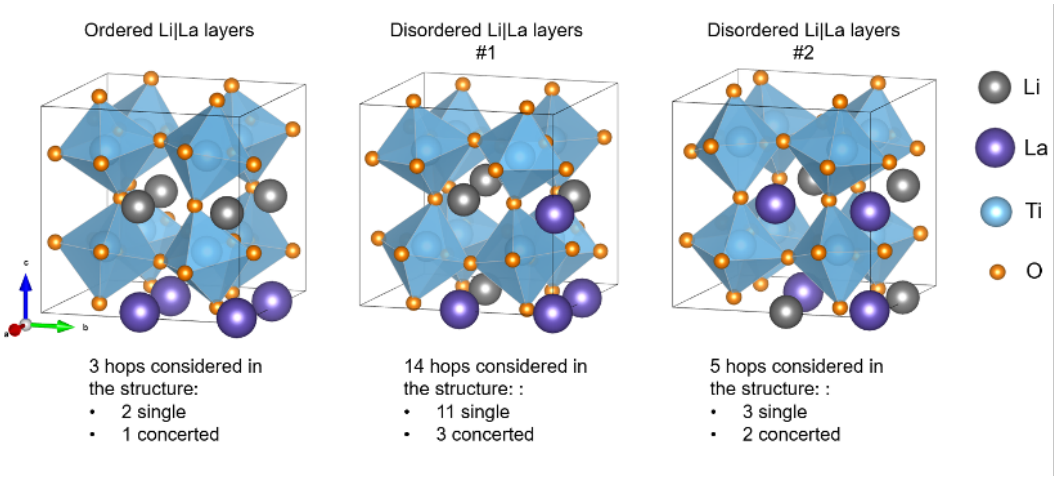

Figure 4.1: Schematics of three different Li|La orderings with respect to the c-axis in the LLTO lattice included in the calculations. The chosen number of Li^+ ion hops with different hopping mechanisms are also included in the bottom of the schematics. *Figure courtesy of Dr. Kiarash Gordiz.*

Depending on which La and Li partial occupancy sites are selected for atom placement in the simulation, locally different structures of LLTO can be formed. Experimental[30] and computational[31–33] studies have shown that the various structures of LLTO can be classified into three categories based on the degree of La|Li disorder in the lattice (Li | La orderings): (i) fully ordered structure, (ii) partially ordered structure, and (iii) fully disordered structure. However, due to the limited size of the supercell used in our simulations (40 atoms), it is difficult to distinguish between the partially ordered and fully disordered structures. Therefore, to maximize our sampling of Li^+ hops in the LLTO lattice within the constraints of the chosen supercell size, three different La|Li orderings are included in the analysis of Li^+ ion hops, as illustrated in Figure 4.1. These chosen structures include one structure with ordered Li|La layers, as well as two structures with disordered Li|La layers

Figure 4.2a shows the resulting normalized cumulative contribution of the different phonon modes to the Li^+ hopping process, here defined as the energy needed for a Li^+ to reach its transition state.

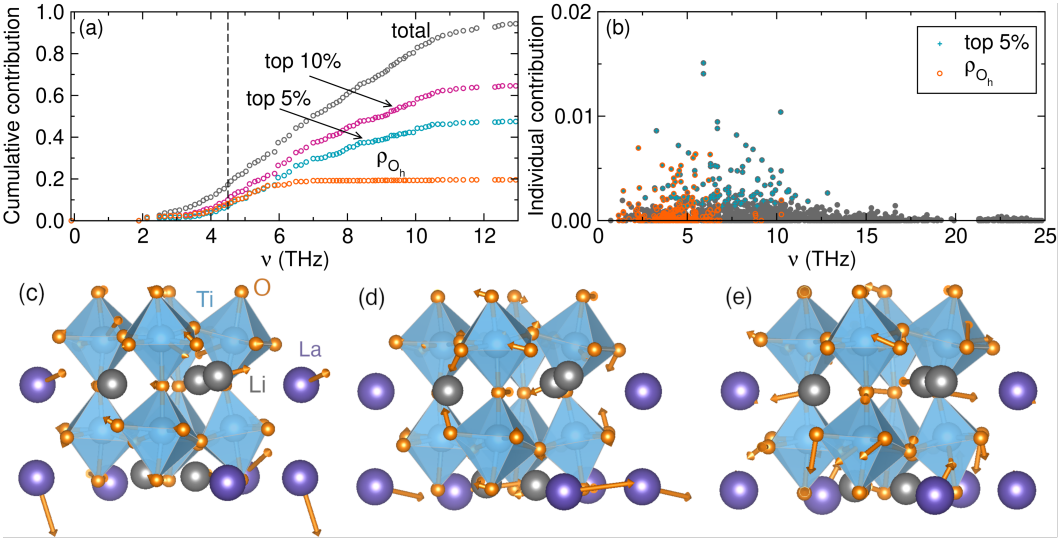

Figure 4.2: Calculated phonon contributions to Li^+ hopping and representative LLTO phonon modes.(a) The cumulative contributions of phonon modes to the normalized energy required for ion hopping, where ρ_{O_h} represents octahedral rocking modes. The black dashed line marks the experimental limit for THz generation (4.5 THz). The cumulative effects of the highest 5% and 10% contributing modes, as well as the octahedral rocking modes are specifically shown.(b) The individualized contributions of phonon modes to the normalized energy required for ion hopping. The data is normalized over all 22 Li^+ hop investigations). (c-e) the eigenvectors of three vibrational modes showing how the lattice displacements project along with the Li^+ hop, under a (c) thermal mode (2.66 THz), (d) the highest contributing non-rocking mode (4.29 THz), and (e) the highest contributing rocking mode (3.46 THz).

Figure 4.2a shows the normalized cumulative contribution of different phonon modes to the Li^+ hopping process, here defined as the energy needed for a Li^+ to reach its transition state. Figure 4.2b shows the individual breakdown of the total phonon mode contributions that sum to 4.2. These modes are further separated based on their projection on different atomic species as shown in Figure 4.3. Rocking modes are distinguished in Figures 4.2a-b.

Experimentally, the phonon modes were only excited up to the instrument limit of 4.5 THz. Thus, we narrow much of our further discussion of the ab initio calculations and MD simulations to the experimental limit of THz generation. The

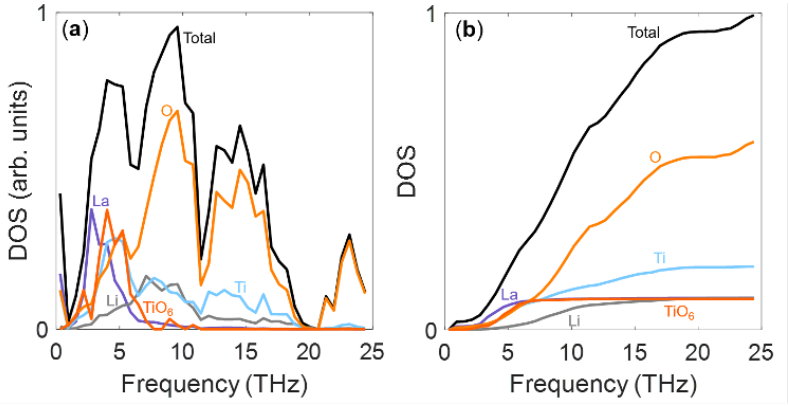

Figure 4.3: Total and partial phonon density of states in (a) non-accumulation and (b) accumulation format for different atomic species and rocking modes (TiO_6 units). Accumulation format helps to reveal useful information. For instance, it shows that 10 % of the total modes are of TiO_6 rocking nature, and in the <6 THz region, 36% of the modes are of TiO_6 rocking nature. *Figure courtesy of Dr. Kiarash Gordiz.*

phonon modes below 4.5 THz (marked by the dashed line) contribute to 17.5% of all sampled hops, as shown in Figure 4.2a, corroborating that low frequency phonon modes strongly influence ion transport as studied in other theoretical reports.[1, 34] Moreover, over 40% of the energy required to induce Li^+ hopping can be accounted for by considering modes up to 6 THz, the occupied population of phonons at room temperature.

To assess if an increase in the hopping rate of Li^+ in LLTO lattice can occur by exciting the identified contributing phonons to the ion hop, three hops were chosen from the 22 investigated hops in this study. The highly contributing phonons are then excited in their respective structures. The following three tests were performed: (i) exciting the top contributing (non-rocking) mode overall, (ii) exciting the top contributing rocking mode, and (iii) exciting a random mode.

Because ion diffusivity increases with temperature, the bulk lattice temperature was fixed to a constant at a low temperature (T = 400 K) so that any change in the diffusivity could be attributed only to the excitation of the targeted modes and not to the bulk temperature. To do so, the total kinetic energy of the system was held constant via a velocity-rescaling scheme, in which, the addition of energy to the intended modes was complimented by a uniform reduction in the kinetic energy of all other modes in the system. To change the temperature of mode n to a desired temperature T_d, the atomic velocities are modified in the system according to the

Hop #	Mode type	Frequency (THz)	400 K (natural MD simulation	700 K (natural MD simulation	400 K (with mode excited to 700 K)
1	Highest non-ρ_{O_h} contributing mode	4.29	0.0011	1.45	1.27
1	Highest ρ_{O_h} contributing mode	3.46	0.0011	1.45	1.39
1	Random mode	2.66	0.0011	1.45	0.0027
2	Highest non-ρ_{O_h} contributing mode	4.50	0.0024	2.07	3.61
2	Highest ρ_{O_h} contributing mode	1.84	0.0024	2.07	3.23
2	Random mode	3.47	0.0024	2.07	0.0004
3	Highest non-ρ_{O_h} contributing mode	5.10	0.0017	1.44	2.09
3	Highest ρ_{O_h} contributing mode	1.94	0.0017	1.44	1.94
3	Random mode	4.43	0.0017	1.44	0.0011

Table 4.1: Enhancement in the ion hopping rate by targeted excitation of the highest contributing non-ρ_{O_h}, highest contributing ρ_{O_h}, and one random mode, that have frequencies in the experimentally accessible frequency range, during MD simulations. The targeted excitation of phonons during MD simulation and the method is applied to three hops among the hops investigated in this study. The visualization of these hops is provided in Appendix J. The numbers included in the table are ion hopping rates (#jumps/ps) besides the numbers listed under the frequency column.

following formula:

$$v_i = v_i + \frac{1}{\sqrt{m_i}}[\sqrt{2k_B T_d} - \dot{Q}_n(t)]e_{i,n} \tag{4.3}$$

where v_i is the velocity of atom i, and $\dot{Q}_n$ is the modal velocity coordinate of mode n defined by:[27]

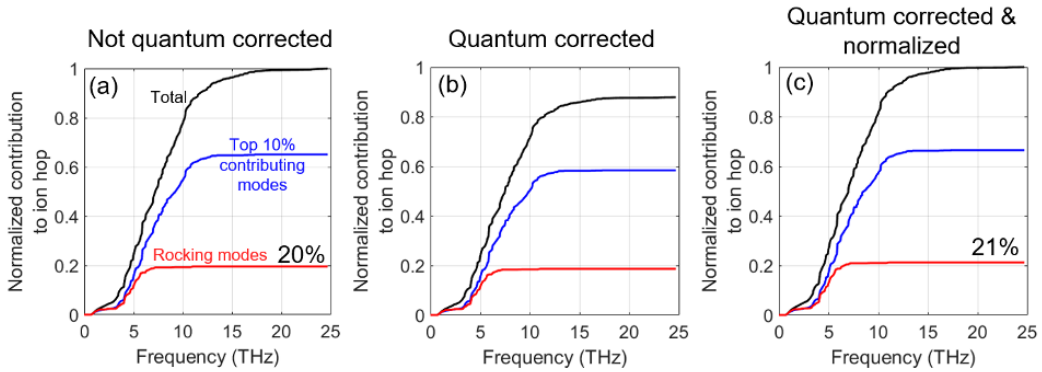

Figure 4.4: Effect of quantum correction on the calculated modal contributions to Li^+ hop in the LLTO lattice. (a) The accumulative modal contributions (a) before, and (b) after quantum correction. (c) Shows the accumulative modal contributions after quantum correction, when the calculated modal contributions are normalized. It can be seen that, since most of the TiO_6 rocking modes have low frequencies (<6 THz), correcting their contribution based on Bose Einstein distribution only slightly increases their overall percentage of contribution to Li^+ in the LLTO lattice (from 20% to 21%). *Figure courtesy of Dr. Kiarash Gordiz.*

$$\dot{Q}_n = \sum_{i=1}^{N} \sqrt{m_i} * e^*_{i,n} v_i \tag{4.4}$$

The chosen method for modal excitation should not change the reported observations in this study because modal excitation (increasing the energy of a mode) can be achieved either by increasing the potential (position perturbation) or the kinetic (velocity perturbation) energy of the mode; the choice of which should not matter. The results for the excitations are shown in Table 4.1. By targeted excitation of the detected contributing phonons in the LLTO structure (including the contributing rocking modes), the hopping rate of the Li^+ increases to the same order magnitude of increasing the hopping rate by increasing the temperature, but this time, by keeping the lattice at the base (T = 400 K) temperature.

The modes in 4.1 for hopping pathway 1 (Figure J.1) are visualized in Figures 4.2c-e, where the random mode at 2.66 THz does not align with the hopping path of the Li^+ (Figure 4.2c), while the highly contributing modes, both rocking and non-rocking, appear to have lattice vibrations aligned with the Li^+ jump path (Figures 4.2d-e). The overall hopping path in which correlated phonon-ion coupling occurs demonstrate

a predicted three order of magnitude enhancement associated with exciting phonon modes that align with the Li^+ hop.

Due to the low frequency nature of modes below 6 THz, the inclusion of quantum effects changes the phonon contributions by less than 1% (see Figure 4.4 and Section S.17 in our work on arXiv,[35] making the calculations relevant to the room temperature experiments.

4.3 Enhancement in ion migration caused by driving conduction-relevant phonon modes

To experimentally test the predicted importance of rocking and bottleneck opening modes, the LLTO is irradiated up to 4.5 THz (bandwidth set by the generation process) and then the perturbation to the impedance is measured. LLTO was synthesized and structurally characterized as described in Chapter 2.4. To prepare the sample for the EIS measurements, the resulting powder was pressed into a pellet with a diameter of 9 mm and a thickness of 0.7 mm under 2 tons of force (308.3 MPa of pressure), yielding a 75-76% pellet density. The pellet was subsequently annealed at 1100°C for 6 h at a ramp rate of 2°C / min over a bed of its mother powder. A 1.6 mm thick strip of Au was sputtered onto one side of the pellet with a 1 mm gap in the center for the light source to excite the LLTO and eliminate possible effects on the impedance from illuminating the Au. The in-plane electrode geometry enables EIS measurements under light excitation despite the shallow absorption depths for both the THz (6 μm) and 800 nm light (7 μm). Cu contacts were used to contact the sputtered Au to the 1260A Solartron impedance analyzer for EIS measurements. An open cell set-up was employed to allow THz irradiation to excite the sample without compromising average power.

The conductivity was then measured by an AC Impedance method over a frequency range of 32 MHz to 1 Hz with an applied 100 mV sinusoidal amplitude between 298 K – 333 K with and without the excitation source using the Solartron 1260A frequency response analyzer. A copper mesh faraday cage was custom-made with a 1.4 mm copper wire spacing to reduce the noise in EIS measurements due to electromagnetic interference from the environment.

Before conducting the laser-driven impedance measurement, we perform variable-temperature EIS measurements as a control for comparing the ion migration enhancement induced by photo-excitation to that enhanced by DC heating.

The Nyquist plots for LLTO under no laser excitation between 298 K - 333 K are

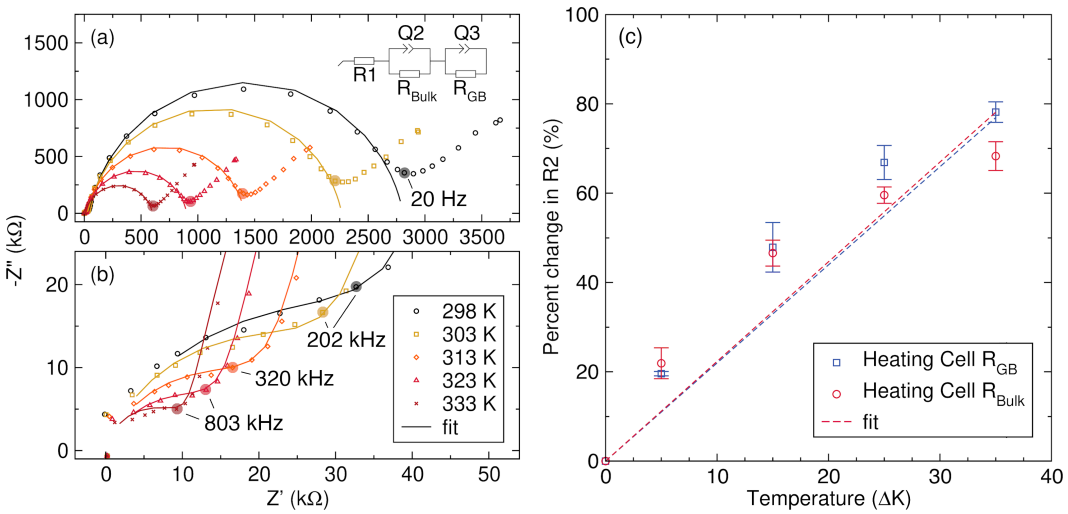

Figure 4.5: (a) Grain boundary semi-circle fit to a $R_1 + R_{GB}/Q2 + R_{Bulk}/Q3$ circuit. (b) Bulk impedance semi-circle fit to a $R_1 + R_{GB}/Q2 + R_{Bulk}/Q3$ circuit. The symbols represent the raw data and the lines represent the respective equivalent circuit fits. (c) Percent change in R_{GB} and R_{bulk} upon heating. The R^2 is 0.9955 and 0.9634 for the R_{GB} and R_{bulk} respectively. 1 K of heat causes a 2.20% and 2.23% change in the grain boundary and bulk impedances respectively.

shown in Figure 4.5a-b. The impedance data for the bulk feature (Figure (4.5a) and grain boundary feature (Figure 4.5b) impedance were fit to the $R1 + R_{bulk}/Q2 + R_{GB}/Q3$ circuit shown in each respective plot. As temperature increases, the impedance decreases for Z' and Z" because of the increase in population and mode types in the phonon bath, in agreement with Equation 1.1. The semi-circle fit corresponding to the grain boundary contribution (Figure 4.5b) has a different shape than the bulk contribution (Figure 4.5a), likely because the bulk semi-circle partially overlaps with the grain boundary feature. The change in impedance is linear with temperature within error (Figure 4.5c).

To generate the desired broadband THz fields to excite ion migration-relevant phonon modes up to 6 Thz, a 1 kHz, 38 fs, 13 mJ pulse centered at 800 nm is first produced via regenerative amplification in a Ti:Sapphire laser (Coherent Legend Elite Duo). The output beam is split by a 25:75 beam splitter, with the more intense beam approximately 10 μJ in energy used to pump an optical parametric amplifier (OPA, TOPAS, Light Conversion Inc.) and generate a 2.1 W, 1440 nm output signal beam. The signal beam goes through a mechanical delay stage and a chopper set at 250 Hz to reduce the average power to 1.1 W to not burn the DAST (4-N,N-dimethylamino-4'-N'-methyl-stilbazolium tosylate) crystal or THZ emitter, which was purchased

from Swiss Terahertz. The μW output of the DAST crystal, which when focused through three OAPs into a 250 μm beam spot, gives a peak field intensity in the 100 kV/cm range. The chamber was purged under inert gas (N_2) to minimize water absorption and to increase the field strength of the THz source. The THz field was characterized using electro-optical detection in 30 μm GaP. The full diagram of the optical set up is shown in Figure 4.6.

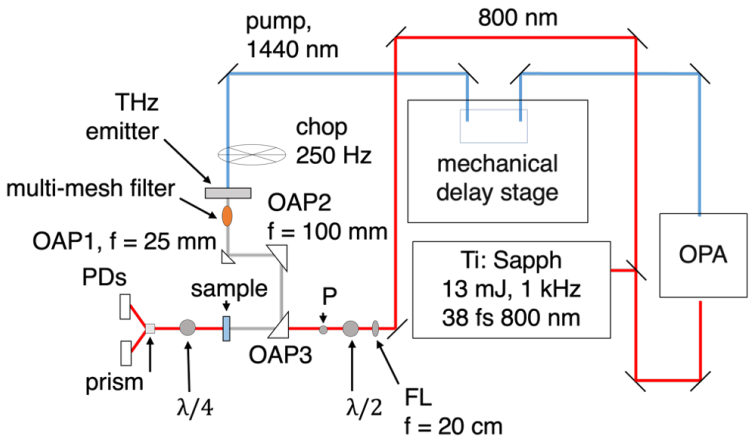

Figure 4.6: Diagram of the THz generation set up. OPA: Optical Parameter Amplifier. OAP: Off-Axis Parabolic. FL: focal lens, P: polarizer, PDs: Photodiodes.

EIS measurements are then repeated while driving the THz phonon modes with 0.26-1.6 mW of THz power focused to a 250 µm beam diameter and 250 Hz repitition rate using an open electrochemical cell. The average power of the THz field was determined using a pyroelectric THz joulemeter. Details on the procedure can be found in Appendix K.

When the 0.7 – 4.5 THz modes are driven, a linear decrease in the Z' on the order of 100s of Ω is measured, scaling with increased power (Figure 4.7). As shown in the inset, the shift in the complex impedance is reproducible between samples and trials. Specifically, 1 mW of power of THz causes a 0.87% change in grain boundary impedance (R^2 = 0.9976) and a 0.78% change in bulk impedance (R^2 = 0.9905). To show the reversibility of the observed phenomenon, single transient frequency impedance (SFIT) measurements were taken. To set up an SFIT measurement, an EIS scan from 1 MHz to 1 Hz was taken using a SP150 Biologic potentiostat to determine the frequency of the grain boundary intercept. The real, imaginary, and total impedance was then measured as a function of time (millisecond resolution)

at the single frequency determined by the previous EIS step with and without the illuminated excitation source. The change is reversible, reverting to the pre-illumination impedance after illumination (Figure 4.8).

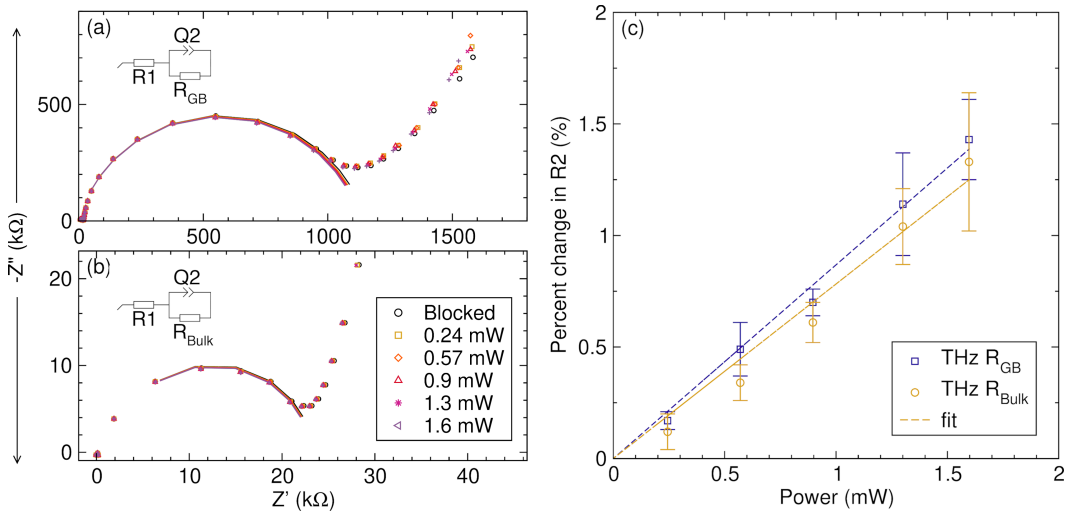

Figure 4.7: Nyquist plots of LLTO showing the decrease in impedance upon THz excitation from 0 to 1.6 mW of average pulse power and corresponding plot of linear shift in impedance with increasing average power (a) Grain boundary semi-circle fit to a $R1 + R_{GB}/Q2$ circuit. (b) Bulk impedance semi-circle fit to a $R1 + R_{Bulk}/Q2$ circuit. The symbols represent the raw data and the lines represent the respective equivalent circuit fits. (c) Percent change in R_{GB} and R_{bulk} upon irradiation of a THz excitation source (1 kHz repetition rate, fs pulsed). The R^2 is 0.9976 and 0.9905 for the R_{GB} and R_{bulk} respectively. 1 mW of power causes a 0.87% and 0.78% change in the grain boundary and bulk impedances respectively.

Simultaneous EIS measurements under illumination were repeated with NIR and MIR light. The NIR light excites laser-induced heating effects, i.e., acoustic phonon modes due to its lack of absorption in LLTO (Figure 3.1) while the MIR light excites the La-O mode at 11.6 µm. The NIR (800 nm) and MIR light sources were generated using a regenerative Ti:Sapphire laser amplifier operating at 1 kHz. The 800 nm output was sent through an optical parametric amplifier for the NIR light and a difference frequency generation unit for the MIR light. The 11.6 µm mode was chosen because it fell within the limitations of the generated MIR light (9.4–14.16 µm centered at 11.8 µm with 0.1 mW average power focused to a 250 µm beam diameter). The acoustic phonon mode baths associated with random thermal vibrations or heat[36] were populated using 5-25 mW of 800 nm pulsed light focused into a 250 µm beam diameter at a 1 kHz repitition rate. Although the generated MIR light was not strong enough to measure a change in impedance,

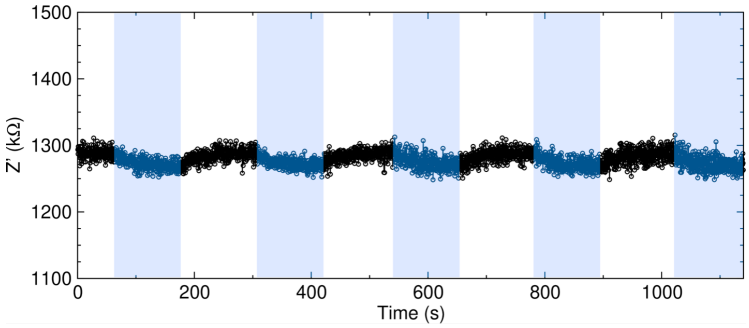

Figure 4.8: Reversible change in Z' of LLTO upon illumination and subsequent removal of the THz field source at 1.6 mW. The total impedance relaxes from the illuminated state to dark impedance measurement in approximately 100 seconds. The total impedance returns to the excited state from dark state upon illumination in approximately 100 seconds.

the 800 nm showed a linear change in impedance with increasing average power as shown in Figure 3.5.

The shift in R_{bulk} for the 800 nm excitation and THz excitation is replotted in 4.9 for ease of comparison.

We find that incoherently heating the acoustic phonon bath with the 800 nm light induces a 0.10% decrease in R_{bulk} per mW of power compared to the 0.78% decrease in R_{bulk} per mW for exciting rocking modes with THz light, in line with the predictions from *ab initio* computational modeling which predict a significant enhancement associated with THz-range vibrational modes. Figure 4.9 not only demonstrates the greater enhancement induced by the THz frequency range excitation(as shown by the steeper slope), but also rules out any nonlinear effects, given the linear correlation between the excitation enhancement and power for both wavelengths.

The normalized change in impedance per average power density of the beam for each excitation frequency is compared in Figure 4.10, which include the above-band gap excitation results discussed in Chapter 3.3. By choosing the average power density as the normalization factor, comparison of the enhancement across different excitation wavelengths with varied spot sizes and repetition rates is possible. Comparison of the normalized enhancement shows that a 48% change in $\Delta R_{bulk}(mW * cm^{-2})^{-1} x 10^{-5}$ for the broadband THz excitation of rocking modes, while laser-induced heating gives a calculated 5.0% change in $\Delta R_{bulk}(mW * cm^{-2})^{-1} x 10^{-5}$. No detectable

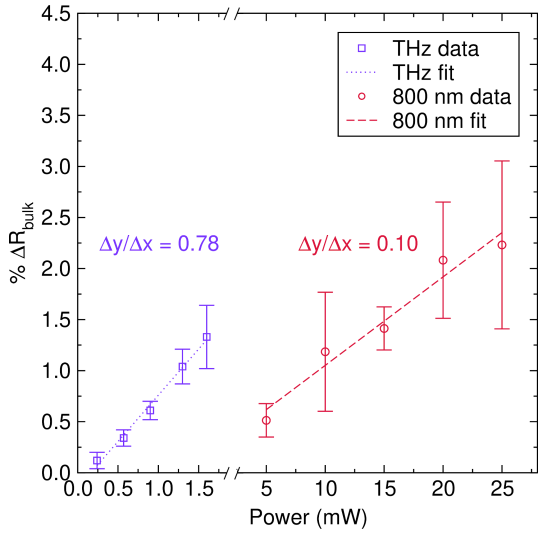

Figure 4.9: The shift in R_{bulk} for the 800 nm excitation and THz excitation. The shifts from the respective Nyquist plots corresponding to the bulk feature plotted against power with equal spot sizes of 250 μm, showing a 0.78% percent decrease in resistance per mW of power for the THz light excitation (R^2 = 0.9918) and a 0.10% change in bulk resistance per mW of power for the 800 nm light excitation (R^2 = 0.9905).

change using the 1 μm, 1.5 μm, or 9.4 - 14.16 μm light was measured as shown in Figure 4.10. The results are consistent with our theoretical calculations where the optical modes contribute significantly less to ion hopping above 10 THz (30 μm m) as shown in Figure 4.2, which possibly justifies why no detectable changes are observed. In Figure 4.10b-d, we note the modes which are excited at each wavelength. Evidently, we find that the excitation of highly absorbing rocking modes is the predominant mechanism by which ion migration can be enhanced when considering phonon excitations from the NIR-to-THz wavelength range.

The relative decrease in R_{bulk} with THz light driving of rocking modes is almost ten-fold compared to that of the 800 nm excitation, which is predicted to incoherently heat the sample. The significant difference in enhancement demonstrates that the theoretically predicted phonon-ion coupled modes promote ion migration at higher rates than uncorrelated thermal, acoustic phonon induced hops.

At the macroscopic scales probed by the several hundred micron diameter focus of the linear THz data shown in Figure 4.10d, the absorption coefficient of LLTO above 2-3 THz exceeds 1000 cm^{-1}, values in excess of those seen in high dipole moment

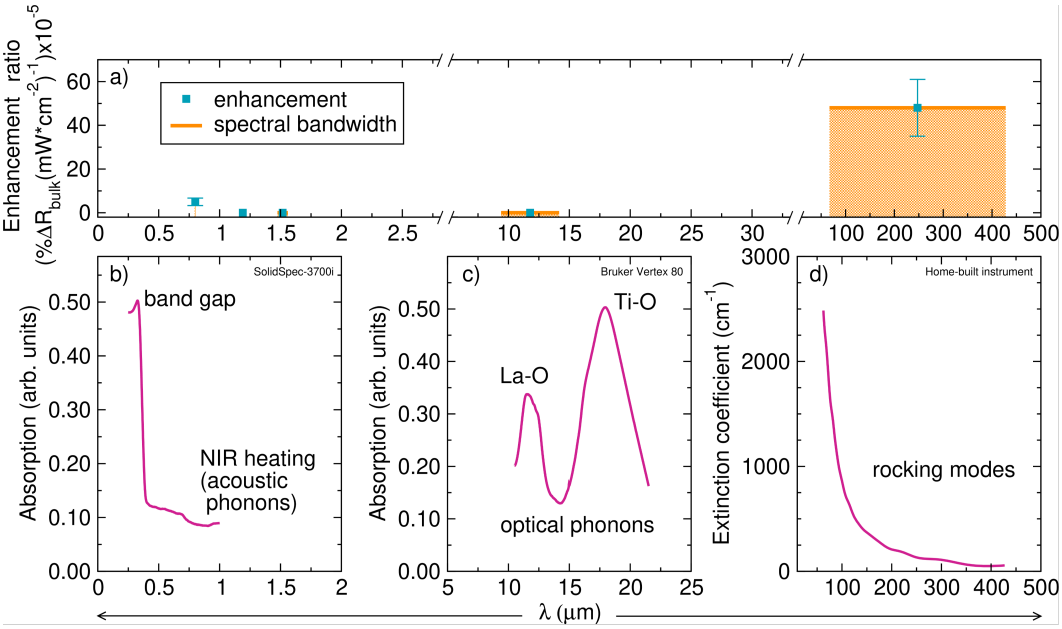

Figure 4.10: Enhancement in bulk ion migration due to illumination across DC heating, near-IR (NIR), mid-IR (MIR), and THz light. (a) Enhancement ratios (cyan squares) reported in $\%\Delta R_{bulk}(mW * cm^{-2})^{-1}x10^{-5}$, calculated from exciting LLTO between NIR – THz light. The width of the horizontal orange bar represents the spectral bandwidth of the excitation pulse. The NIR enhancement corresponds to incoherent heating of the acoustic phonon bath. The MIR excitation corresponds to coherent driving of optical phonon modes, which was inconclusive for the same excitation density as the THz modes. The THz light coherently drives highly contributing modes, showing the largest relative enhancement. (b-d), Absorption spectra of LLTO (magenta) in the (b) NIR, (c) MIR, and (d) THz regions obtained using UV-vis spectroscopy, FTIR, and THz transmission, respectively. The NIR absorption plot was measured on a Shimadzu SolidSpec-37000iDUV spectrophotometer, the MIR was measured on the Bruker Vertex 80, and the THz absorption was measured on a custom THz time-domain spectroscopy set up.

liquids such as water and acetonitrile.[37] The multi-octave bandwidth of the THz pulse enables both resonant electric dipole-allowed transitions and sum frequency excitation via the polarizability operator (that is, Raman active modes).[38] The absolute values and smooth nature of the cross sections suggests that the transition dipoles are large, and that local variability in the Li/La ratio impacts the mode frequencies, in agreement with theory. This is further corroborated by Raman measurements of $Li_{3x}La_{2/3-x}TiO_3$ ($0.04 \leq x \leq 0.15$), where the local distribution of Li^+ and La^{3+} alters the spectroscopic signature of modes associated with the TiO_6 octahedra.[17] Absorption coefficients at the level of Figure 4.10d require significant

coupling of octahedral rocking with ion displacement, likely with potential energy surfaces that are quite flat for small displacements. Determining the fraction of THz modes that contribute to actual ion hopping/conductivity requires careful comparison to theory of the hopping mechanism and action spectroscopy to quantitatively assess the role of THz excitation on ion hopping.

Having performed these measurements, we believe that the enhancement due to THz laser excitation can be attributed to phonon-ion couplings which increase ionic conduction. However, the generation of electronic carriers and heating effects must also be considered. Any electronic contribution toward the total measured impedance, including the excitation of electronic carriers due to THz fields, are unlikely in LLTO, because (1) there is no change to the measured open circuit voltage during the EIS experiments, (2) the THz radiation is less than 0.025 eV,[39] which is sufficiently below the 2.1 eV band gap of LLTO,[40] and (3) no nonlinear effects are observed, as demonstrated by Figure 4.9. Therefore, the THz fields are unlikely to generate electronic carriers or have sufficient energies to promote enhanced electronic conductivity in LLTO. However, we note that photo-enhanced electronic conductivity is possible in other materials with smaller energy-gap transitions.[20] In the presented work, the measured changes in impedance should be attributed to changes in ion hopping. Additionally, no dependence on excitation near the contacts on the LLTO was found at the metal-material junction, ruling out the generation of carriers on the metal contacts.

Deconvoluting thermal enhancements of ion hopping from those associated with exciting targeted lattice-driven dynamics is non-trivial. The measurement of a single Nyquist plot that captures the bulk semi-circular feature requires at least 10s of seconds with five points measured per decade, no averaging, and a narrow frequency sweep range, preventing the direct probing of the “peak” temperature change induced by the laser which occurs in less than 100 ns. On the milliseconds-to-seconds timescales of the EIS measurements, we expect both excitations to have contributions from the decay of the initial phonon excitation into heat. However, if heating is the only mechanism by which the laser enhances ion hopping for both the 800 nm and THz light excitations, we would expect these excitations to cause similar levels of enhancement when normalized, given their similar penetration depths. Instead, the THz light leads to an order of magnitude larger enhancement compared to the 800 nm light when normalized by power density Figure 4.10a. Such a discrepancy requires further investigation into the differences in laser-induced

heating and longer-term photo-modulation effects between both excitation energies.

To more accurately compare the enhancements in ion migration between the laser-induced heating and THz-induced rocking modes and separate contributions due to heating and photo-modulated ion hopping at milliseconds-or-longer timescales, we adopt the FDTD method as previously described in Chapter 3.6. After identifying the absorption depths of both 800 nm and THz light, the model is used to produce cross-sectional heating maps of the sample which show differences in the temperature gradient between the THz and 800 nm light (Figures D.6 and D.1). Given the challenges in reconciling the region probed electrochemically with that heated by the laser, we aim estimate an upper bound for heating relative to the milliseconds-or-longer timescales probed by EIS. We note that the ultrafast laser pulses will induce peak temperatures far greater than the metric we define, but the timescales at which the temperature fluctuations occur vastly exceed that of the EIS measurement to manifest as measurable changes in the EIS data presented. As such, we instead capture the average maximum temperature in the sample at all time points during and after the final pulse, once the sample has reached a baseline thermal steady state, which occurs within 100 ms (Figures D.3 and D.7). With this metric, we find that the 800 nm light induces a temperature change of 0.03 K/mW while the THz light induces a change of 0.02 K/mW.

Excitation Source (nm)	**Calculated Thermal Effects (%ΔR/mW)**	**Measured Enhancement (%ΔR/mW)**
800 nm	0.07	0.10
0.7 - 4.5 THz	0.04	0.78

Table 4.2: Deconvolution of thermal-induced ion enhancement from the total measured enhancement of ion migration.

In Table 4.2, we use the thermal enhancement factors in K/mW to differentiate the computed thermal effects from the measured total enhancement, the slope in Figure 4.9, which also has contributions associated with the population of phonon baths in LLTO. To ascertain the ion migration enhancements associated with calculated thermal effects, we utilize Equation 4.5:

$$thermal\ effects = \frac{\Delta K}{mW} * \frac{\%\Delta R}{\Delta K} \tag{4.5}$$

We use the slope for the change in sample resistance per degree Kelvin in Figure

4.5 and multiply this factor by the computed wavelength-dependent heating factors, discussed above, thus evaluating Equation 4.5. The thermal effects value determined by Equation 4.5 is a quantitative measure of the upper limit for thermal-induced heating effects on timescales relevant to EIS, in units of $\%\Delta R/W$, as depicted in the second column of Table 4.2. Finally, we compare the computed thermal effects to the slopes of Figure 4.9, shown in the third column in Table 4.2.

From Table 4.2, we can find the fraction of total enhancement which can be attributed to thermal effects as compared to the total measured enhancement and determine that 70% of the enhancement at 800 nm is associated with thermal heating. We note that the 30% discrepancy here likely indicates that laser heating and resistor heating impact ion hopping differently. However, because most of the enhancement can be attributed to thermal effects at 800 nm, we believe that this wavelength measures the enhancement associated with populating the acoustic phonon bath, or heating the sample. For the THz excitation, we determine the fraction of the total enhancement which is associated with thermal effects. We find that only 5% of the THz-induced enhancement is associated with heating, while the other 95% is attributed to further photo-modulation effects associated with the filling of the population of contributing THz rocking modes, in qualitative agreement with the computational work presented in this paper. By parsing out the thermal contributions from the total measured enhancement, we demonstrate that we are indeed probing the photo-modulation of ion hopping as opposed to purely laser-induced heating of the sample.

In conclusion, we compare the relative role of acoustic, optical, and THz phonon modes in ion migration through laser-frequency-selective perturbation of EIS measurements. By directly driving highly contributing phonon modes, which are most likely rocking modes in the 0.7 – 4.5 THz region, a ten-fold enhancement in ion migration is measured relative to incoherent heating. Using an FDTD model, we attribute the majority of this enhancement to laser-driven photo-modulation effects. The significant contribution of rocking modes to ion hopping in the <4.5 THz region agrees with ab initio calculations, validating its use in exploring phonon-mediated hopping and confirming that only a small percentage of phonon mode types lead to a large amount of ion migration. However, we note that the broadband nature of the THz light limits our ability to experimentally distinguish contributions of coupled ion-phonon rocking modes versus modes that open the bottle neck, instead relying on theory for interpretation. Future work in selectively driving different

phonon mode types with narrow-band THz pulses would be instrumental in further developing the methods we that established.[41]

Nonetheless, the findings herein can aid in the design of future solid-state ion conductors. The results also hint at the potential for exploring light-induced states for ionic transport that could lead to new applications and sciences that require new ultrafast spectroscopy techniques.

The work presented in this chapter was financially supported by the National Science Foundation, Air Force Office of Science & Research, and David & Lucile Packard Foundation. Financial support for creating the heating cell is from grant #CS-CSA-2022-068 from the Research Corporation for Science Advancement.

References

[1] Zhenming Xu et al. "Anharmonic cation–anion coupling dynamics assisted lithium-ion diffusion in sulfide solid electrolytes". In: *Advanced Materials* 34 (49), p. 2207411. ISSN: 49. DOI: 10.1002/adma.202207411. URL: https://onlinelibrary.wiley.com/doi/abs/10.1002/adma.202207411.

[2] Tomohide Morimoto et al. "Microscopic ion migration in solid electrolytes revealed by terahertz time-domain spectroscopy". In: *Nature Communications* 10.1 (June 17, 2019). Number: 1 Publisher: Nature Publishing Group, p. 2662. ISSN: 2041-1723. DOI: 10.1038/s41467-019-10501-9. URL: https://www.nature.com/articles/s41467-019-10501-9 (visited on 09/22/2022).

[3] Andrey D. Poletayev et al. "The persistence of memory in ionic conduction probed by nonlinear optics". In: *Nature* 625.7996 (Jan. 2024). Publisher: Nature Publishing Group, pp. 691–696. ISSN: 1476-4687. DOI: 10.1038/s41586-023-06827-6. URL: https://www.nature.com/articles/s41586-023-06827-6 (visited on 03/05/2024).

[4] A. X. Gray et al. "Ultrafast terahertz field control of electronic and structural interactions in vanadium dioxide". In: *Physical Review B* 98.4 (July 2, 2018). Publisher: American Physical Society, p. 045104. DOI: 10.1103/PhysRevB.98.045104. URL: https://link.aps.org/doi/10.1103/PhysRevB.98.045104 (visited on 09/22/2022).

[5] Kiarash Gordiz et al. "Enhancement of ion diffusion by targeted phonon excitation". In: *Cell Reports Physical Science* 2.5 (May 19, 2021), p. 100431. ISSN: 2666-3864. DOI: 10.1016/j.xcrp.2021.100431. URL: https://www.sciencedirect.com/science/article/pii/S2666386421001260 (visited on 09/22/2022).

[6] Zhizhen Zhang et al. "Targeting superionic conductivity by turning on anion rotation at room temperature in fast ion conductors". In: *Matter* 2.6 (June 3,

2020). Publisher: Elsevier, pp. 1667–1684. ISSN: 2590-2393, 2590-2385. DOI: 10.1016/j.matt.2020.04.027. URL: https://www.cell.com/matter/abstract/S2590-2385(20)30233-2 (visited on 10/12/2022).

[7] Thorben Krauskopf et al. "Comparing the descriptors for investigating the influence of lattice dynamics on ionic transport using the superionic conductor $Na_3 PS_{4-x}Se_x$". In: *Journal of the American Chemical Society* 140.43 (Oct. 31, 2018), pp. 14464–14473. ISSN: 0002-7863, 1520-5126. DOI: 10.1021/jacs.8b09340. URL: https://pubs.acs.org/doi/10.1021/jacs.8b09340 (visited on 11/17/2022).

[8] Roman Schlem et al. "Insights into the lithium sub-structure of superionic conductors Li_3YCl_6 and Li_3YBr_6". In: *Chemistry of Materials* 33.1 (Jan. 12, 2021). Publisher: American Chemical Society, pp. 327–337. ISSN: 0897-4756. DOI: 10.1021/acs.chemmater.0c04352. URL: https://doi.org/10.1021/acs.chemmater.0c04352 (visited on 02/02/2023).

[9] Isabel Hanghofer, Bernhard Gadermaier, and H. Martin R. Wilkening. "Fast rotational dynamics in argyrodite-Type Li_6PS_5X (X: Cl, Br, I) as seen by ^{31}P nuclear magnetic relaxation—on cation–anion coupled transport in thiophosphates". In: *Chemistry of Materials* 31.12 (June 25, 2019), pp. 4591–4597. ISSN: 0897-4756, 1520-5002. DOI: 10.1021/acs.chemmater.9b01435. URL: https://pubs.acs.org/doi/10.1021/acs.chemmater.9b01435 (visited on 12/08/2022).

[10] Zhizhen Zhang and Linda F. Nazar. "Exploiting the paddle-wheel mechanism for the design of fast ion conductors". In: *Nature Reviews Materials* 7.5 (May 2022). Number: 5 Publisher: Nature Publishing Group, pp. 389–405. ISSN: 2058-8437. DOI: 10.1038/s41578-021-00401-0. URL: https://www.nature.com/articles/s41578-021-00401-0.

[11] Bingkai Zhang et al. "Cooperative transport enabling fast Li-ion diffusion in Thio-LISICON $Li_{10}SiP_2S_{12}$ solid electrolyte". In: *Nano Energy* 62 (Aug. 2019), pp. 844–852. ISSN: 22112855. DOI: 10.1016/j.nanoen.2019.05.085. URL: https://linkinghub.elsevier.com/retrieve/pii/S2211285519304914 (visited on 06/06/2021).

[12] Arihant Bhandari and Jishnu Bhattacharya. "Origin of fast ion conduction in $Li_{10}GeP_2S_{12}$, a superionic conductor". In: *The Journal of Physical Chemistry C* 120.51 (Dec. 29, 2016), pp. 29002–29010. ISSN: 1932-7447, 1932-7455. DOI: 10.1021/acs.jpcc.6b10967. URL: https://pubs.acs.org/doi/10.1021/acs.jpcc.6b10967 (visited on 06/06/2021).

[13] Sokseiha Muy et al. "Tuning mobility and stability of lithium ion conductors based on lattice dynamics". In: *Energy & Environmental Science* 11.4 (2018), pp. 850–859. ISSN: 1754-5692, 1754-5706. DOI: 10.1039/C7EE03364H. URL: http://xlink.rsc.org/?DOI=C7EE03364H (visited on 10/24/2022).

[14] Marvin A. Kraft et al. “Influence of lattice polarizability on the ionic conductivity in the lithium superionic argyrodites Li_6PS_5X (X = Cl, Br, I)”. In: *Journal of the American Chemical Society* 139.31 (Aug. 9, 2017), pp. 10909–10918. ISSN: 0002-7863, 1520-5126. DOI: 10.1021/jacs.7b06327. URL: https://pubs.acs.org/doi/10.1021/jacs.7b06327 (visited on 06/06/2021).

[15] Xinyu Li and Nicole A. Benedek. “Enhancement of ionic transport in complex oxides through soft lattice modes and epitaxial strain”. In: *Chemistry of Materials* 27.7 (Apr. 14, 2015), pp. 2647–2652. ISSN: 0897-4756, 1520-5002. DOI: 10.1021/acs.chemmater.5b00445. URL: https://pubs.acs.org/doi/10.1021/acs.chemmater.5b00445 (visited on 10/24/2022).

[16] Sonia Stramare, Venkataraman Thangadurai, and Werner. Weppner. “Lithium lanthanum titanates: A review”. In: *Chemistry of Materials* 15.21 (Oct. 2003), pp. 3974–3990. ISSN: 0897-4756, 1520-5002. DOI: 10.1021/cm0300516. URL: https://pubs.acs.org/doi/10.1021/cm0300516 (visited on 06/06/2021).

[17] Xin Guo, Pardha Saradhi Maram, and Alexandra Navrotsky. “A correlation between formation enthalpy and ionic conductivity in perovskite-structured $Li_{3x}La_{0.67-x}TiO_3$ solid lithium ion conductors”. In: *Journal of Materials Chemistry A* 5.25 (2017), pp. 12951–12957. ISSN: 2050-7488, 2050-7496. DOI: 10.1039/C7TA02434G. URL: http://xlink.rsc.org/?DOI=C7TA02434G (visited on 06/07/2021).

[18] Michael Först et al. “Nonlinear phononics as an ultrafast route to lattice control”. In: *Nature Physics* 7.11 (Nov. 2011). Number: 11 Publisher: Nature Publishing Group, pp. 854–856. ISSN: 1745-2481. DOI: 10.1038/nphys2055. URL: https://www.nature.com/articles/nphys2055 (visited on 09/22/2022).

[19] Tobia F. Nova et al. “An effective magnetic field from optically driven phonons”. In: *Nature Physics* 13.2 (Feb. 2017). Number: 2 Publisher: Nature Publishing Group, pp. 132–136. ISSN: 1745-2481. DOI: 10.1038/nphys3925. URL: https://www.nature.com/articles/nphys3925 (visited on 10/10/2022).

[20] Wanzheng Hu et al. “Optically enhanced coherent transport in $YBa_2Cu_3O_{6.5}$ by ultrafast redistribution of interlayer coupling”. In: *Nature Materials* 13.7 (July 2014). Number: 7 Publisher: Nature Publishing Group, pp. 705–711. ISSN: 1476-4660. DOI: 10.1038/nmat3963. URL: https://www.nature.com/articles/nmat3963 (visited on 10/10/2022).

[21] Michael J. Rice and W. L. Roth. “Ionic transport in super ionic conductors: a theoretical model”. In: *Journal of Solid State Chemistry* 4.2 (Mar. 1, 1972), pp. 294–310. ISSN: 0022-4596. DOI: 10.1016/0022-4596(72)90121-1. URL: https://www.sciencedirect.com/science/article/pii/0022459672901211 (visited on 05/21/2025).

[22] Tobia F. Nova et al. “Metastable ferroelectricity in optically strained SrTiO3”. In: *Science* 364.6445 (June 14, 2019). Publisher: American Association for the Advancement of Science, pp. 1075–1079. DOI: 10.1126/science.aaw4911. URL: https://www.science.org/doi/full/10.1126/science.aaw4911 (visited on 04/04/2023).

[23] Frank Y. Gao et al. “Snapshots of a light-induced metastable hidden phase driven by the collapse of charge order”. In: *Science Advances* 8.29 (July 22, 2022). Publisher: American Association for the Advancement of Science, eabp9076. DOI: 10.1126/sciadv.abp9076. URL: https://www.science.org/doi/10.1126/sciadv.abp9076 (visited on 11/05/2024).

[24] Zehua Chen et al. “Unified theory for light-induced halide segregation in mixed halide perovskites”. In: *Nature Communications* 12.1 (May 11, 2021). Number: 1 Publisher: Nature Publishing Group, p. 2687. ISSN: 2041-1723. DOI: 10.1038/s41467-021-23008-z. URL: https://www.nature.com/articles/s41467-021-23008-z (visited on 04/04/2023).

[25] Sergiu Draguta et al. “Rationalizing the light-induced phase separation of mixed halide organic–inorganic perovskites”. In: *Nature Communications* 8.1 (Aug. 4, 2017). Number: 1 Publisher: Nature Publishing Group, p. 200. ISSN: 2041-1723. DOI: 10.1038/s41467-017-00284-2. URL: https://www.nature.com/articles/s41467-017-00284-2 (visited on 04/04/2023).

[26] Hamid Reza Seyf et al. “Using Green-Kubo modal analysis (GKMA) and interface conductance modal analysis (ICMA) to study phonon transport with molecular dynamics”. In: *Journal of Applied Physics* 125.8 (Feb. 22, 2019), p. 081101. ISSN: 0021-8979. DOI: 10.1063/1.5081722. URL: https://doi.org/10.1063/1.5081722 (visited on 10/23/2024).

[27] Martin T. Dove. *Introduction to Lattice Dynamics*. Cambridge Topics in Mineral Physics and Chemistry. Cambridge: Cambridge University Press, 1993. ISBN: 978-0-521-39293-8. DOI: 10.1017/CBO9780511619885. URL: https://www.cambridge.org/core/books/introduction-to-lattice-dynamics/85943FCCF2BA2797CE53D96D3A8BFCBF (visited on 10/23/2024).

[28] Kiarash Gordiz and Asegun Henry. “Phonon transport at interfaces: Determining the correct modes of vibration”. In: *Journal of Applied Physics* 119.1 (Jan. 4, 2016), p. 015101. ISSN: 0021-8979. DOI: 10.1063/1.4939207. URL: https://doi.org/10.1063/1.4939207 (visited on 10/23/2024).

[29] Hamid Reza Seyf and Asegun Henry. “A method for distinguishing between propagons, diffusions, and locons”. In: *Journal of Applied Physics* 120.2 (July 11, 2016), p. 025101. ISSN: 0021-8979. DOI: 10.1063/1.4955420. URL: https://doi.org/10.1063/1.4955420 (visited on 10/23/2024).

[30] Odile Bohnke et al. “In search of the cubic phase of the Li+ ion-conducting perovskite $La_{2/3x}Li_{3x}TiO_3$: structure and properties of quenched and in situ heated samples”. In: *Solid State Ionics* 149.3 (Aug. 2, 2002), pp. 217–226. ISSN: 0167-2738. DOI: 10.1016/S0167-2738(02)00142-X. URL: https://www.sciencedirect.com/science/article/pii/S016727380200142X (visited on 10/23/2024).

[31] Michele Catti. “Short-range order and Li^+ ion diffusion mechanisms in $Li_5La_9\square_2(TiO_3)_{16}$ (LLTO)”. In: *Solid State Ionics* 183.1 (Feb. 11, 2011), pp. 1–6. ISSN: 0167-2738. DOI: 10.1016/j.ssi.2010.12.016. URL: https://www.sciencedirect.com/science/article/pii/S0167273810006818 (visited on 10/23/2024).

[32] Michele Catti. “First-Principles Modeling of Lithium Ordering in the LLTO ($Li_xLa_{2/3-x}TiO_3$) Superionic Conductor”. In: *Chemistry of Materials* 19.16 (Aug. 1, 2007). Publisher: American Chemical Society, pp. 3963–3972. ISSN: 0897-4756. DOI: 10.1021/cm0709469. URL: https://doi.org/10.1021/cm0709469 (visited on 10/23/2024).

[33] Michele Catti. “Ion Mobility Pathways of the Li^+ Conductor $Li_{0.125}La_{0.625}TiO_3$ by Ab Initio Simulations”. In: *The Journal of Physical Chemistry C* 112.29 (July 1, 2008). Publisher: American Chemical Society, pp. 11068–11074. ISSN: 1932-7447. DOI: 10.1021/jp803345y. URL: https://doi.org/10.1021/jp803345y (visited on 10/23/2024).

[34] Jeffrey G. Smith and Donald J. Siegel. “Low-temperature paddlewheel effect in glassy solid electrolytes”. In: *Nature Communications* 11.1 (Mar. 20, 2020). Number: 1 Publisher: Nature Publishing Group, p. 1483. ISSN: 2041-1723. DOI: 10.1038/s41467-020-15245-5. URL: https://www.nature.com/articles/s41467-020-15245-5 (visited on 10/14/2022).

[35] Kim H. Pham et al. “Correlated Terahertz phonon-ion interactions dominate ion conduction in solid electrolyte $Li_{0.5}La_{0.5}TiO_3$”. In: arXiv:2305.01632 (Mar. 6, 2024). DOI: 10.48550/arXiv.2305.01632. arXiv: 2305.01632[cond-mat,physics:physics]. URL: http://arxiv.org/abs/2305.01632 (visited on 03/09/2024).

[36] Mayanak K. Gupta et al. “Investigation of Low-Energy Lattice Dynamics and Their Role in Superionic Na Diffusion and Ultralow Thermal Conductivity of Na3PSe4 as a Solid-State Electrolyte”. In: *Chemistry of Materials* 36.23 (Dec. 10, 2024). Publisher: American Chemical Society, pp. 11377–11392. ISSN: 0897-4756. DOI: 10.1021/acs.chemmater.4c01553. URL: https://doi.org/10.1021/acs.chemmater.4c01553 (visited on 05/21/2025).

[37] Dean S. Venables and C. A. Schmuttenmaer. “Far-infrared spectra and associated dynamics in acetonitrile–water mixtures measured with femtosecond THz pulse spectroscopy”. In: *The Journal of Chemical Physics* 108.12 (Mar. 22, 1998), pp. 4935–4944. ISSN: 0021-9606. DOI: 10.1063/1.475902. URL: https://doi.org/10.1063/1.475902 (visited on 05/21/2025).

[38] Griffin Mead et al. “Sum-Frequency Signals in 2D-Terahertz-Terahertz-Raman Spectroscopy”. In: *The Journal of Physical Chemistry. B* 124.40 (Oct. 8, 2020), pp. 8904–8908. ISSN: 1520-5207. DOI: 10.1021/acs.jpcb.0c07935.

[39] Benjamin I. Greene et al. “Far-infrared light generation at semiconductor surfaces and its spectroscopic applications”. In: *IEEE Journal of Quantum Electronics* 28.10 (Oct. 1992). Conference Name: IEEE Journal of Quantum Electronics, pp. 2302–2312. ISSN: 1558-1713. DOI: 10.1109/3.159537.

[40] Lu Zhang et al. “Lithium lanthanum titanate perovskite as an anode for lithium ion batteries”. In: *Nature Communications* 11.1 (Dec. 2020), p. 3490. ISSN: 2041-1723. DOI: 10.1038/s41467-020-17233-1. URL: http://www.nature.com/articles/s41467-020-17233-1 (visited on 06/06/2021).

[41] Bo Liu et al. “Generation of narrowband, high-intensity, carrier-envelope phase-stable pulses tunable between 4 and 18 THz”. In: *Optics Letters* 42.1 (Jan. 1, 2017). Publisher: Optica Publishing Group, pp. 129–131. ISSN: 1539-4794. DOI: 10.1364/OL.42.000129. URL: https://opg.optica.org/ol/abstract.cfm?uri=ol-42-1-129 (visited on 09/22/2022).

Chapter 5

CONCLUSIONS AND FUTURE DIRECTIONS

In conclusion, the work presented sheds light on the complexity of interactions and correlations between the dynamic lattice with the migrating ion in LLTO using ultrafast impedance methods. We learn that a combination of optical phonons, rocking phonons, acoustic phonons, and electrostatic screening can all collectively influence the energy landscape of the ion migration pathway, notably by reducing the activation energy barriers associated with 4-O bottleneck that acts as the gate or saddle point to ion migration.

We achieve selective excitation of each lattice dynamic in study by tuning the resonant photo-excitation source between UV to THz frequencies of light, generally achieving narrowbandwidths that enable the decoupling of effects of one lattice dynamic from another. However, even with the ability to select single wavelengths to study corresponding lattice dynamic interactions, challenges in producing a strong enough excitation source to observe the changes in impedance or achieving a large enough SNR to confidently measure and validate the existence of a meaningful signal can render a conclusion indecisive. Future work in optimizing such signals through the design of resonators is crucial for expanding the technique to study other solid-state ion conductors that may also have correlated ion-hopping dynamics but show weaker responses to light excitation.

More broadly, there are a number of advancements not yet realized in this work that could greatly expand the capabilities of the laser-driven, ultrafast impedance technique and answer even more complex questions concerning correlated ion hopping mechanisms.

One current challenge lies in the ability to excite optical phonons with narrowband pulses. As shown in Chapter 4, exciting phonon modes using broadband pulses limits our experimental ability to distinguish the effects of different phonon mode-types based on frequency like that shown through computational methods. For instance, in Figure 4.2a-b, we see that the modes lying between 5 to 7.5 THz show the largest degrees of individual enhancement in comparison to modes below 4 THz and above 8 THz. By generating narrowband THz pulses centered at these distinct THz frequencies, we can identify and verify bands of frequencies that are suitable

for enhanced, correlated ion hopping for different classes of materials for improved structure-property designs. Although the generation of narrowband THz pulses has been demonstrated in literature,[1] field strengths are often compromised and can be too weak to measure with ultrafast impedance or non-time resolved impedance techniques. Efforts in achieving narrowband THz pulses with high field strengths would be key in advancing the proposed laser-driven technique. Moreover, the generation of excitation sources farther into the THz range (of up to 10 THz) would also be beneficial for studying ionic conductors with phonon modes that lie higher in frequency, such as $Li_7La_3Zr_{12}O_{12}$[2] and $Li_{10}GeP_2S_{12}$,[3] which have different ion hopping mechanisms and crystal structures compared to LLTO. In particular, theory suggests that concerted ion hopping is the dominant mechanism for ionic conduction in $Li_7La_3Zr_{12}O_{12}$ as opposed to LLTO, with minimal explanation for the origin of such behavior. Advancements in THz generation, frequency selectivity, field strengths, and range could very much expand our understanding of phonon modes and their role in ion hopping.

Generating narrowband pulses of NIR light at sufficient energies can be accomplished more easily compared to THz frequencies, but the efficiency of fourth harmonic generation is low compared to other wavelengths that can be produced using second or third harmonic generation, limiting the practical use of such excitation sources to study ionic conductors with even larger band gap energies. Advancements in improving the efficiency of different generation processes required to produce wavelengths continuously from the low UV up to THz would vastly improve the types of correlated dynamics that can be studied for different classes of ionic and mixed conductors that have different band gap energies, crystal structures, ion hopping channels, ion hopping mechanisms, and more.

Another area of interest is the exploration of cross couplings between different phonon mode types or lattice dynamics that can collectively enhance ion hopping in a non-summative way, or i.e. whether coupled phonons can induce enhancements larger than the summation of their individual counterparts. Considering that the 350 nm light excitation collectively induced optical phonon mode dynamics, octahedral rocking, and changes in the O-2p electron density occupation in LLTO, the cross coupling of multiple dynamical processes must be investigated more rigorously and systematically to truly understand the interplay of these correlations during ion hopping. Such studies would require the careful design of multi-pulse experiments to selectively excite unique phonon mode pairs and then measure their combined

effect on ion hopping. 2D and 3D spectroscopic measurements in literature have already been demonstrated for a variety of material classes[4] and can be adapted to study multi-correlated dynamics in solid-state ion conductors.

Lastly, time-resolved impedance measurements under THz excitation would definitively prove the role of phonons in ion hopping at their inherent timescales. Although we demonstrate time-resolved measurements for the 350 nm and 800 nm light excitations, a number of physical limitations prevent the successful demonstration at THz frequencies. The main challenge lies with the detection sensitivity of the real-time oscilloscope, which can be improved with careful design of a resonator that enhances the sample response without distortion of the signal. Additionally, the sample holder must be optimized to prevent the clipping of the THz pulses which already have minimal field strengths strong enough to perturb the sample and enable the measurement of a changed impedance. The sample holder must fulfill the aforementioned requirements while enabling a coaxial geometry that can receive the carrier signal from the signal generator, maintaining good contact between the gold pin and the copper short(minimizing air gaps), and enabling a large enough overlap in the volume of sample excited by the THz source and the carrier signal into the sample. Once the listed conditions are met and optimized, ultrafast impedance measurements at THz frequencies can enable incredibly valuable measurements that can be directly compared to and verified by computation models predicting the role of phonon modes at picosecond timescales. Such capabilities could answer long-debated questions and controversies concerning the role and existence of certain phonon modes in the ionic conduction pathway for ionic conductors like $LiBH_4$.[5] Answers to such questions can not only help enable the targeted design of superionic conductors with much higher success, but also provide another powerful means of improving and verifying how we model ultrafast lattice dynamics for higher-throughput materials discovery through machine learning methods, or even experimental-high-throughout studies of known materials classes to better identify properties that can enable superionic conduction.

Even with the described limitations, our proposed technique overcomes the challenges of other ultrafast time resolved approaches by utilizing the laser as a probe in an AC measurement, rather than as the pump source to initiate ion conduction. The described method ensures that the resulting transient or signal directly probes ion conduction. Although this study focuses on one type of Li^+ conductor with low electronic conductivity, extensions to mixed ion-electron conducting systems

is certainly possible. Additionally, the cost-effective, photo-modulated or action spectrum-like method utilizing EIS provides a more lab-accessible route to probe complex ion-couplings. Even though time-domain coupling and correlation information are lost, the relative impact of different electronic and vibrational interactions can still be compared.

References

[1] Carlo Vicario et al. "Narrow-band and tunable intense terahertz pulses for mode-selective coherent phonon excitation". In: *Applied Physics Letters* 117.10 (Sept. 8, 2020). Publisher: American Institute of Physics, p. 101101. ISSN: 0003-6951. DOI: 10.1063/5.0015612. URL: https://aip.scitation.org/doi/10.1063/5.0015612 (visited on 09/22/2022).

[2] F. Tietz et al. "Synthesis and Raman micro-spectroscopy investigation of Li7La3Zr2O12". In: *Solid State Ionics*. Special Issue for the E-MRS Spring Meeting Symposium C: "Solid State Ionics: Mass and Charge Transport Across and Along Interfaces of Functional Material" Strasbourg / France, May 14-17, 2012 230 (Jan. 10, 2013), pp. 77–82. ISSN: 0167-2738. DOI: 10.1016/j.ssi.2012.10.021. URL: https://www.sciencedirect.com/science/article/pii/S0167273812005942 (visited on 05/15/2025).

[3] Jusef Hassoun et al. "A structural, spectroscopic and electrochemical study of a lithium ion conducting Li10GeP2S12 solid electrolyte". In: *Journal of Power Sources* 229 (May 1, 2013), pp. 117–122. ISSN: 0378-7753. DOI: 10.1016/j.jpowsour.2012.11.130. URL: https://www.sciencedirect.com/science/article/pii/S0378775312018150 (visited on 05/15/2025).

[4] Margherita Maiuri, Marco Garavelli, and Giulio Cerullo. "Ultrafast spectroscopy: State of the art and open challenges". In: *Journal of the American Chemical Society* 142.1 (Jan. 8, 2020). Publisher: American Chemical Society, pp. 3–15. ISSN: 0002-7863. DOI: 10.1021/jacs.9b10533. URL: https://doi.org/10.1021/jacs.9b10533 (visited on 05/05/2023).

[5] Yingzhi Sun et al. "Enhanced ionic conductivity and lack of paddle-wheel effect in pseudohalogen-substituted Li argyrodites". In: *Matter* 5.12 (Dec. 2022), pp. 4379–4395. ISSN: 25902385. DOI: 10.1016/j.matt.2022.08.029. URL: https://linkinghub.elsevier.com/retrieve/pii/S2590238522005185 (visited on 05/15/2025).

Appendix A

DERIVATION OF SCATTERING PARAMETERS FROM CURRENT AND VOLTAGE FOR NETWORK ANALYSIS

A.1 One port networks

Network analysis is useful for analyzing and simplifying circuit modeling of a complex circuit system by only considering the current flow in and out of the system of interest. For example, if a circuit is modeled as a one port network with two terminals, it is assumed that current must (i) flow into the system and (ii) flow out of the system, as shown by I_1 as (+) or (−) respectively in Figure A.1.

If the magnitude of the current is equal, the voltage value V_1 at both terminals must also be equal.

An important assumption for network analysis is that the inner circuity of the components modeled is treated as a black box system, and only the final output at the terminal is analyzed. By invoking a black box assumption, the two-port network in a larger network can be characterized without fully defining the inside of the black box.

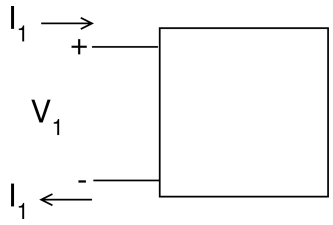

Figure A.1: One port or two-terminal system diagram for network analysis, where the current flow into the black box must equal the current flow out.

A.2 Two port networks

For the construction of the ultrafast impedance spectrometer described in Chapter 2.2, we use a directional coupler that employs three ports, where two of the three ports are coupled to each other and the remaining port is uncoupled. Here, we first discuss the theory behind a two-port network or four-terminal network to lay the foundation for a three-port network. As shown in Figure A.2, current I_1 and current I_2 both flow into the black box (direction shown as +) and out of the box (direction

shown as −). No independent sources are assumed, and that an external voltage is applied to both sides to produce the respective currents.

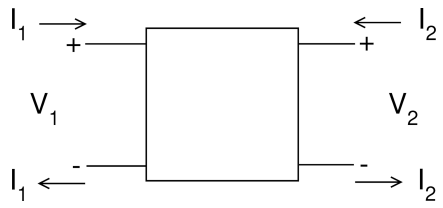

Figure A.2: Two port or four-terminal system diagram for network analysis, where the current flow in must equal the current flow out for a pair of terminals on the same plane of the black box.

Network analyzers are designed to directly measure the scattering parameter at each port, describing how the waves travel along the transmission line. From the scattering parameter, impedances can be calculated.

Here, we first show the derivation of impedances which are defined as the ratio between AC voltage and current, from which we derive scattering parameters.[1] To derive the relationship between the impedance, voltages, and currents shown in Figure A.2, we must consider the individual terminals that allow current flow in and out of the black box.

There are two ways that a current can enter and leave the black box at port 1. One case is where the current can enter the black box at port 1 and also leave at port 1. The corresponding Equation A.1 describes this relationship, where the first subscript number represents the final port that the current leaves from and the second subscript number represents the origin port that the current leaves from.

$$V_1 = Z_{11} I_1 \tag{A.1}$$

The second way for the current to leave the black box at port 1 is for the current to enter first at port 2. The corresponding Equation A.2 describes this relationship.

$$V_1 = Z_{12} I_2 \tag{A.2}$$

Since the current I_2 entering and leaving the black box must be equal, Equations A.1 and A.2 must sum to V_1, leading to the final Equation A.3:

$$V_1 = Z_{11} I_1 + Z_{12} I_2 \tag{A.3}$$

The same set of equations can be written for V_2, as shown in Equation A.4.

$$V_2 = Z_{21}I_1 + Z_{22}I_2 \tag{A.4}$$

These derived equations become useful because as long as a short circuit is introduced at a single port, I_1 or I_2 can become zero, enabling the calculation of the respective impedance parameters Z_{11}, Z_{12}, Z_{22}, Z_{21}. In our case, since the sample takes the place of the black box, the ports are theoretically symmetrical such that $Z_{11} = Z_{22}$ and $Z_{12} = Z_{21}$. The Z_{11} would give the amplitude information of the complex impedance while the Z_{21} would give the phase information. Although our study is limited to only Z_{11} type measurements, we believe that such information is still valuable for the initial ultrafast impedance measurements demonstrated in this work.

Recall that when employing measurements with a network analyzer and the time-resolved oscilloscope, scattering parameters now describe how traveling currents and voltages in a transmission line are affected when met at a discontinuity introduced by the model black box. When the incident signal arrives at one of the ports, some of the signal is reflected backward, while the remaining signal transmits or scatters to another port. We generalize the motion of these signals as waves that have directionality.

We now define the forward wave and a reverse wave in this network system using voltages, currents, and impedance. If we rewrite Equation A.3 and A.4 for scattering parameters, we see that b_1, b_2, a_1, and a_2 must be defined, where $a(x)$ represents the forward wave and $b(x)$ represents the backward wave as shown in Equation A.5 and A.6

$$b_1 = S_{11}a_1 + S_{12}a_2 \tag{A.5}$$

$$b_2 = S_{21}a_1 + S_{22}a_2 \tag{A.6}$$

We next redefine the voltage $V(x)$ as phasor quantities shown in Equation A.7 and the current $I(x)$ as a ratio of voltage and impedance shown in Equation A.8:

$$V(x) = V^+(x) + V^-(x) \tag{A.7}$$

$$I(x) = \frac{V^+(x)}{Z_0} - \frac{V^-(x)}{Z_0} \tag{A.8}$$

If the scattering parameters are measured as a power, and the equation for power is the product of current and voltage, we can rewrite the power equation using Equations A.7 and A.8:

$$\begin{aligned} P &= IV \\ P &= (V^+(x) + V^-(x))(\frac{V^+(x)}{Z_0} - \frac{V^-(x)}{Z_0}) \\ P &= \frac{V^+(x)^2}{Z_0} + \frac{V^+(x)V^-(x)}{Z_0} - \frac{V^-(x)V^+(x)}{Z_0} + \frac{V^-(x)^2}{Z_0} \\ P &= \frac{V^+(x)^2}{Z_0} - \frac{V^-(x)^2}{Z_0} \end{aligned} \tag{A.9}$$

We now define the first term in Equation A.9 as $a(x)^2$ and the second term in as $b(x)^2$, such that $a(x)$ and $b(x)$ are now defined as the wave amplitudes of the forward and reverse waves respectively:

$$a(x) = \frac{V^+(x)}{\sqrt{Z_0}} \tag{A.10}$$

$$a(x) = \frac{V^-(x)}{\sqrt{Z_0}} \tag{A.11}$$

Using Equations A.10 and A.11, we can now rewrite the total $V(x)$ and $I(x)$ in terms of $a(x)$ and $b(x)$:

$$\frac{V(x)}{\sqrt{Z_0}} = a(x) + b(x) \tag{A.12}$$

$$I(x)\sqrt{Z_0} = a(x) - b(x) \tag{A.13}$$

Equations A.12 and A.13 now show how the impedances, voltages, and currents relate back to the forward and reverse wave constants, which then relate back to the scattering parameters. Although the measurement of scattering parameters is typically preferred over impedance parameters at high frequencies, impedance values can still be extracted for analysis depending on the application, as shown in this work.

A.3 Three port networks (directional couplers)

Now we consider the case of a directional coupler that employs a four-port network system, but practically operates as a three-port system because the last port is terminated. We also consider a case such that each pair of ports are mutually isolated (ports 1 and 2 and ports 3 and 4 are mutually isolated pairs) and that the ports of one pair are both matched. If port 4 is terminated, ports 1 and 3 are now coupled, such that a fraction of the input power at port 1 is delivered to port 3. In the experiments described in Chapter 2.2-2.3, 10% of the power at port 1 is measured at port 3. A general schematic of the direction coupler is shown in Figure A.3.

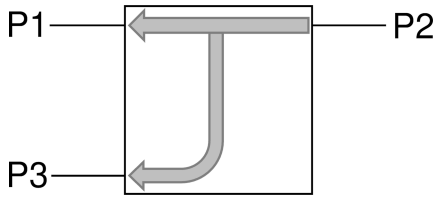

Figure A.3: General schematic of a directional coupler, where ports P1 and P3 are coupled while P2 is uncoupled and P4 is terminated.

The directional coupler is set up such that the sample is configured at the transmitted port (effectively port 1) and the custom VNA is configured at the coupled port (port 3) so that the signal relating to the S11 reflection parameter can be measured. By adopting this experimental geometry, Port 2, the uncoupled port, can now be used to transmit the carrier signal or perturbing frequency wave from the signal generator. With the integrated directional coupler, ultrafast impedance measurements can now be achieved in reflection geometry experiments. Future work in modifying the sample for transmission experiments can enable phase modulation measurements which are key for calculating the complete, complex impedance of the sample in study and ultimately the absolute ionic conductivity.

References

[1] Peter C. L. Yip. *High-Frequency Circuit Design and Measurements*. 1st. Chapman & Hall, 1990. 224 pp.

Appendix B

PRINCIPLES OF AMPLITUDE DEMODULATION

From Chapter 2.1, recall that a waveform initially generated by the signal generator transmits through the sample first before the final waveform is measured and analyzed. If we consider the original waveform as the initial state from which the change in amplitude and phase can be determined, the complex impedance can be derived.

Another way to interpret this process is that the sample acts as a data modulation source, changing the amplitude and phase of the original waveform transmitted from the signal generator. We refer to this original waveform as the carrier frequency or carrier signal, with a characteristic amplitude for the sinusoidal wave as shown in Equation B.1:[1]

$$c(t) = A_c cos(2\pi f_c t) \tag{B.1}$$

where f_c is the frequency and A_c is the amplitude of the carrier signal.

When the sample modulates this carrier frequency, the resulting waveform now has information encoded within the carrier signal. The sample, in this case, can be referred to as the transmission medium that enables such information to be encoded in the carrier signal. Generally, the described carrier amplitude modulation can be thought of as a form of signal modulation, where the amplitude of the carrier wave is modulated by another waveform, in this case, deriving from the transmission of the carrier wave through the sample.

If the characteristic sinusoidal wave deriving from the sample is generally defined as some function $m(t)$ with a modulation index of M and frequency $\omega_m = 2\pi f_m$, [2] the general form of a modulated signal comprised of both the carrier frequency and the encoded message signal from the sample can be written as Equation B.2:

$$y(t) = A_c[1 + k_a m(t)]c(t) \tag{B.2}$$

where k_a is a constant called the amplitude sensitivity of the modulator responsible for the generation of the modulated signal $s(t)$. An illustrative representation of the

amplitude demodulation process is shown in Figure B.1, where the low frequency signal corresponding to the sample (b) modulates the high frequency carrier signal(a) to yield the final amplitude modulated signal (c). The minimum and maximum levels related to the amplitude-modulated signal components are $1 - M$ and $1 + M$ respectively. The resulting modulation creates three distinct frequency components, specifically one related to the carrier f_c and the other two related to the modulation signal $\pm$ f_m, with the $+f_m$ being termed the upper sideband and the $-f_m$ being termed the lower side band. Both sidebands are centered symmetrically around f_c as long as $f_m < f_c$.

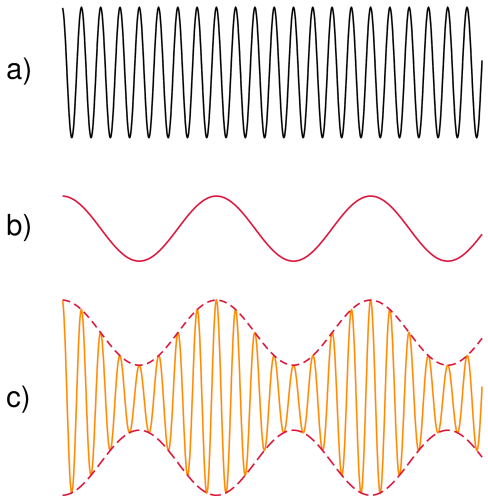

Figure B.1: Amplitude modulation of a carrier frequency with a modulation frequency. (a) High frequency carrier signal. (b) Low frequency sample modulation signal. (c) Final amplitude demodulation as a result of encoding the low frequency modulation signal (b) onto the high frequency carrier signal (a).

Conversely, amplitude demodulation involves the process of retrieving the encoded information from the original carrier frequency by the removal or reduction of the carrier frequency. The key advantage of utilizing amplitude demodulation methods is the ability to extract the original modulation with minimal distortions and noise, though they can still be subject to environmental interference and noise.

One approach for performing an amplitude demodulation includes the rectification of the modulated signal. Then, a low pass filter is used to filter out the high-frequency components, after which the recovered information can be retrieved.

A general schematic illustrating both these processes is shown in Figure B.2, where rectifying the modulated signal results in the positive data set of the starting modulated waveform, or $+f_m$. Then, a low-pass filter is used to remove the high frequency

component of the modulated waveform, leaving behind the final modulation waveform associated with the sample.

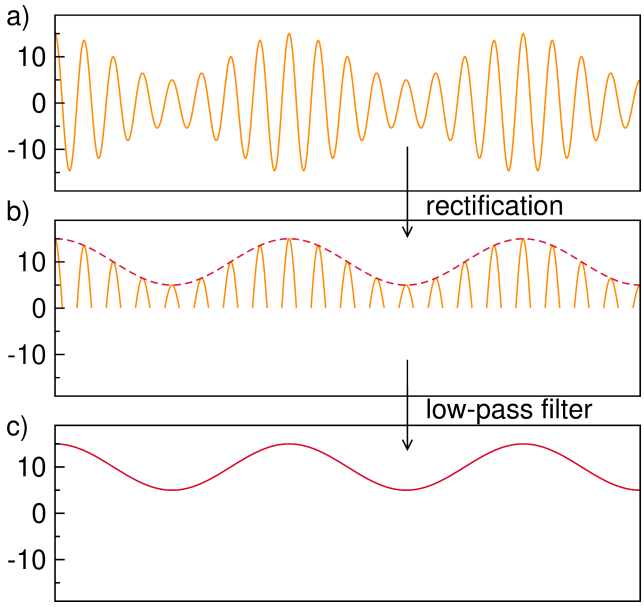

Figure B.2: Amplitude demodulation of a modulated signal to extract the modulation or messenger frequency.(a) Inital amplitude modulated signal. (b) Rectified signal of (a). (c) Extracted low frequency modulation signal using a low-pass filter.

In Chapter 2.3, we show that applying the amplitude demodulation function is essential for extracting encoded information related to the sample. One limitation with using the amplitude demodulation function, however, is that extracting the modulation signal is only possible when the modulation substantially exceeds the signal to noise ratio of the measurement. In the current state of our instrument, we are currently only able to achieve a large enough modulation signal under excitation conditions to perform the amplitude demodulation procedure and extract the modulation information. A resonator designed to amplify the modulation associated with the sample would be helpful for obtaining initial modulation values under dark conditions.

References

[1] Haykin. *Communication Systems, 4th Ed*. Google-Books-ID: p1Ty2RJ1Z8UC. Wiley India Pvt. Limited, Aug. 2006. 836 pp. ISBN: 978-81-265-0904-1.

[2] Michael G. Ruppert et al. "A review of demodulation techniques for amplitude-modulation atomic force microscopy". In: *Beilstein Journal of Nanotechnology* 8.1 (July 10, 2017). Publisher: Beilstein-Institut, pp. 1407–1426.

ISSN: 2190-4286. DOI: 10.3762/bjnano.8.142. URL: https://www.beilstein-journals.org/bjnano/articles/8/142 (visited on 11/02/2024).

Appendix C

NEB AND BAND-STRUCTURE CALCULATIONS

First-principles calculation were performed with the Vienna Ab initio Simulation Package (VASP) [1–3] with the PBE exchange-correlation functional. [4]

The Projector augmented wave (PAW) method potential was employed [5, 6] for La ($5s^2$, $5p^6$, $5d^1$, $6s^2$), Li ($1s^2$, $2s^1$), Ti_{GW} ($3s^2$, $3p^6$, $3d^4$) and O_{GW} ($2s^2$, $2p^4$) to describe the electron-ion interactions. The structural relaxations were performed with an energy cutoff of 550 eV for the plane-wave basis, employing a $4\times4\times4$ and $\Gamma-$centered k mesh. The lattice constant was set to 7.7378 Å [7] and the atoms were relaxed until the forces were less than 10 meV/Å. For the excited state calculations, we employed the CDFT approach [8] with `ISMEAR=-2` flag to promote one electron from the VBM to the CBM at the Γ point in both the spin channels.

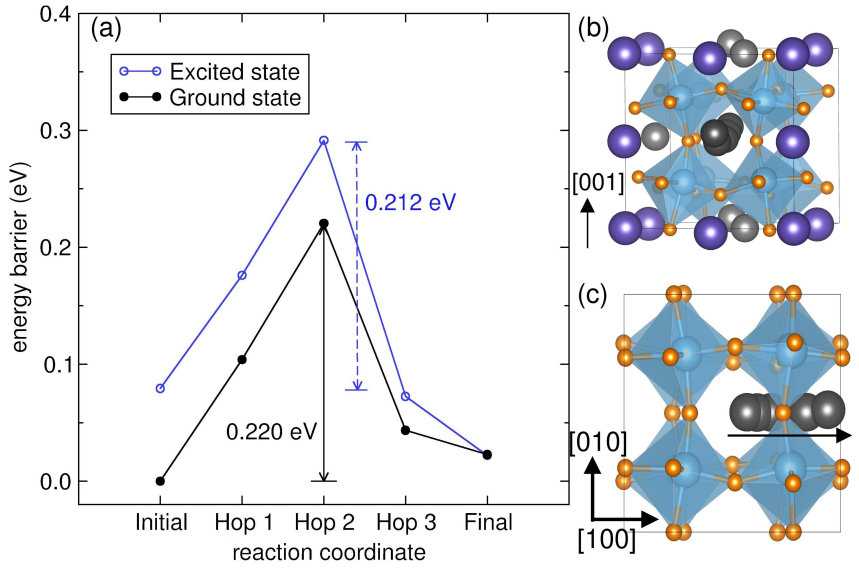

Figure C.1: Calculated energy barriers of the hopping Li^+ at the ground and excited state for the partially-ordered phase.(a) The ground and excited state migration pathways are shown as the solid black and blue lines respectively. The arrows represent the energy difference between the saddle point and the initial starting energy. (b) side and (c) top view of the complete NEB path, where the migrating Li atoms are marked in dark gray. In the top view, the La and non-migrating Li atoms are not shown for clarity, and the direction of migration is shown by a black arrow. *Figure courtesy of Dr. Vijaya Begum-Hudde.*

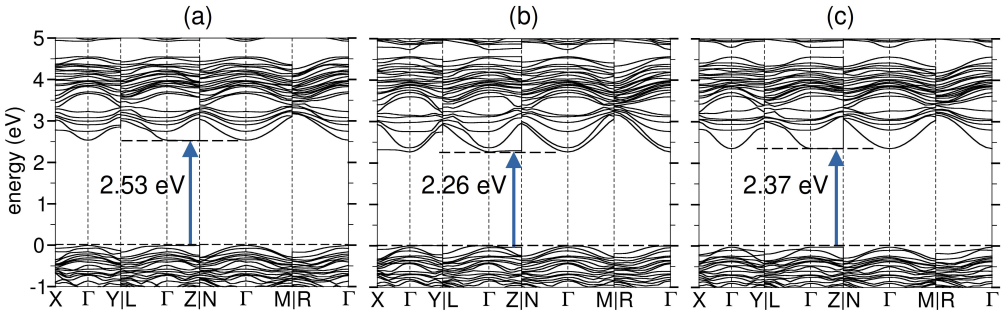

Figure C.2: Band structure of the ground state of the fully-ordered phase. (a) Starting structure of the NEB path (b) saddle point and (c) end structure of the NEB path with VBM set to zero. Band gap in (a) indirect, Γ (VBM) to Z(CBM), (b) indirect, between $L - \Gamma$ to Γ and (c) direct, Z to Z. *Figure courtesy of Dr. Vijaya Begum-Hudde.*

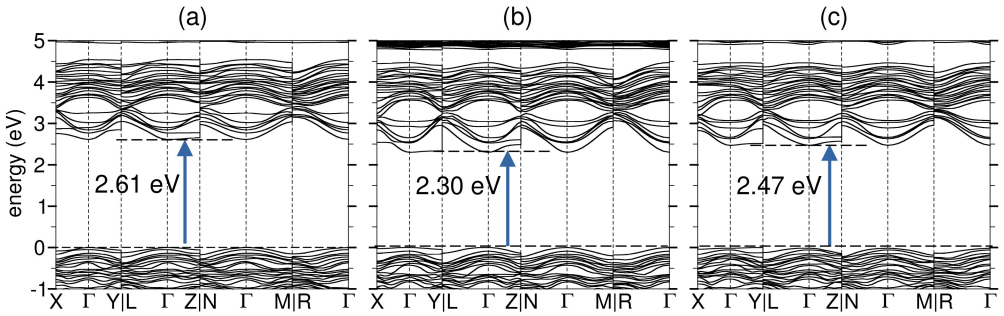

Figure C.3: Band structure of the ground state of the partially-ordered phase. (a) Starting structure of the NEB path (b) saddle point and (c) end structure of the NEB path with VBM set to zero. Band gap in (a) direct, Γ (VBM) to Γ(CBM), (b) indirect, between $L - \Gamma$ to Γ and (c) indirect, Y to Γ. *Figure courtesy of Dr. Vijaya Begum-Hudde.*

NEB climb methodology [9] within the implementation of VASP was employed to relax the images to compute the migration barrier. The end structures for the minimum energy pathway were taken from a previously published work[7]. The end structures were relaxed for both the ground- and excited-state NEB path, and three images were used to calculate the migration barriers.

A force-based optimizer- Fast Inertial Relaxation Engine (`IBRION = 3, POTIM = 0, IOPT = 7`), FIRE [9] was employed for the relaxations. The migration barrier were computed by employing Akima fit, and was calculated as the difference between the energy at the saddle point from the fitting and of the starting structure of the NEB path.

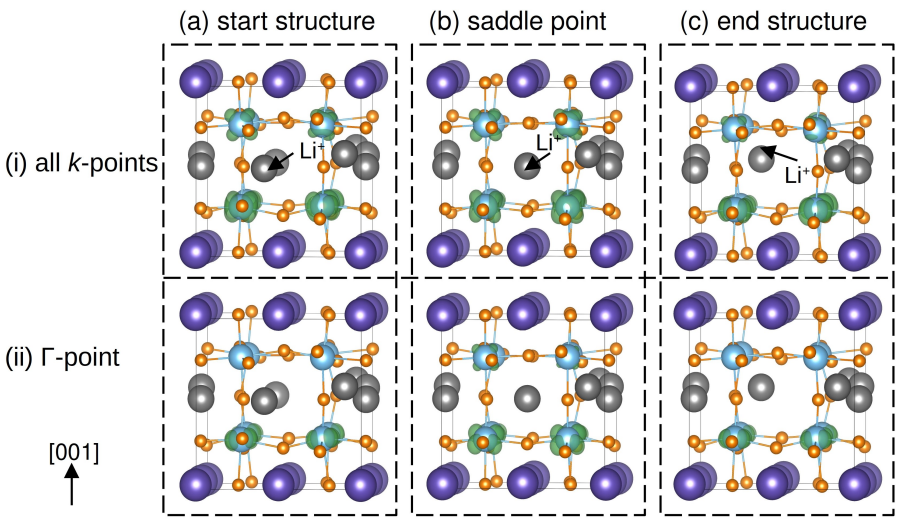

Figure C.4: Band-decomposed partial charge density plot for the fully-ordered phase of the conduction band minimum (CBM). (a) starting structure (b) saddle point and (c) end structure of the NEB path. (i) Top row depicts charge density for all the *k*-points and (ii) bottom row is for the Γ−point. Iso-surface (in green) of the plot represents a charge density of 0.002 1/Å^3. The migrating Li^+ ion is marked with a black arrow and the NEB path is along the *a*-*b* plane towards the center of the structure.*Figure courtesy of Dr. Vijaya Begum-Hudde.*

References

[1] G. Kresse and J. Hafner. In: *Phys. Rev. B* 47 (1 Jan. 1993), pp. 558–561. DOI: 10.1103/PhysRevB.47.558. URL: https://link.aps.org/doi/10.1103/PhysRevB.47.558.

[2] G. Kresse and J. Furthmüller. In: *Computational Materials Science* 6.1 (1996), pp. 15–50. ISSN: 0927-0256. DOI: https://doi.org/10.1016/0927-0256(96)00008-0. URL: https://www.sciencedirect.com/science/article/pii/0927025696000080.

[3] G. Kresse and J. Furthmüller. In: *Phys. Rev. B* 54 (16 Oct. 1996), pp. 11169–11186. DOI: 10.1103/PhysRevB.54.11169. URL: https://link.aps.org/doi/10.1103/PhysRevB.54.11169.

[4] John P. Perdew, Matthias Ernzerhof, and Kieron Burke. "Rationale for mixing exact exchange with density functional approximations". In: *The Journal of Chemical Physics* 105.22 (Dec. 1996), pp. 9982–9985. ISSN: 0021-9606. DOI: 10.1063/1.472933. eprint: https://pubs.aip.org/aip/jcp/article-pdf/105/22/9982/19228856/9982_1_online.pdf. URL: https://doi.org/10.1063/1.472933.

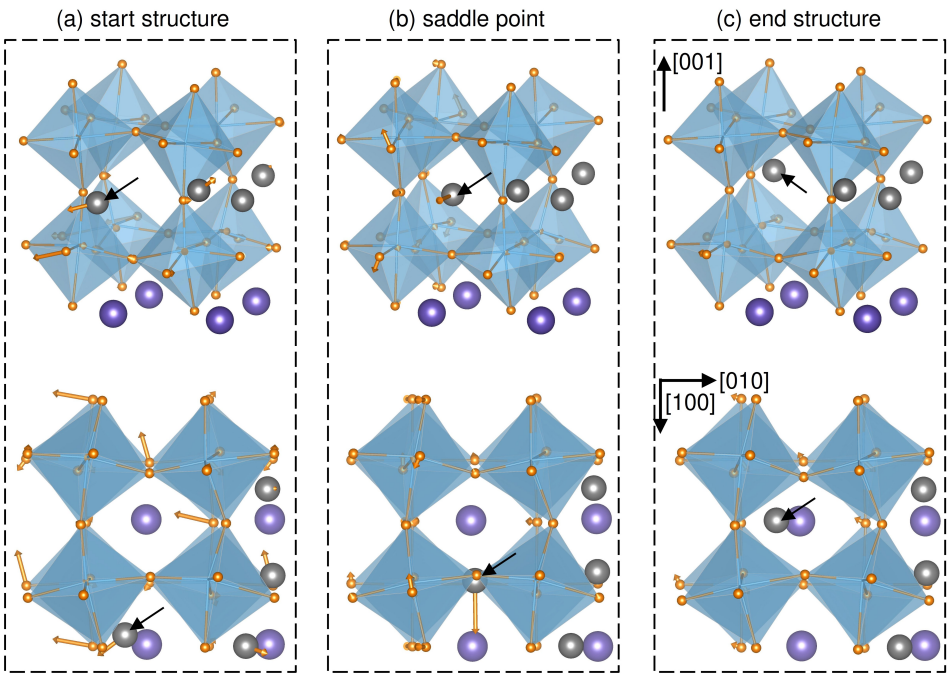

Figure C.5: Displacements in the fully-ordered phase calculated as the distance between the relaxed atomic positions of the excited and ground state structures. Orange arrows indicate the displacements for the relaxed ground state geometry (tail of the arrow) with respect to excited-state geometry (head of the arrow) in the NEB path for (a) start structure, (b) saddle point and (c) End structure. Black arrows mark the migrating Li^+ ions. *Figure courtesy of Dr. Vijaya Begum-Hudde.*

[5] P. E. Blöchl. In: *Phys. Rev. B* 50 (24 Dec. 1994), pp. 17953–17979. DOI: 10.1103/PhysRevB.50.17953. URL: https://link.aps.org/doi/10.1103/PhysRevB.50.17953.

[6] G. Kresse and D. Joubert. In: *Phys. Rev. B* 59 (3 Jan. 1999), pp. 1758–1775. DOI: 10.1103/PhysRevB.59.1758. URL: https://link.aps.org/doi/10.1103/PhysRevB.59.1758.

[7] Kim H. Pham et al. "Correlated Terahertz phonon-ion interactions dominate ion conduction in solid electrolyte $Li_{0.5}La_{0.5}TiO_3$". In: arXiv:2305.01632 (Mar. 6, 2024). DOI: 10.48550/arXiv.2305.01632. arXiv: 2305.01632[cond-mat,physics:physics]. URL: http://arxiv.org/abs/2305.01632 (visited on 03/09/2024).

[8] Adam Gali et al. "Theory of Spin-Conserving Excitation of the $N{-}V^-$ Center in Diamond". In: *Phys. Rev. Lett.* 103 (18 Oct. 2009), p. 186404. DOI: 10.1103/PhysRevLett.103.186404. URL: https://link.aps.org/doi/10.1103/PhysRevLett.103.186404.

[9] Graeme Henkelman, Blas P. Uberuaga, and Hannes Jónsson. "A climbing image nudged elastic band method for finding saddle points and minimum

energy paths". In: *The Journal of Chemical Physics* 113.22 (Dec. 2000), pp. 9901–9904. ISSN: 0021-9606. DOI: 10.1063/1.1329672. URL: https://doi.org/10.1063/1.1329672.

Appendix D

FINITE-DIFFERENCE TIME-DOMAIN (FDTD) HEAT CONDUCTION MODEL SIMULATIONS

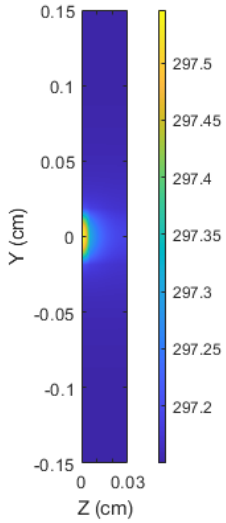

Figure D.1: Cross-section of the sample after 1 s of ultrafast laser heating, modeled with an 800 nm, 20 mW excitation with a penetration depth of 7 μm. *The colorbar corresponds to the temperature of the sample in Kelvin, with the initial temperature* 0 *and* $y = 0$. *Figure courtesy of Natan Spear.*

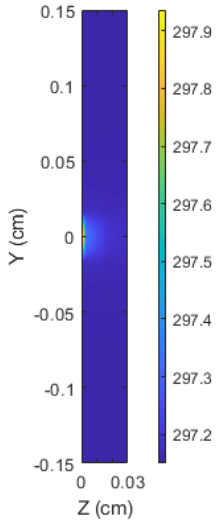

Figure D.2: Cross-section of the sample after 1 s of ultrafast laser heating, modeled with a 350 nm, 16 mW excitation with a penetration depth of 30 nm. The color bar corresponds to the temperature of the sample in Kelvin, with the initial temperature at 297 K. The sample and excitation is centered at x = 0 and y = 0. *Figure courtesy of Natan Spear.*

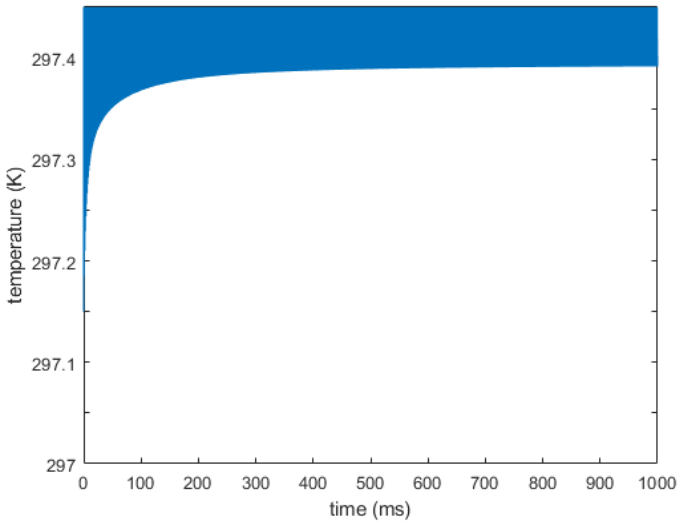

Figure D.3: The baseline maximum temperature in the sample for 800 nm, 20 mW light. The simulation demonstrates that the sample's baseline temperature reaches steady state within one second. Each pulse still causes a nearly instantaneous rise and decay, but a steady baseline temperature of 297.55 K is reached in several tenths of a second. *Figure courtesy of Natan Spear.*

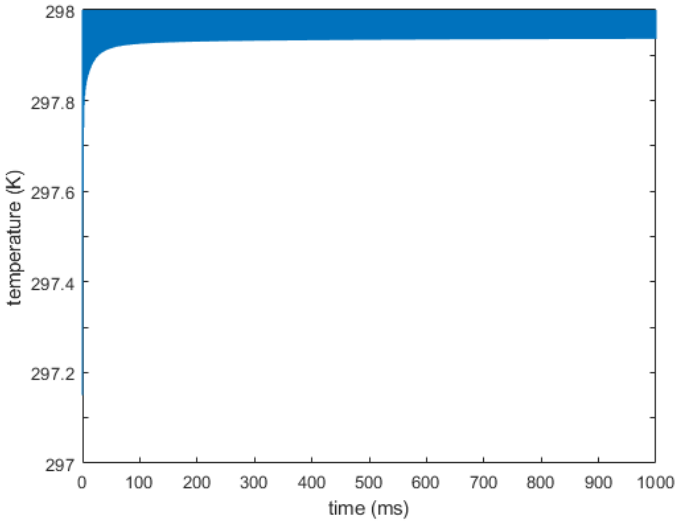

Figure D.4: The baseline maximum temperature in the sample for 350 nm, 16 mW light. The simulation demonstrates that the sample's baseline temperature reaches steady state within one second. Each pulse still causes a nearly instantaneous rise and decay, but a steady baseline temperature of 297.94 K is reached in several tenths of a second. *Figure courtesy of Natan Spear.*

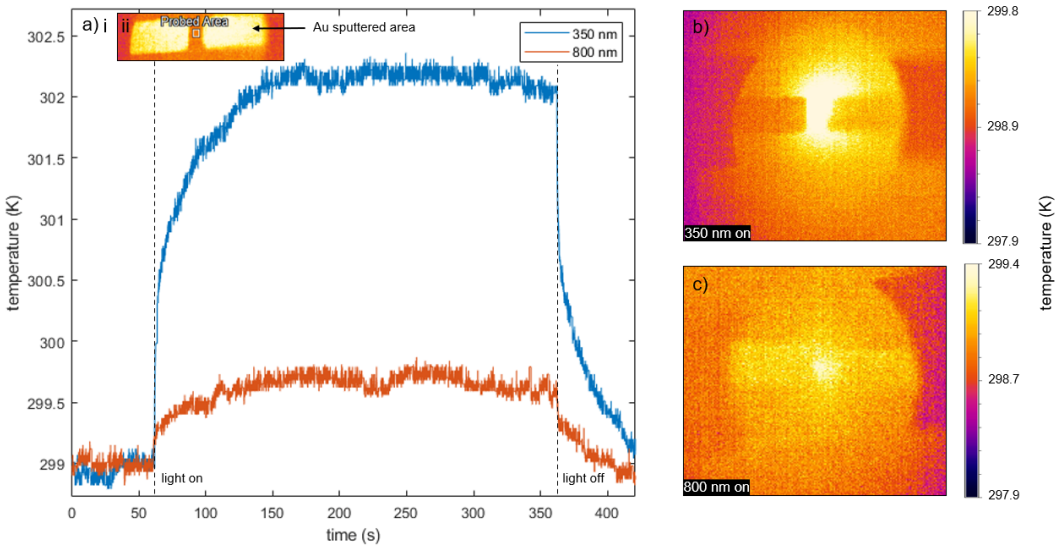

Figure D.5: Experimental measurement of the LLTO sample surface temperature with sputtered Au contacts under 800 nm, 20 mW and 350 nm, 16 mW illumination using an infrared thermal gun. (a) Measured surface temperature of the probed sample area upon illumination between 60 and 360 seconds (i) and inset of the IR camera image, showing the probed area of the sample (ii). (b) Surface map of sample under 350 nm excitation and 800 nm excitation (c) focused between the Au electrodes. *Figure courtesy of Amy Lin.*

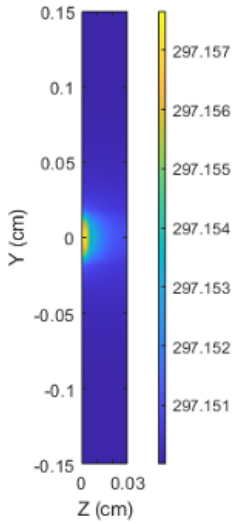

Figure D.6: Cross-section of the sample after 1 s of ultrafast laser heating, modeled with a 1 mW THz light excitation with a penetration depth of 6 μm. The color bar corresponds to the temperature of the sample in Kelvin, with the initial temperature at 297.15 K. The sample and excitation are centered at x = 0 and y = 0. *Figure courtesy of Natan Spear.*

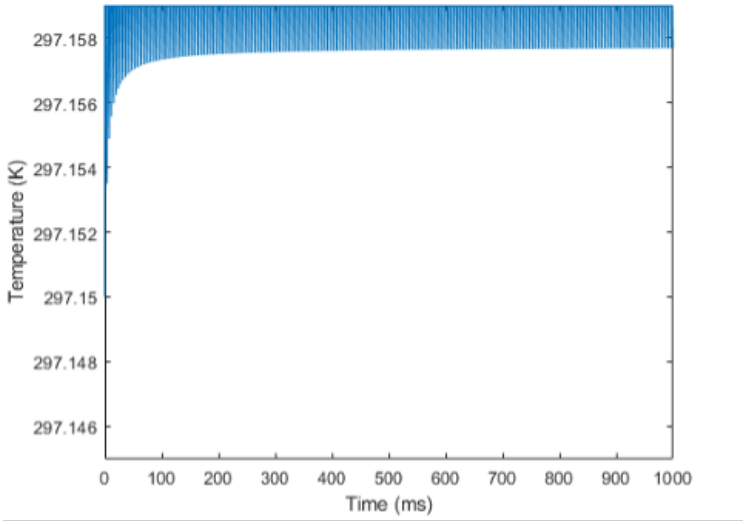

Figure D.7: The baseline maximum temperature in the sample for THz light. The simulation demonstrates that the sample's baseline temperature reaches steady state within one second. Each pulse still causes a nearly instantaneous rise and decay, but a steady baseline temperature of 297.158 K is reached in several tenths of a second. *Figure courtesy of Natan Spear.*

Appendix E

CUSTOM ELECTROCHEMICAL CELL DESIGNS

E.1 Optical cell

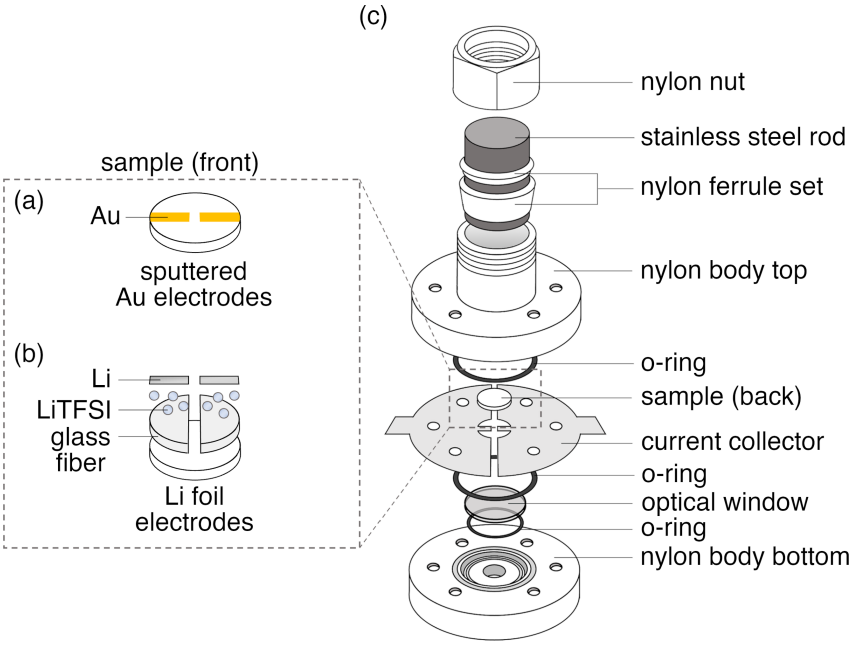

Figure E.1: Blocking and non-blocking electrode sample set up and corresponding custom electrochemical optical cell design.(a) Blocking electrode geometry utilizing Au sputtered electrodes on the plane of the sample. (b) Non-blocking electrode set up utilizing Li foil and a glass fiber separator soaked in 1 M LiTFSI. (c) Optical cell design to enable electrochemical measurements under simultaneous photo-excitation. Six screws are used to assemble the cell through the six corresponding, depicted holes shown in both nylon body parts.

The custom optical cell was designed to enable air-free electrochemical experiments under simultaneous optical excitation. The excitation enters through the hole in the center of the nylon body bottom and the desired optical window, then to the un-sputtered area of the sample. The optical window is chosen to maximize transmission. In the experiments described in Chapter 3.6, an uncoated, fused silica window was used that transmits 93.0% and 93.5% of the 350 nm and 800 nm light respectively.

The stainless steel current collector was machined to match the in-plane electrode

geometry of the cell. The stainless steel rod is used to apply pressure to the sample and ensure contact between the electrodes and the current collector. The nylon nut and ferrule set is used to secure the top barrel section of the nylon body top, fully enclosing the cell against air exposure. Six screws are used to enclose the cell by screwing into the threaded holes of both nylon body parts.

E.2 Heating cell

The heating cell was designed to conduct electrochemical experiments with an in-plane sample geometry like that shown for the optical cell, but with an additional temperature controller. To insulate the cell, chemical-resistant Nlyon foam sheets were used. A 20.0 mm x 20.0 mm Thorlabs HT24-24 W Metal Ceramic Heater was used in conjunction with the externally powered TC-48-20 OEM to control the internal temperature of the cell via the thermistor. An optically transparent window can be used to enable simultaneous photo-excitation, or for non-air sensitive samples. A Teflon window with a centered drilled through hole can be used to fill the gap between the sample and nylon cell top. The nylon cell top contains two o-ring wells to seal the stainless steel plate, or current collector, and the optically transparent window. Five screws and wingnuts are used to secure the cell through the five depicted non-threaded holes in Figure E.2.

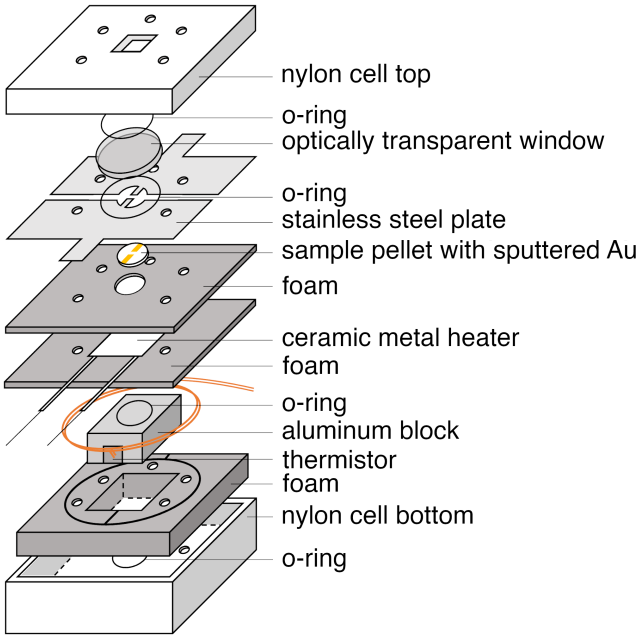

Figure E.2: Electrochemical heating cell set-up to obtain the power-to-temperature calibration curve and collect EIS data below 32 MHz with the 1260A Solartron. The cell components are compressed and held together with screws that fit through the five holes depicted. Each screw is secured with wingnuts.

Appendix F

BLOCKING AND NON-BLOCKING DC POLARIZATION EXPERIMENTS WITH LLTO (EXTENDED)

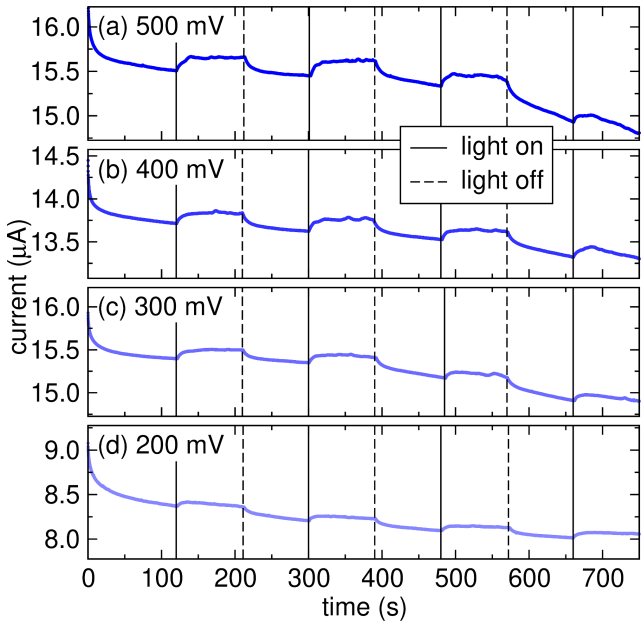

Figure F.1: DC Polarization experiments for LLTO upon 350 nm irradiation using non-blocking Li electrodes. A potential hold of (a) 500 mV, (b) 400 mV, (c) 300 mV, (d) 200 mV, and (e) 100 mV were applied to measure the steady state current with and without irradiation in 90 second intervals.

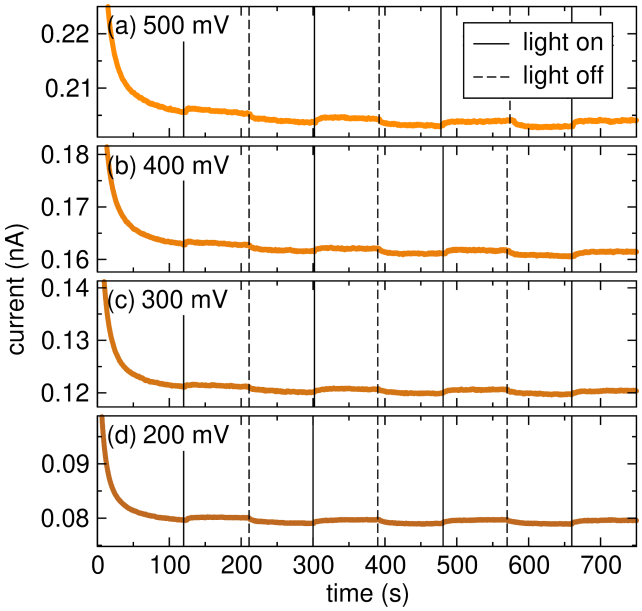

Figure F.2: DC Polarization experiments for LLTO upon 350 nm irradiation using blocking Au electrodes. A potential hold of (a) 500 mV, (b) 400 mV, (c) 300 mV, and (d) 200 mV were applied to measure the steady state current with and without irradiation in 90 second intervals.

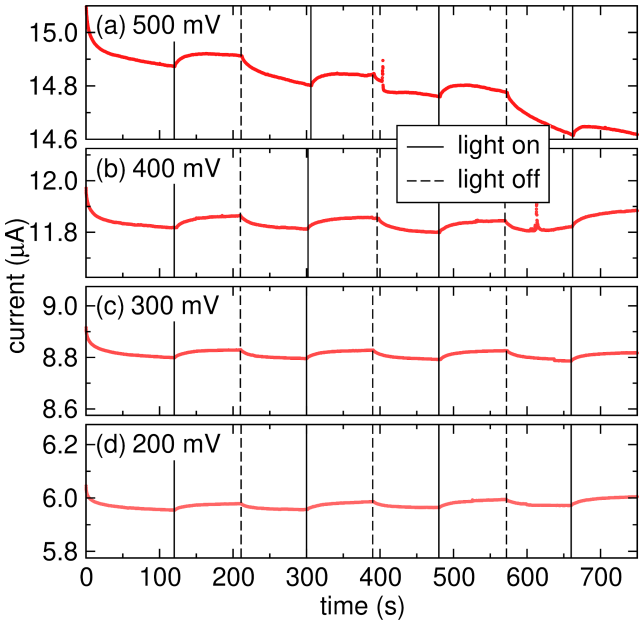

Figure F.3: DC Polarization experiments for LLTO upon 800 nm irradiation using non-blocking Li electrodes. A potential hold of (a) 500 mV, (b) 400 mV, (c) 300 mV, (d) 200 mV, and (e) 100 mV were applied to measure the steady state current with and without irradiation in 90 second intervals.

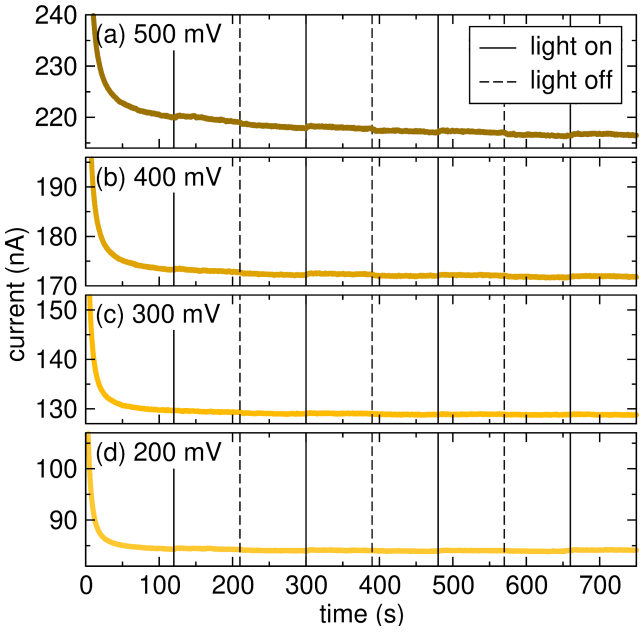

Figure F.4: DC Polarization experiments for LLTO upon 800 nm irradiation using blocking Au electrodes. A potential hold of (a) 500 mV, (b) 400 mV, (c) 300 mV, and (d) 200 mV were applied to measure the steady state current with and without irradiation in 90 second intervals.

Appendix G

REPLICATES OF CHANGES IN IMPEDANCE CAUSED BY ABOVE-BAND GAP EXCITATION OF LLTO (EXTENDED)

In addition to the above-band gap EIS measurements at 350 nm shown in Figure 3.4, a similar series of replicates were done with a 349 nm, 1 kHz, nanosecond pulse width excitation source. With the longer pulse excitation, a more significant shift can be measured in the Nyquist plot, confirming the linear change in impedance versus laser power with more minimized error. Due to limitations in fourth harmonic generation, the shifts in impedance are limited by the maximum power output that can be generated at each wavelength. In the 350 nm case, the maximum output is generally 8-13 mW, causing a smaller measurable shift in impedance, while in the 349 nm case, an output up to 40 mW can be achieved and shows the impedance shift more clearly. Since the 349 nm source has a longer pulse width, more of the enhanced signal is likely from optical heating, rather than the proposed photo-induced mechanism discussed in Chapter 3.

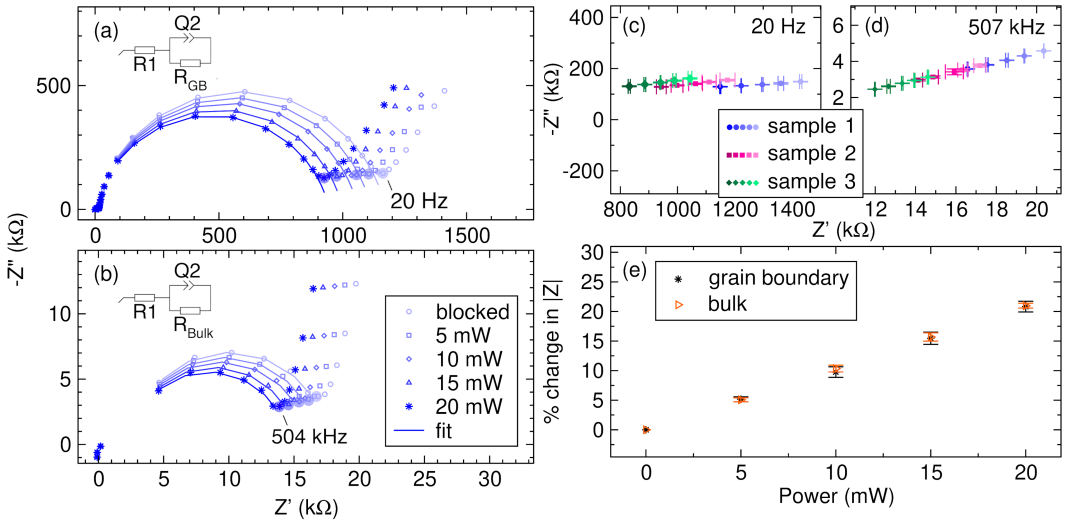

Figure G.1: Change in impedance upon band-gap excitation with 349 nm 1 kHz repetition rate nanosecond pulsed light between 5 – 20 mW. (a) Grain boundary semi-circle fit to a $R1 + R_{GB}/Q2$ circuit. (b) Bulk impedance semi-circle fit to a $R1 + R_{Bulk}/Q2$ circuit. (c) Grain boundary and (d) bulk replicates across three samples showing the change in impedance upon 349 nm light excitation over 5 – 20 mW at a frequency corresponding to the respective intercept of the semi-circle feature. (e) Percent change in impedance as a function of laser power shows a linear response for both the grain boundary and bulk.

Appendix H

800 NM SFIT OF LLTO (EXTENDED)

To compare the shift in impedance at similar average powers to the 350 nm experiment, an 11 mW, 800 nm excitation was also used for the SFIT measurements. Although a change in shift is noticeable, the shift is too small to analyze the transient aspects of the data.

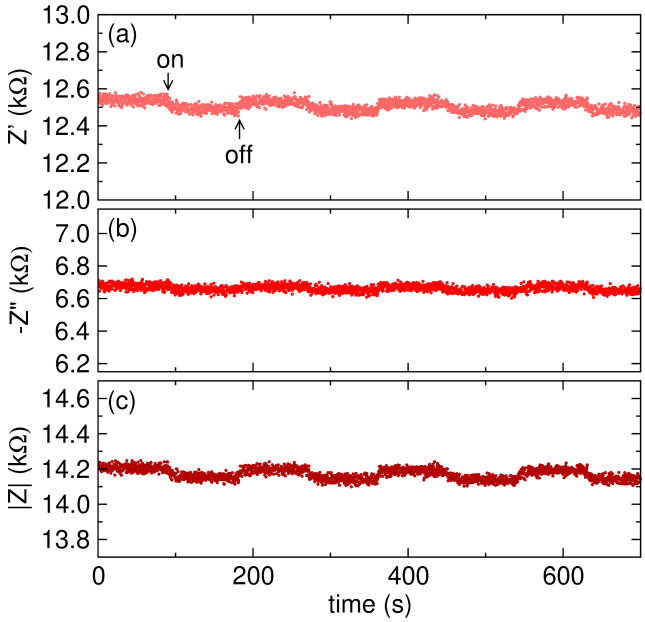

Figure H.1: SFIT measurements of (a) the real impedance, (b) the imaginary impedance, and (c) the total impedance of LLTO upon 800 nm, 11 mW excitation at 251 kHz and 100 mV sinusoidal frequency amplitude. The on and off label indicates when the impulse excitation is active or not.

Appendix I

REPLICATES OF CHANGES IN IMPEDANCE CAUSED BY THZ EXCITATION OF LLTO (EXTENDED)

Although the shifts in impedance are very small for the THz excitation EIS measurements due to the low average power, the shift is reproducible across three samples and four trials, as shown in Figure I.1.

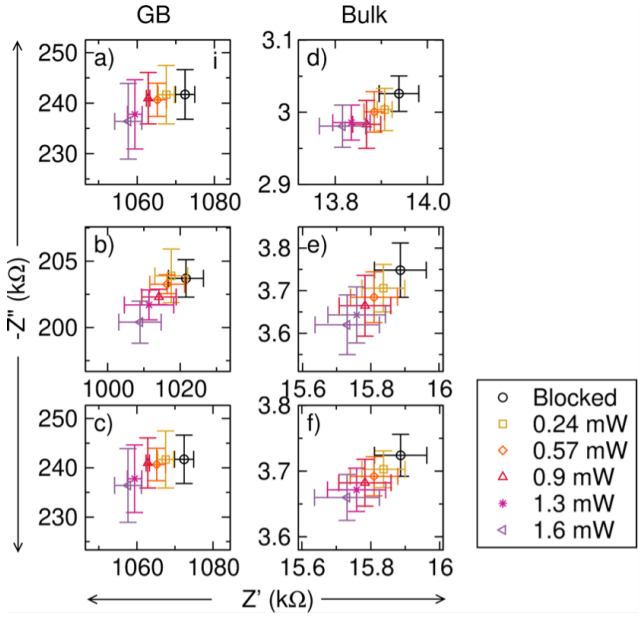

Figure I.1: Replicates of the measured -Z" and Z' at 32 Hz and 803 kHz upon THz excitation.(a-c) Single frequency impedance measurements at 32 Hz for grain boundary features and (d-f) at 803 kHz for the bulk features averaged over 3 samples and 4 trials. The frequency chosen represents the frequency at which the greatest difference is observed between the Nyquist plots at points close to the Z' intercept. The frequency is different from the intercepts shown Figure 4.7 because of the change in cell set up (and subsequent change in cell pressure). Although the absolute impedance varies slightly, the relative changes are consistent between sample to sample.

Appendix J

HOPPING PATHWAYS FOR JUMP RATE CALCULATIONS

The following hopping visualizations correspond to the numbered hops investigated in Table 4.1:

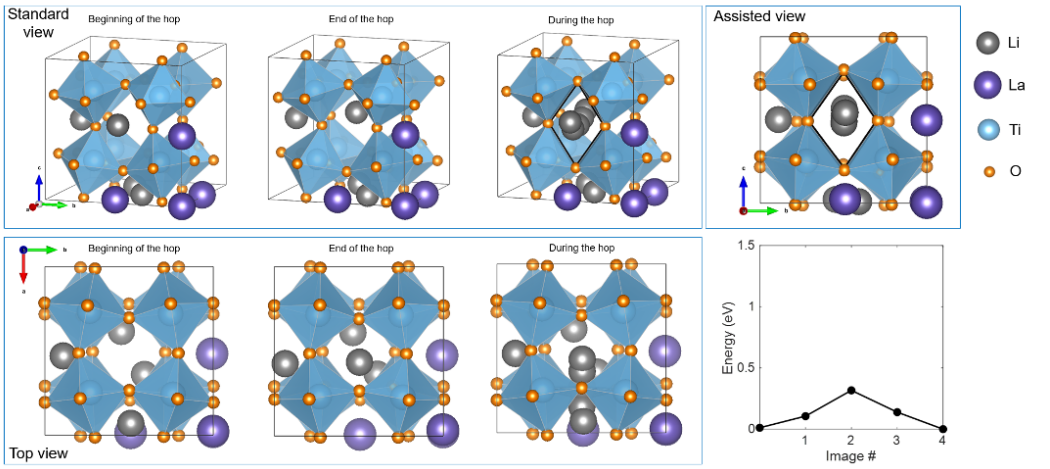

Figure J.1: Representation of Hop #1. The shown hop is a single ion hop, and the structure is derived by repositioning of the Li atoms in the parent disordered structure. *Figure courtesy of Dr. Kiarash Gordiz.*

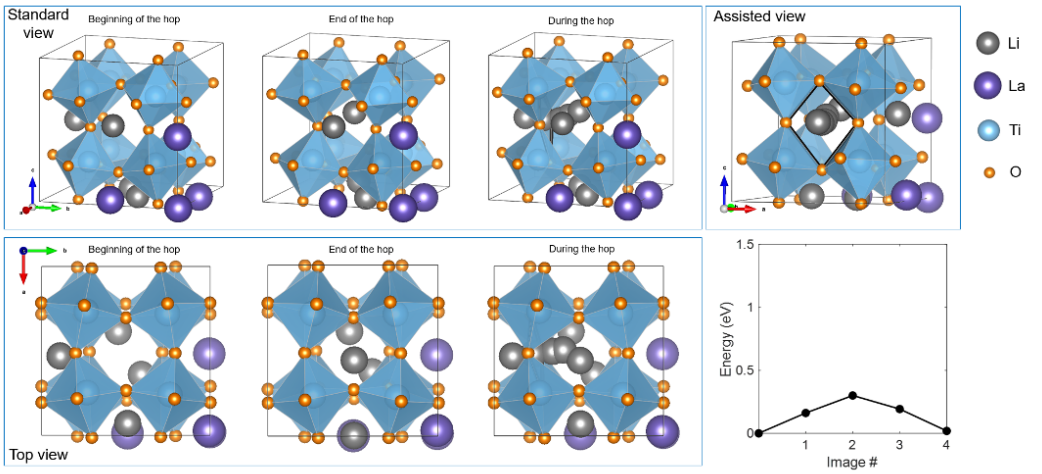

Figure J.2: Representation of Hop #2. The shown hop is a single ion hop, and the structure is derived by repositioning of the Li atoms in the parent disordered structure. *Figure courtesy of Dr. Kiarash Gordiz.*

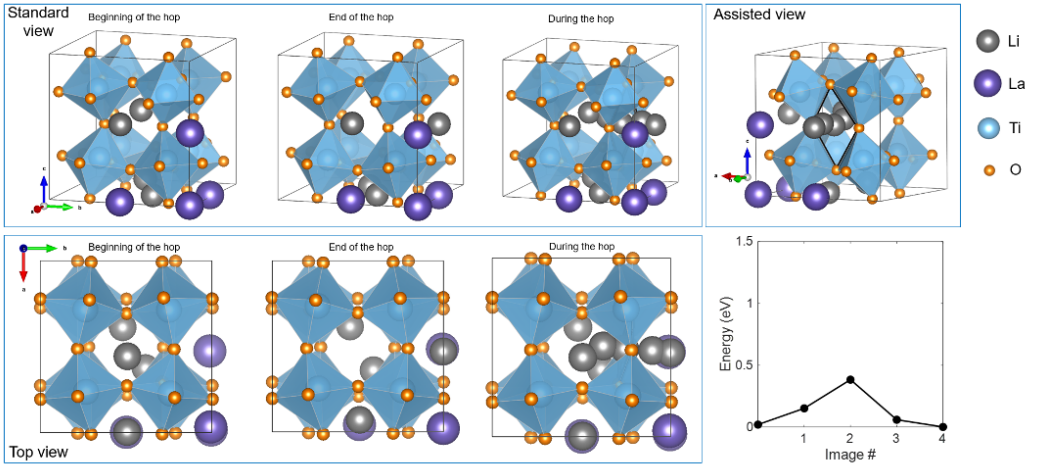

Figure J.3: Representation of Hop #3. The shown hop is a single ion hop, and the structure is derived by repositioning of the Li atoms in the parent disordered structure. *Figure courtesy of Dr. Kiarash Gordiz.*

Appendix K

THZ AVERAGE POWER CALCULATION

Terahertz pulse energies were measured using a calibrated pyroelectric THz joulemeter (Genctec EO SDX 1211). The subsequent THz field strength values were used to calculate an average power for comparison to the non-resonant heating.

$$pulse\ energy\ (J) = \frac{voltage\ output\ (V)}{614000\ (V/J)} \tag{K.1}$$

$$average\ power\ (W) = pulse\ energy\ (J) * repitition\ rate\ (Hz) \tag{K.2}$$

Using a pyroelectric THz joulemeter, a measured voltage was used to calculate the pulse energy of the THz field using Equation K.1, where 614000 V/J is the conversion factor according to the manufacturer specifications. The average power of the laser was then calculated using Equation K.2 where J is the pulse energy and (symbol) is the repetition rate of the pulses after passing the chopper (500 Hz).

IR Pump Power (mW)	Field Strength (keV/cm)	Peak to Peak Voltage (V)	Average THz Power(mW)
1000	162.50	2.0	1.60
800	141.22	1.6	1.30
700	128.68	1.3	1.10
600	114.86	1.1	0.90
500	96.61	0.9	0.73
400	83.42	0.7	0.57
200	46.88	0.3	0.24

Table K.1: IR power to THz field strength calibration yielding the average power calculation.

INDEX